GAMMA-RAY STUDIES

OF

SOME LIGHT NUCLEI.

A Thesis submitted for the degree of Master of Science at the Australian National University. 1965.

PREFACE.

This thesis described a series of experiments which were carried out on the Canberra Tandem Van de Graaff and Cockcroft-Walton accelerators in the Department of Experimental Nuclear Physics of the Australian National University. Covered is a two year period from March 1963 to March 1965.

The work described in Chapter III was carried out in conjunction with Mr. J.R. Patterson under the supervision of Professor E.W. Titterton. Approximately 50 percent of the supervised effort was my own. The remaining work, Chapters IV, V, was carried out under the supervision of Dr. T.R. Ophel.

Practically all the equipment used in the experiments had been previously developed in the Department and no significant changes were made. Only the leaky integrator technique was developed during the course of the He^3 experiments.

Some of the experiments described in this thesis have been published under the following titles:

1. Total Cross Section of the Reaction $B^{10}(He^3,t)C^{10}$ between threshold and 10.5 MeV.

   D.R. OSGOOD, J.R. PATTERSON and E.W. TITTERTON. Physics Letters. Vol. 10. No.1. (1964).

2. Total Cross Section of the Reaction $C^{10}(He^3,n)O^{14}$ between threshold and 11.4 MeV.

D.R. OSGOOD, J.R. Patterson, E.W. TITTERTON. Nuclear Physics. (In Press) (1965).

3. The 991 KeV Resonance of the $Al^{27}(p,)$ readtion.

T.R. OPHEL and D.R. OSGOOD. (In press).

Many people have assisted in the work described in this thesis, it is a pleasure to thank them.

To Professor E.W. Titterton for his patient supervision and constant encouragement during the course of the experiments.

To Dr. T.R. Ophel for his inspiring supervision of the $Mg^{26}(p,\gamma)$ investigations, and also for many helpful suggestions regarding general experimental procedures.

To Dr. F.C. Barker who gave much helpful advice during the preparation of some of the above papers.

To the Australian National University whose scholarship I held throughout the course of this work.

To Mrs. K. Prowse who typed this thesis capably and cheerfully.

No part of this thesis has been submitted for a degree at any other University.

* * * * *

D. R. Osgood.

CONTENTS

* * * * * * * *

INTRODUCTION.

One of the major fields of nuclear physics research is the accumulation of experimental data on the position and properties of the well defined resonances in the cross sections of low energy nuclear reactions. The primary purpose of the investigations reported in this thesis was to determine the position and properties of some levels that are accessible with a high resolution Tandem Van der Graaff accelerator (approx. 12 MeV) and a Cockcroft-Walton accelerator (approx. 1.2 MeV). Four separate experiments have been carried out and data has been collected on part of the level structure of the nuclei N^{13}, O^{15}, Al^{27} and Si^{28}. All the data has been collected via gamma-ray observations.

Chapter I describes briefly the general theoretical background to the experiments. The use of a leaky integrator in conjunction with a previously constructed activation apparatus is described.

The second Chapter discusses gamma-ray detection methods in some detail. For the majority of the discussion only NaI(Tl) detectors are considered. A solid state detector is mentioned in this section only briefly. Both single detector systems and combinations of detector systems are described. The combinations include a three crystal spectrometer, two detectors in coincidence and the sum coincidence technique. A separate section is devoted to gamma-ray detection as <u>all</u> the experimental work of the thesis involved the observation of gamma-rays.

An account of the $B^{10}(He^3,t)C^{10}$ and the $C^{12}(He^3,n)O^{14}$ reactions is given in Chapter three. These two reactions were investigated with the activation technique and all the usual quantities needed to determine the total cross sections were measured.

Considerable structure was found in the $C^{12}(He^3,n)O^{14}$ excitation function. From a comparison with the structure observed in other reactions leading to the compound nucleus, O^{15}, an interpretation of the structure has been made in terms of compound nuclear states, influenced at high energies by a direct interaction contribution. Several new levels in O^{15} were found from a study of the $C^{12}(He^3,n)O^{14}$ reaction. The $B^{10}(He^3,t)C^{10}$ reaction proved to be uninteresting with respect to nuclear levels as no obvious resonances were observed. The reaction apparently proceeded via a direct interaction process.

The fourth chapter relates the investigations into the low-lying levels of Al^{27}. This work was part of a systematic study of Al^{27} carried out at the A.N.U. The 2.98 MeV and 3.68 MeV levels have been investigated by means of double and triple gamma-ray correlation measurements at various resonances of the $Mg^{26}(p,\gamma)$ reaction. Efforts to excite the 3.68 MeV level with useful intensity via inelastic proton and alpha scattering were not successful.

The 3.68 MeV level has been assigned a spin and parity of $3/2^+$ and the $\left(\frac{\text{quadrupole}}{\text{dipole}}\right)$ amplitude mixing ratio of the only significant transition de-exciting the level via the 0.840 MeV level with at least 97% probability is -0.40 ± 0.05. The spin of the 2.98 MeV level has

been measured as 3/2 in accord with previous measurements.

The final chapter (five) is a report on the $Al^{27}(p,\gamma)Si^{28}$ reaction at the 991 KeV resonance. This was a re-investigation of work previously carried out at the A.N.U. as doubts had been cast on this earlier investigation. The analysis was the work of the Supervisor, Dr. T.R. Ophel. Although minor variations were observed the doubts of (An 64) were proved to be unfounded. Included in this chapter is a brief description of a solid-state gamma-ray detector that arrived shortly before the termination of the scholarship and only preliminary results on the resolution and applicability to a three crystal spectrometer are shown.

Appendix I describes the results of some calculations on target effective energy thicknesses and foil energy thicknesses.

Finally, Appendix II describes the present situation with regard to the scintillation process in crystals such as NaI(Tl).

* * * * * * * * * * *

CHAPTER I

1.1 The Compound Nucleus

In 1936 Niels Bohr (Bo 36) introduced the concept of the compound nucleus which has shaped the thinking of nuclear physicists ever since. The concept was based on the picture of the nucleus as a system with very strong short range forces. He suggested that some nuclear reactions could be considered to proceed via an intermediate state, known as the compound nucleus, which resulted from the absorption of the incident nucleon by the target nucleus. The incoming nucleon shared its energy with the other nucleons very rapidly, losing its individual identity in the process so that the properties of a compound nucleus with a given excitation energy could be essentially independent of the mode of formation. The break-up of this compound nucleus could take place via many channels subject to the conservation laws. The important fact enunciated was that the competition between the various modes did not depend on how the compound nucleus was formed.

To form a compound nucleus the incident particle must penetrate the coulomb barrier. The probability of penetration depends markedly on the bombarding energy. The compound nucleus like most nuclei is assumed to have discrete energy levels and if the excitation in the compound nucleus equals the energy of one of these discrete levels then a large penetration probability can be expected. This has been

FIG.1. A schematic representation of the Bohr compound nucleus concept. An endothermic reaction is depicted.

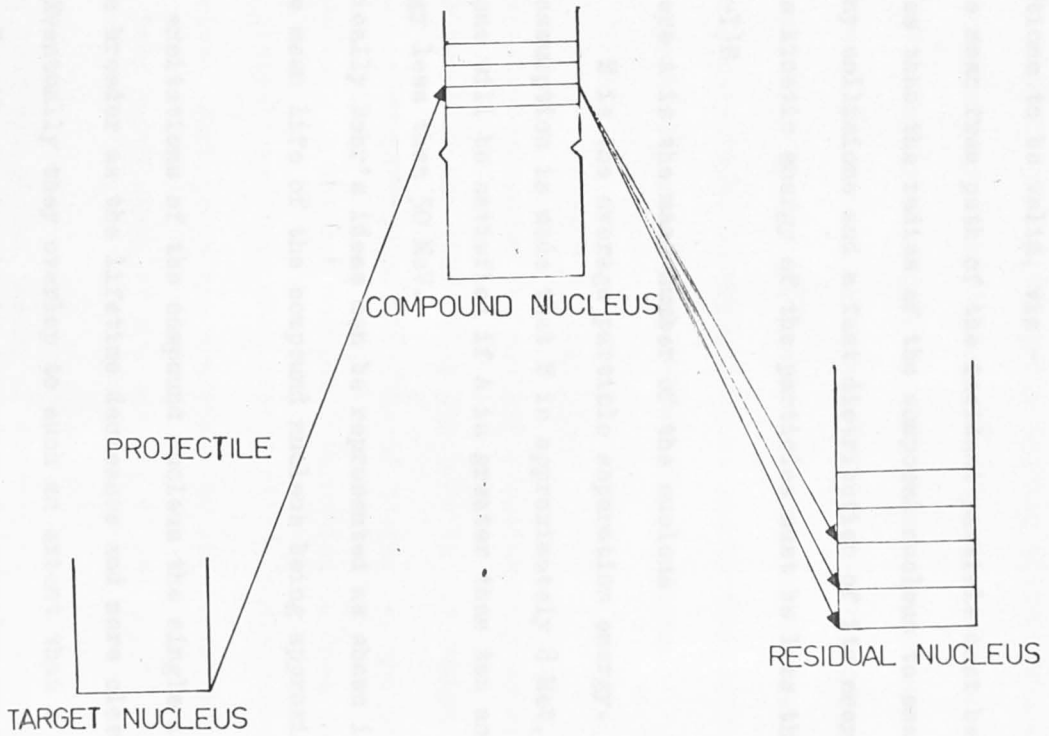
COMPOUND NUCLEUS
PROJECTILE
RESIDUAL NUCLEUS
TARGET NUCLEUS

FIG. 1.

called resonance formation of the compound nucleus and gives rise to sharp maxima in the excitation formation (Gu 29). Many such examples have been observed since the ideas were put forward.

Two conditions are necessary for the Bohr description of nuclear reactions to be valid, viz -

(i) the mean free path of the incident particle must be much less than the radius of the compound nucleus to ensure many collisions and a fast distribution of its energy.

(ii) the kinetic energy of the particles must be less than $(A-1)S$

where A is the mass number of the nucleus

S is the average particle separation energy.

If the assumption is made that S is approximately 8 MeV, then both conditions will be satisfied if A is greater than ten and the kinetic energy less than 50 MeV.

Schematically Bohr's ideas can be represented as shown in figure 1, the mean life of the compound nucleus being approximately 10^{-19} secs.

At high excitations of the compound nucleus the single isolated levels become broader as the lifetime decreases and more closely spaced in energy. Eventually they overlap to such an extent that a continuum is attained. In this region it is necessary to consider averages over many resonances. Experimentally, the onset of the continuum would be observed by the gradual disappearance of definite resonances

in the excitation function. However, the disappearance of the resonances need not necessarily hail the continuum as it could mean that other reaction mechanisms have taken over.

When the discrete energy levels of the compound nucleus are well separated, or have the same parity, the angular distributions of the break-up products are symmetric about 90°. However interference between two levels of opposite parity will cause marked asymmetry and the angular distributions will change markedly with the energy of the bombarding particle. In the continuum region the statistical cancellation of interference terms in general give smooth excitation functions and symmetry about 90°; except for Ericson fluctuations.

1.2 Direct Interactions

An alternative mechanism for nuclear reactions may be considered when the time spent by the bombarding particle in the region of the target nucleus is comparable to the time of transit of the particle across the nucleus. A nuclear surface interaction is then possible in which the incident particle only reacts with a small number of the target particles. Such processes are known as direct interactions. Probably the best known examples are the (d, p) and (d, n) stripping reactions.

The main features of the theory of direct interactions are

(i) The prediction that the differential cross section is strongly peaked in the forward direction.

(ii) The excitation function varies smoothly with energy exhibiting no resonances.

Relevant to (He^3, n) reactions (see section 3.2) is the extension of the direct stripping theory for the stripping of two nucleons formulated by Newns (Ne 60) and applied to the $C^{12}(He^3,n)O^{14}$ reaction.

In general, the compound nucleus and direct interaction modes of a reaction will both occur with one or the other predominating. Interference between the two modes can give conflicting results as appears to be evident in the $C^{12}(He^3,n)O^{12}$ reaction studies (section 3.2).

1.3 The Activation Technique

Both the $B^{10}(He^3,t)C^{10}$ and the $C^{12}(He^3,n)O^{14}$ reactions were investigated by the activation technique.

The Technique

Nuclear reactions are observed by the exposure of a target to a source of particles or photons of sufficient energy to react with the constituent nuclei of the target. Information can be obtained by observation of the prompt emissions that occur during the exposure. However, when the residual nucleus of a nuclear reaction is radioactive a relatively simple method of obtaining information is available. This is the activation technique, which consists of measuring the radioactivity produced after the exposure of the target has ceased. Since nearly all unstable nuclei emit γ-rays it should, in principle,

be possible to investigate total reaction cross sections by detection of the yield of these γ-rays. The reasons for this are

(i) A radio-active nucleus has a characteristic half life which can be accurately determined. Hence it is possible to determine if a certain reaction has taken place by the half-lives present. This method was used for the $B^{10}(He^3,t)C^{10}$ and $C^{12}(He^3,n)O^{14}$ reactions. However, this means of identification becomes difficult if more than three radioactive nuclei, with comparable half-lives, are produced simultaneously. This difficulty can sometimes be overcome by coincidence measurements in high yield reactions.

(ii) A radioactive nuclide emits particles with an energy characteristic of its decay. Observations of these can determine specifically the unstable nuclide and so the reaction taking place e.g. $C^{12}(He^3,n)O^{14}$. The O^{14} nucleus decays to N^{14} with the emission of a 2.31 MeV γ-ray (see section 3.2). However, the existence of the 2.31 MeV γ-ray does not categorically determine the existence of the O^{14} nucleus, only the 2.31 Mev -ray of half-life 72 secs achieves this fact.

(iii) The cross section of the reaction that has taken place can be related readily to the yield of the particles from the radioactive decay.

The technique is most powerful when the incident beam is mono-energetic and can be controlled in energy. High energy resolution

can then be obtained by using thin targets and making measurements as a function of the beam energy. If, on the other hand, the beam is monoenergetic but cannot be so controlled, a method known as the staked foil technique can be used. In this method the target is a stack of thin foils through which the beam is passed. As the beam passes through the stack, it loses energy. Hence a complete excitation function can be measured after one irradiation. However, energy straggling of the beam in the foils is severe and the energy resolution is poor.

In the past the majority of activation analysis investigations have been carried out with protons and neutrons, only a little done with He^3 because the availability of He^3 gas to bombard targets was a late development. When He^3 gas became available in large quantities and at a reasonable cost, the detailed study of He^3 induced reactions became possible.

Analysis of Data

As a comprehensive discussion is given in (Je 64), only the outlines will be given here to illustrate the means of determining the cross sections in Chapter III.

When a material is bombarded by a beam of nuclear particles some of the nuclei present will interact with the incident particles if the threshold energy is exceeded. (These nuclei may be different isotopes of the same element or different elements entirely, depending

on the actual reaction taking place. In many cases the product nuclei are radioactive. If the activity which is produced by one reaction can be distinguished from all other activities present then the amount of this induced activity is a measure of the reaction cross section.

It has been shown (Je 64) that the cross section (σ) is given, for constant beam current, by:

$$\sigma = \frac{Y \lambda M t_1 \ 1.6 \times 10^{-19}}{I(\varepsilon P)(1-e^{-\lambda t_1})(e^{-(t_2-t_1)\lambda} - e^{-(t_3-t_1)\lambda})} \ cm s^2 \quad \ldots (1)$$

where Y = Yield of Radioactive nuclei.

λ = Decay constant of the radioactive nuclei.

M = Mass of target nucleus.

t_1 = Bombarding time .

I = Charge collected in C.

ε = Detection efficiency of counter.

P = Peak to total ratio of counter.

(t_3-t_2) = Time of detection with counter.

All the quantities on the right hand side can be experimentally determined or are tabulated. Hence the cross section can be calculated.

Sensitivity

If irradiation is carried out for a sufficient number of half-lives of the produced radioactive nuclei that the factor $(1-e^{-\lambda t_1})$ of equation (1) becomes close to unity and if the activity present is determined within a small fraction of a half-life after the

FIG.5. The build up of activity on a target as a function of time. (Constant current assumed).

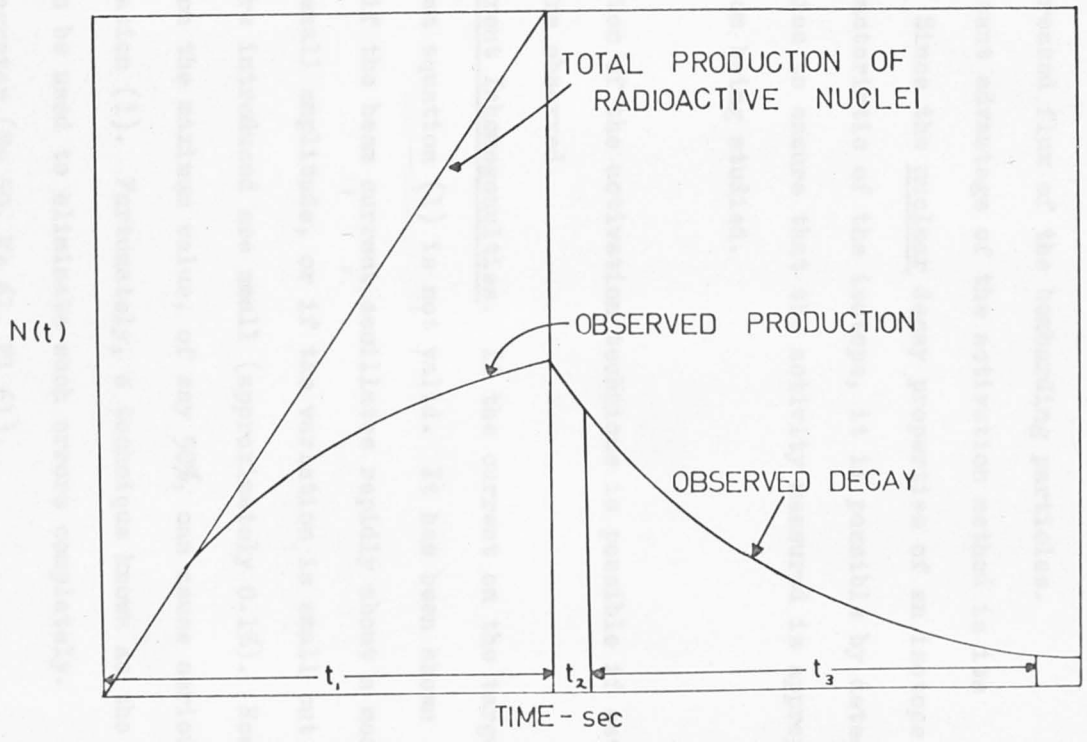
TOTAL PRODUCTION OF
RADIOACTIVE NUCLEI
N(t)
OBSERVED PRODUCTION
OBSERVED DECAY
t1
t2
t3
TIME - sec

FIG. 5.

irradiation ceases, then the sensitivity of the activation technique increases with

(i) Increased detection efficiency of the equipment.

(ii) Increased reaction cross section.

(iii) Increased flux of the bombarding particles.

An important advantage of the activation method is its specificity. Since the nuclear decay properties of an isotope are uniquely characteristic of the isotope, it is possible by detecting these properties to ensure that the activity measured is appropriate to the reaction being studied.

Difficulties

Application of the activation technique is possible if several precautions are observed.

(i) Current Inhomogenuities. If the current on the target is not steady then equation (1) is not valid. It has been shown (Je 64) that if the beam current oscillates rapidly about a mean value with a small amplitude, or if the variation is small but linear, then the errors introduced are small (approximately 0.1%). However, deviations from the maximum value, of say 50%, can cause serious errors in equation (1). Fortunately, a technique known as the leaky integrator can be used to eliminate such errors completely.

The Leaky Integrator (Sn 50, Ke 61, Fl 61).

The situation required for the application of equation (1) is depicted in figure 5 where the yield curve as a function of time

FIG.6. A schematic representation of the leaky integrator circuit.

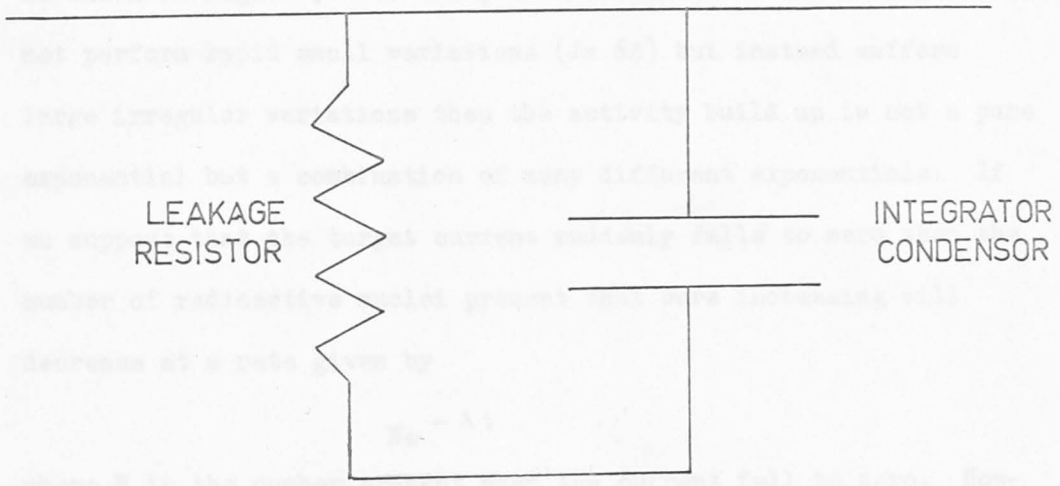

FIG. 6.

is plotted assuming constant bombarding flux. During the 'beam on' period the build up of activity on the target is given by

$$N = N_{\infty}(1 - e^{-\lambda t}) \qquad (2)$$

where N is the number of radioactive atoms present at time t

N_{∞} is the number of radioactive atoms present at t = .

For a constant current this build up is a pure exponential as shown in figure 5. However, if the current is not steady or does not perform rapid small variations (Je 64) but instead suffers large irregular variations then the activity build up is not a pure exponential but a combination of many different exponentials. If we suppose that the target current suddenly falls to zero then the number of radioactive nuclei present that were increasing will decrease at a rate given by

$$Ne^{-\lambda t}$$

where N is the number present when the current fell to zero. However the charge collected (I) will not decay away in the normal current integrator and equation (1) will become invalid. Hence the use of the usual current integrator to normalise the yield of the reaction is not possible in the case of random fluctuations in the current. In order to annul the effects of any current fluctuations a leaky integrator can be constructed by shunting the integrating condensor of a normal current integrator with a resistor of such a value that the decay constant of the RC circuit so produced is

FIG.7. The build up of charge using the leaky integrator technique. (Constant current assumed).

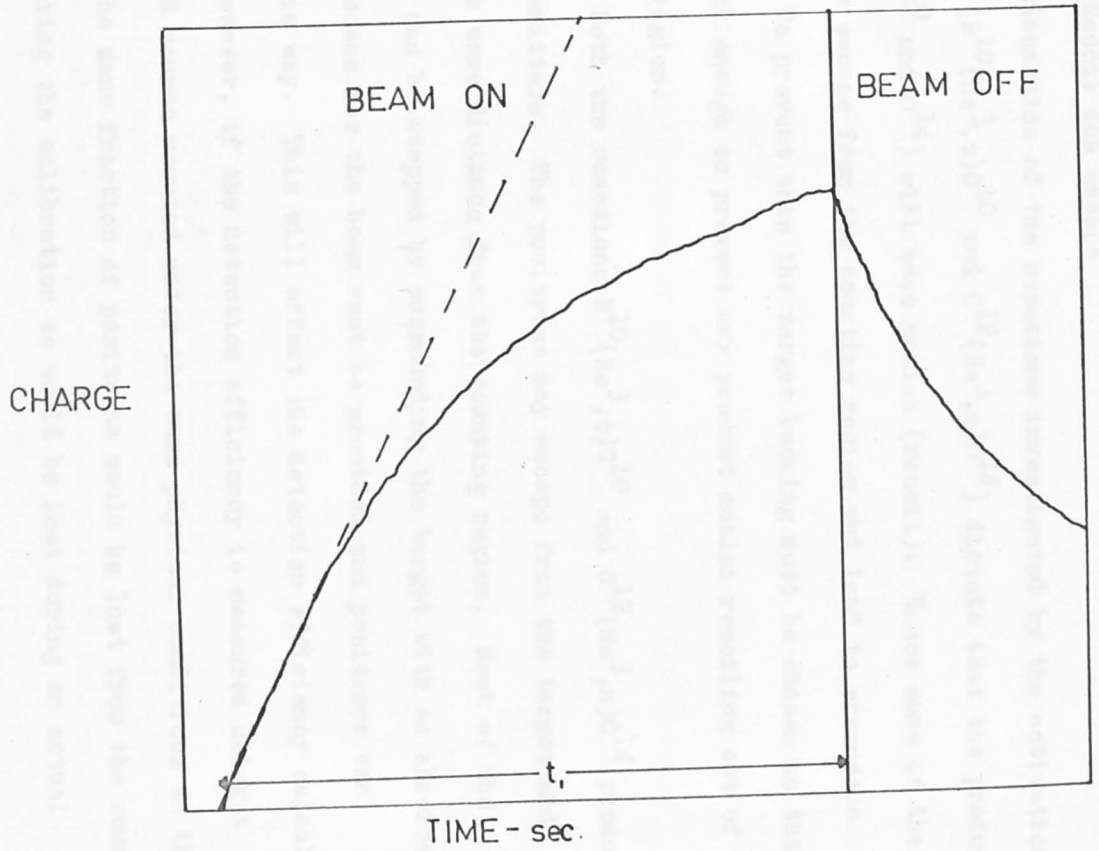

FIG. 7.

the same as the radioactive nuclei under observation. Hence, this leaky integrator provides a means of following the level of radioactivity produced at the target. The charge build up is shown in figure 7.

(ii) Recoil ion escape

The kinematics of the reactions investigated by the activation technique ($B^{10}(He^3,t)C^{10}$ and $C^{12}(He^3,n)O^{14}$) dictate that the product nuclei (C^{10} and O^{14}) will have motion (recoil). Hence some of these nuclei may escape from the counting region and lead to erroneous results. To prevent this the target backing must be chosen so that it is thick enough to prevent any product nuclei recoiling out of the counting region.

(iii) Both the reactions $B^{10}(He^3,t)C^{10}$ and $C^{12}(He^3,n)O^{14}$ produce positron emitters. The positrons may escape from the target and annihilate some distance from the counting region. Most of the positrons can be stopped by surrounding the target with an absorber. However access for the beam must be provided and positrons can escape this way. This will effect the detection efficiency calculations. However, if the detection efficiency is measured using a calibrated source mounted under the same physical conditions as the targets the same fraction of positrons would be lost from the counting region during the calibration as would be lost during an actual experiment.

Applications

(i) The activation technique is a useful method of investigating many reactions. It is especially useful when the emitted reaction particles are neutrons for no really satisfactory directional neutron counter is available. It is therefore difficult to discriminate between reaction and background neutrons. The technique is also very useful for distinguishing between simple and complex reactions such as (a, b) and (a, 2b) respectively. A third type of measurement where the activation technique can be useful is in cases where it is difficult to separate the charged reaction particles of interest from other charged particles.

(ii) The distribution of the elements in the earth's crust and in meteorites has an important bearing on the origins of the solar system. The ratios of the elements present may be found accurately by the activation technique.

(iii) The composition of mammalian organs.

(iv) The production of radio-isotopes, mainly by (n, γ) reactions.

1.4 The Low-lying Al^{27} Levels

As will be seen in Chapter IV the low lying levels of Al^{27} were investigated via the Mg^{26} (p, γ) reaction. In this section the theoretical background is discussed.

The Mg^{26} (p, γ) reaction exhibits typical Bohr compound

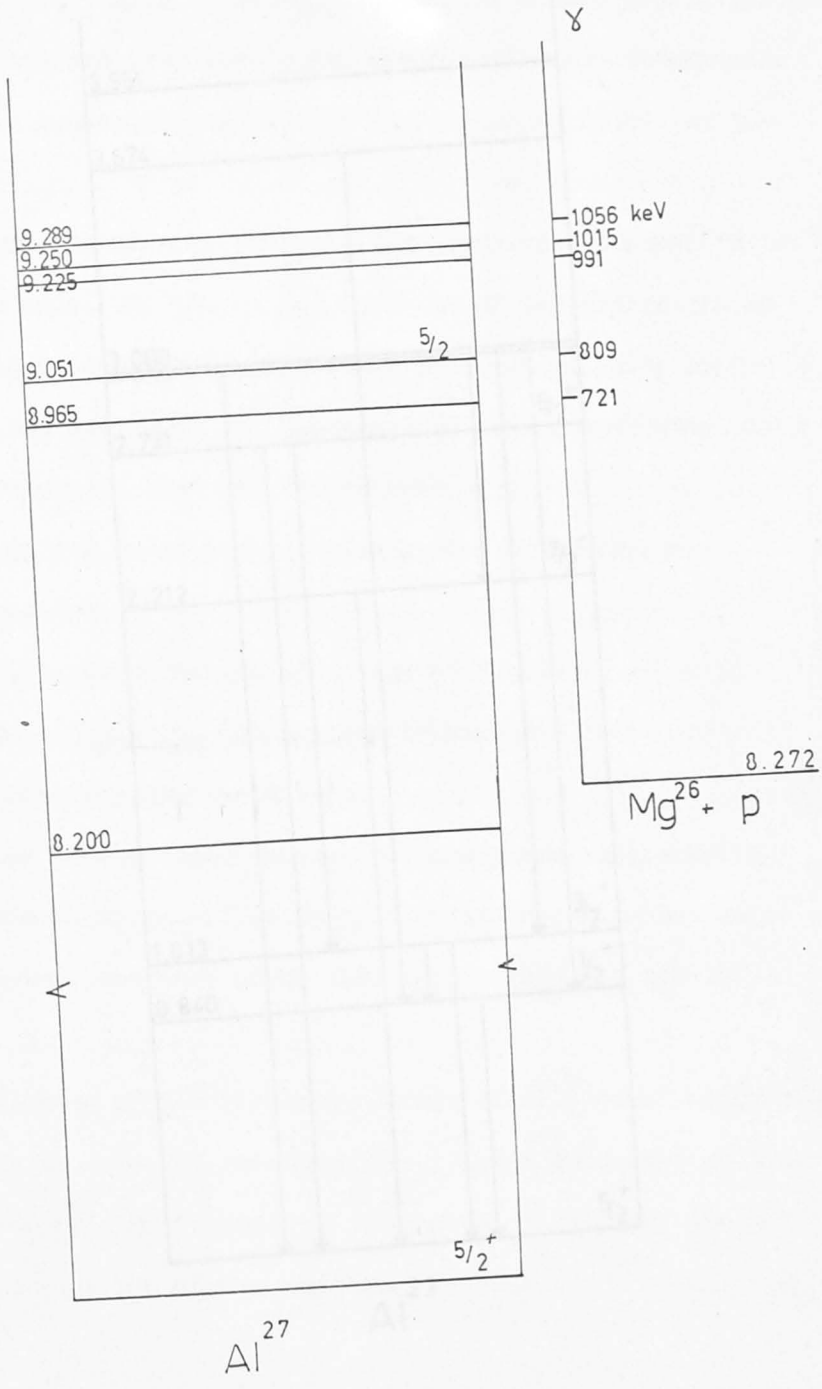
γ
1056 keV
1015
991
809
721
8.272
Mg26 + p
9.289
9.250
9.225
5/2
9.051
8.965
8.200
5/2+
Al27

FIG. 8.

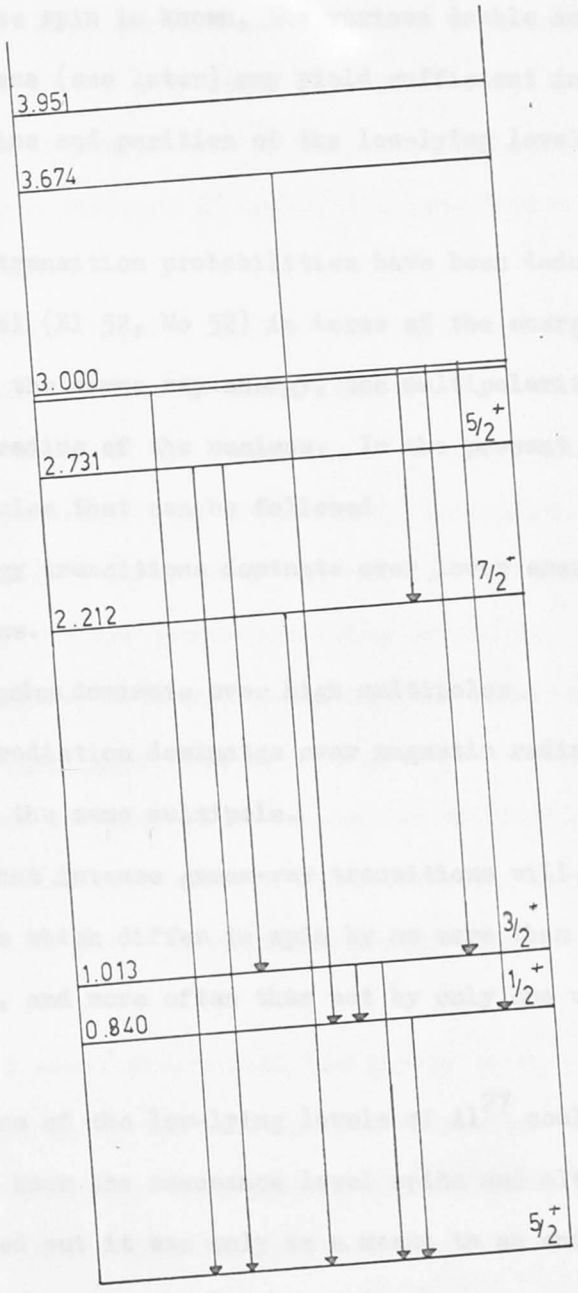

FIG. 9.

nucleus resonances. Figure 8 shows the reaction in the region of interest and figure 9 the low energy region of the Al^{27} nucleus.

If the resonance spin is known, the various double and triple gamma-ray correlations (see later) may yield sufficient information to determine the spins and parities of the low-lying levels of the nucleus.

The gamma-ray transition probabilities have been deduced on the single particle model (Bl 52, Mo 52) in terms of the energy of the transition (E) i.e. the gamma-ray energy, the multipolarity of the transition and the radius of the nucleus. In the present case there are three general rules that can be followed

(i) High energy transitions dominate over lower energy transitions.

(ii) Low multipoles dominate over high multipoles .

(iii) Electric radiation dominates over magnetic radiation when both have the same multipole.

This implies that intense gamma-ray transitions will usually occur between states which differ in spin by no more than two units of angular momentum, and more often than not by only one unit of spin.

Before the spins of the low-lying levels of Al^{27} could be deduced it was necessary to know the resonance level spins and although this was therefore carried out it was only as a means to an end; the end being the spin and parity of the low-lying levels.

Angular Correlations

The measurement of angular correlations of the gamma-radiations emitted following particle capture constitutes a powerful technique for determining some of the properties of excited nuclear states. Definition. An angular correlation is the relative yield of the reaction products as a function of angle, the beam direction being the reference direction.

Angular correlation studies have become important for nuclear level and reaction studies for two main reasons, viz.

(i) The improvement in the technique of studying angular correlations. The probability of detection in coincidence of two radiations of a cascade depends on the product of the efficiencies of the two detectors for the gamma-rays being detected. As long as relatively low efficiency detectors were used the measurement of angular correlations was very tedious indeed. The use of scintillation NaI(Tl) counters has changed the situation completely. Not only has time been saved with these greater efficiency counters but the selection of particular gamma-transitions has greatly widened the scope of the work.

(ii) There is a sound theoretical background to support the experimental data and allow the data to be interpreted. The theories of angular distributions have been extensively reviewed (De 57, Bi 60, Go 59). The theoretical interpretation of the results has been made comparatively easy by compilations such as (Fe 62) and these

FIG.10. A schematic representation of an experimental arrangement for measuring a double correlation.

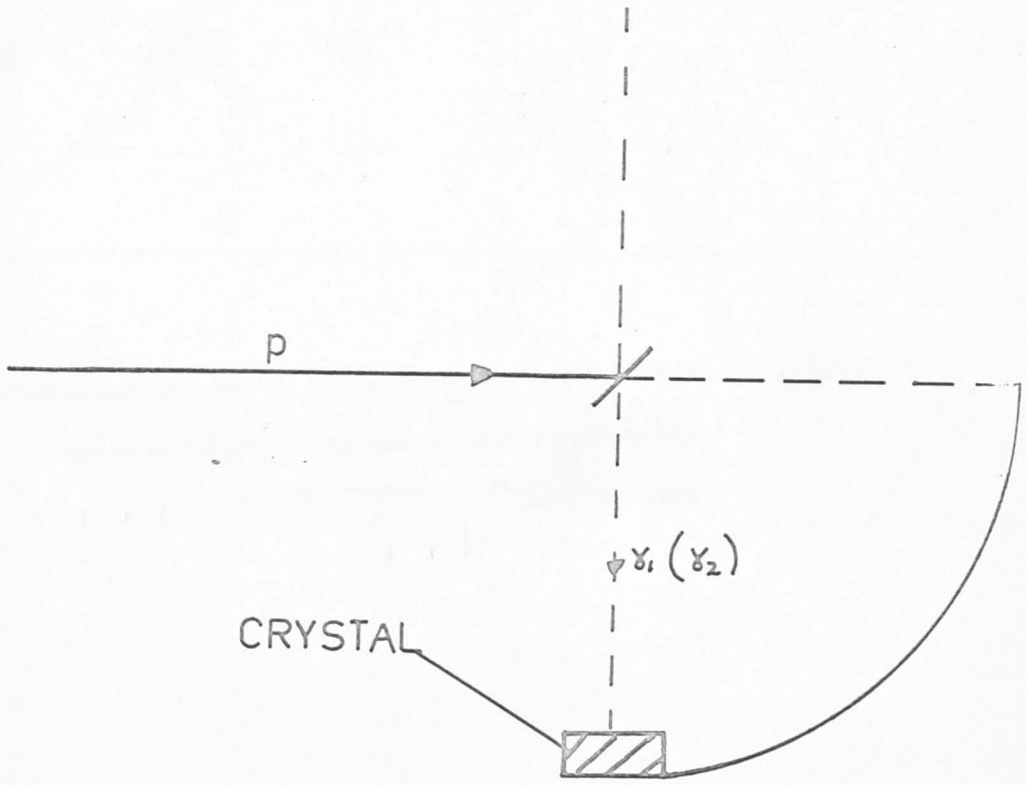

FIG. 10.

FIG.11. A schematic representation of an experimental arrangement for measuring a triple angular correlation.

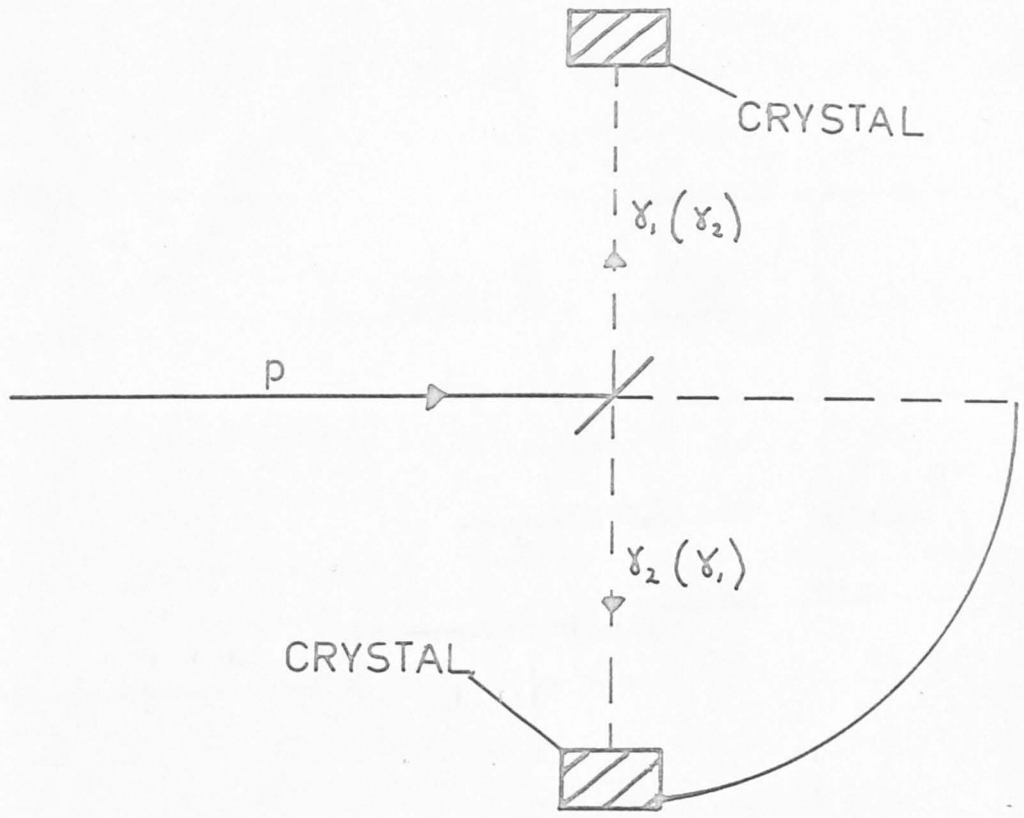

FIG. 11.

FIG.12. The $(p,\gamma\gamma)$ process.

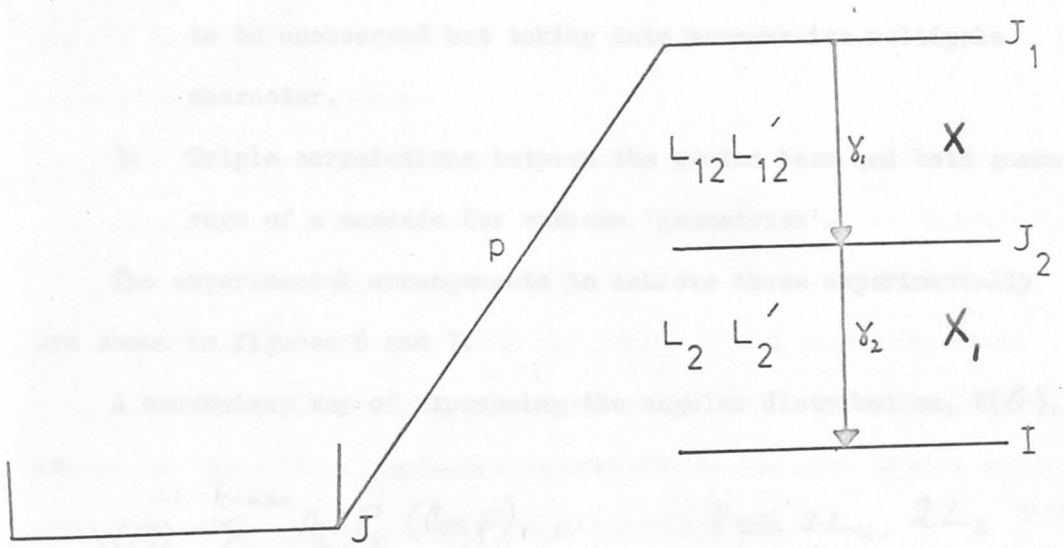

FIG. 12.

tables were used throughout the present work on the $Mg^{26}(p, \gamma)$ reaction. The tables are compiled such that theoretical expressions can be obtained for

1. A double correlation between the proton beam and the 1st gamma-ray of a cascade.
2. A double correlation between the proton beam and the 2nd gamma-ray of a cascade, assuming the 1st gamma-ray to be unobserved but taking into account its multipole character.
3. Triple correlations between the proton beam and both gamma-rays of a cascade for various 'geometries'.

The experimental arrangements to achieve these experimentally are shown in figures 6 and 7.

A convenient way of expressing the angular distribution, $W(\theta)$, is

$$W(\theta) = \sum_{k=0}^{k=max} A_k P_k (\cos\theta) \qquad k \leq 2L_{12}, 2L_2 \quad \ldots\ldots(2)$$

where $P_k (\cos\theta)$ are the legendic polynomials of order k and A_k contains the physics of the correlation. It is A_k, or some factor proportional to A_k that is tabulated. L_1, L_2 are the multipoles of the gamma-rays involved (see figure 8).

Double Correlations

The correlation of the gamma-radiation with respect to the beam of charged particles is often referred to as a double correlation

and is the type of correlation most readily measured. The simplest double correlations to interpret are those which result from the capture of alpha particles by even-even nuclei since only the unknown spins of the states together with the unknown quadrupole-dipole amplitude ratio of the radiation are involved in the calculation of the correlation coefficients. In this case the capture state must have the parity of the orbital angular momentum of the captured alpha particle since even-even nuclei and alpha particles have even parity.

The next most simple type of correlation to interpret and one which has been extensively used (La 55, Le 56) is the correlation of gamma-rays from the capture of protons by even-even nuclei e.g. Mg^{26} (p.γ) Al^{27}. In this case the parity of the capturing state cannot be deduced from its spin alone since there are two adjacent values of the orbital angular momentum of the captured proton possible for each value of the nuclear angular momentum.

The interpretation of double correlations measured for the proton bombardment of a non-zero spin nucleus are more complex as, apart from the parameters mentioned above, there is the possibility of channel spin mixtures, which can vary from 0 to infinity and multipole interference (LL^1).

Polarisation Correlations

In principle the electric or magnetic nature of the transition can be determined with a detector system sensitive to the plane of

polarisation of the gamma-radiation. Two processes so sensitive are the photo-disintegration of the deuteron and the Compton scattering process. A quantity commonly measured is the Compton scattered gamma-rays at 0° to the plane defined by the beam and the gamma-ray to those at 90° to this plane. ($\frac{N_0}{N_{90}}$)

Then $\frac{N_0}{N_{90}} \propto$ Polarisation.

Triple correlations

It is possible to produce a striking simplification of a gamma-ray spectrum from a resonance by observing the gamma-rays in coincidence with selected gamma-rays. The correlation between two gamma-rays and the particle beam is called a triple correlation. The coincidence counting rate as a function of angle when one of the detectors is fixed with respect to the charged particle beam depends upon the geometrical arrangement as well as on the nuclear parameters. It is therefore possible to obtain experimentally more information than in the case of the double correlation since the same nuclear parameters apply to all the arrangements.

In practice triple correlations are measured using definite arrangements of the detectors with respect to the target and incoming beam. Each arrangement is called a 'geometry'. A geometry consists of a correlation between one gamma-ray of the cascade in a fixed direction and the other gamma-ray in a variable direction. Application of these geometries together with the double correlations

can usually resolve any difficulties with regard to the nuclear level or levels under discussion. The various geometries are given in Table 1. (Fe 62).

TABLE 1.

GEOMETRY	12	2	
I	Variable	90°	180°
II	90°	Variable	180°
III	Variable	0°	0°
IV	0°	Variable	0°
V	90°	90°	Variable
VI	90°	Variable	90°
VII	Variable	90°	90°

In the present work on Al^{27} levels only geometries I and II were employed.

Fig. 8 is a schematic representation of the experimental situation in the present case of the Mg^{26} (p.γ) reaction.

The theory dictates the following. (Ref. Fig. 8).

(i) The double correlation between p and γ_1 will depend on J_1, J_2, L_{12}, L_{12}' and X_1 only.

X_1 is the $\frac{\text{quadrupole}}{\text{dipole}}$ mixing ratio for γ_1.

(ii) The double correlation between p and γ_2 will depend on J_2, I, L_2, L_2', X_2 and X_1.

(iii) The triple correlations between p, γ_1 and γ_2 will depend on J_1, J_2, I, L_2, L_2', L_{12}, L_{12}', X_1 and X_2.

In the present experiments I was known in all cases.

Gamma ray selection rules dictate the following for a γ-transition between two levels of angular momentum J_1, J_2 and parity π_1, π_2 respectively.

(i) $$|J_1 - J_2| \leq L \leq |J_1 + J_2|$$

where L is the angular momentum in integral units of $\hbar$ removed by the radiation. This is really the conservation of momentum principle.

(ii) For electric transitions

$$\Delta\pi = (-1)^L$$

For magnetic transitions

$$\Delta\pi = (-1)^{L+1}$$

where $\Delta\pi$ is the parity difference between the two levels.

If $\Delta\pi = -1$ there is a parity change of sign

$= +1$ there is no parity change of sign.

The analysis of the experimental data was as follows:-
It was assumed that only dipole and quadrupole radiation was present. Then reasonable values of J_1 and J_2 were assumed so that the theoretical expressions could be compiled. This enabled the experimental double correlation (p, γ_1) to provide us with a range of values of X_{21}. This then permitted a theoretical prediction of the (p, γ_2) double correlation and hence a range of values for X_{21} to be obtained. Also the theoretical triple correlations ($p, \gamma_1 \gamma_2$, GEOMETRIES I and II) when compared with experiment gave a range of values of X_{21}. For the assumed sequence to be acceptable the values of X_{21} must overlap. Unfortunately if more than one set of J_1, J_2 values gave consistent results there was no way of distinguishing between them in the present work, unless a different cascade

(J_1, J_2', I') could determine J_1. However, it is possible for the sequences (J_1, J_2, I) and $(J_1 \longrightarrow J_2'' \longrightarrow I)$, where J_2 and J_2'' refer to the same Al^{27} level, to both give consistent results. This difficulty can be resolved if the mixing ratios are very different for the two sequences.

Geometrical Corrections To Angular Correlations.

A measured γ-ray angular distribution is generally fitted by the method of least squares to a Legendre polynomial expansion in order to compare the coefficients with theoretical ones calculated as described previously. Before such a comparison is made, however, it is necessary to take account of the finite solid angle subtended at the target by the detector. The correction for cylindrical crystals of NaI(Tl) has been derived by Rose (Ro 53). If the theoretical correlation is given by equation (2) then the measured correlation will have coefficients given by

$$\frac{a_k'}{a_o} = \frac{J_k}{J_o} \frac{a_k}{a_o} \quad \cdots \quad (3)$$

where J_k/J_o is the correction factor and is less than unity.
If a triple correlation is measured, the correction factor contains the product of two coefficients, each appropriate to each detector. The J_k/J_o factors have been tabulated (Go 58) on the assumption that all the pulses produced by the interaction between a γ-ray of given energy and the detector are detected and included in the analysis of the data. The geometrical correction factors are given in the text where appropriate.

* * * * * * * * * *

CHAPTER II

Gamma - Rays.

The experimental work of this thesis involved the detection of γ-rays with NaI (Tl) spectrometers. These are described in this chapter.

2.1 Single Crystals

Gamma rays interact with matter by one of three main processes. These are utilized in γ-ray spectroscopy and have an important part to play in the performance of detectors and the interpretation of results. Hence they will be reviewed briefly.

(i) The photo-Electric Effect. (Fig.13)

The γ-ray is absorbed by a bound electron in atom with the result that the electron is ejected from the atom with an energy E given by

$$E = E' - B \quad . \quad . \quad . \quad . \quad . \quad (4)$$

where B is the binding energy of the electron to the atom

E' is the gamma-ray energy.

The process is followed by re-capture of the electron to give rise to the scintillation (unfortunately this part of the process is not well understood). The cross section (σ) for the photo-electric effect is given by

$$\sigma \propto \frac{Z^n}{(E')^{n'}} \quad . \quad . \quad . \quad . \quad . \quad (5)$$

where Z is the charge on the nucleus

n varies from 4 to 5 depending on E'

n' is about 3.

FIG.13. The three major absorption processes for gamma-rays in NaI(Tl) detectors considered in this thesis.

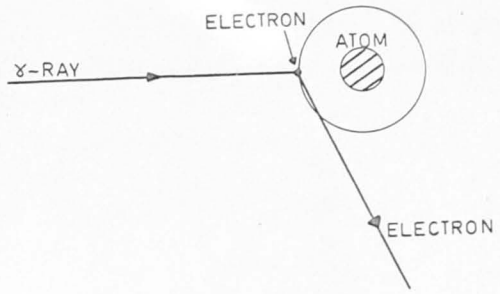

PHOTOELECTRIC EFFECT

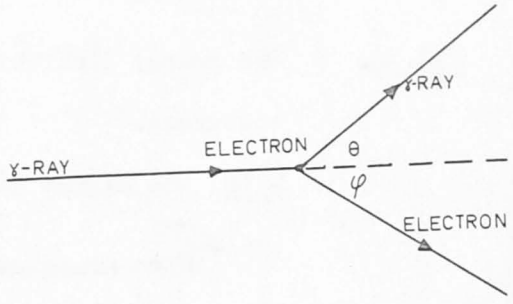

COMPTON EFFECT

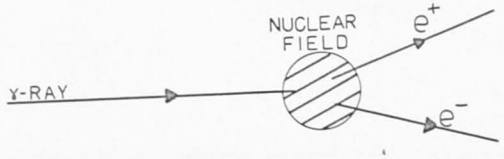

PAIR PRODUCTION

FIG. 13.

FIG.14. The energy distribution of Compton scattered electrons.

NOTE the marked variation in the low energy tail.

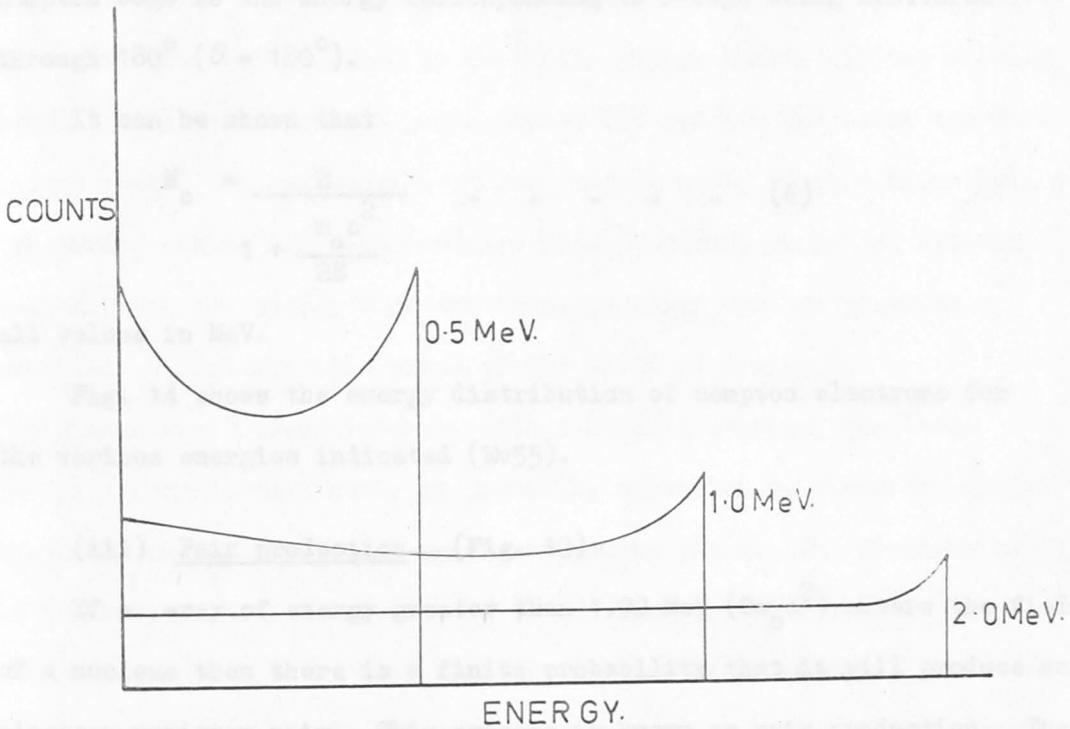

FIG. 14.

(ii) The Compton Effect (Fig. 13)

Here the gamma-ray is inelastically scattered by one of the virtually free electrons in the crystal. Hence not all the γ-ray energy can be absorbed by one interaction. The energy of the scattered electron ranges from zero to the so-called compton edge (E_c). The compton edge is the energy corresponding to γ-rays being scattered through 180° ($\theta = 180^\circ$).

It can be shown that

$$E_c = \frac{E}{1 + \frac{m_o c^2}{2E}} \quad . \quad . \quad . \quad . \quad . \quad (6)$$

all values in MeV.

Fig. 14 shows the energy distribution of compton electrons for the various energies indicated (Ev55).

(iii) Pair production. (Fig. 13)

If a -ray of energy greater than 1.02 MeV ($2m_o c^2$) enters the field of a nucleus then there is a finite probability that it will produce an electron-positron pair. This process is known as pair production. The probability of the effect occurring increases approximately as the logarithm to the base e of twice the γ-ray energy. Any γ-ray energy in excess of 1.02 MeV is carried off as kinetic energy of the outgoing pair.

All of the interactions mentioned previously can contribute to the pulse height spectrum when -rays are incident on a NaI (T1) crystal. The photo-electric emission of the K electrons from iodine atoms with

subsequent absorption of the K X-radiation results in the so-called "full-energy" peak. At lower pulse-heights there is a continuous distribution due to Compton scattering at various angles with escape of the scattered γ-rays. For energies greater than 1.02 MeV the pair production process can occur, with annihilation of the positron to two 0.511 MeV γ-rays. If both 0.511 γ-rays are absorbed by the crystal there is a further addition to the "full energy peak". If one or both annihilation γ-rays escape peaks result 0.5 and 1.0 MeV below the full energy peak. The combination of full energy peak, Compton distribution and escape peaks, all with gaussian distributions, gives the relationship between the energy E of the incoming γ-ray and the spectrum obtained; called the line shape of the γ-ray of energy E.

Hence when γ-rays interact with a NaI(Tl) crystal, the γ-ray photon energy is completely or partially converted to electron energy depending on the absorption processes taking place. The electron energy is transformed back to photons of an energy detectable with a photo-multiplier. In this complex process, one photon of energy E is transformed into a light pulse of roughly fixed energy but with an <u>intensity</u> almost directly proportional to the energy deposited in the crystal.

To consider line shapes more thoroughly γ- rays can be divided into two energy regions:- Those with energy below 1.02 MeV and those above 1.02 MeV.

<u>Case I</u> γ-ray energy below 1.02 MeV.

In this region only the photo-electric and compton scattering processes can take place. An absorption by the photo-electric process

FIG.15. A typical line shape for a gamma-ray below 1.02 MeV.

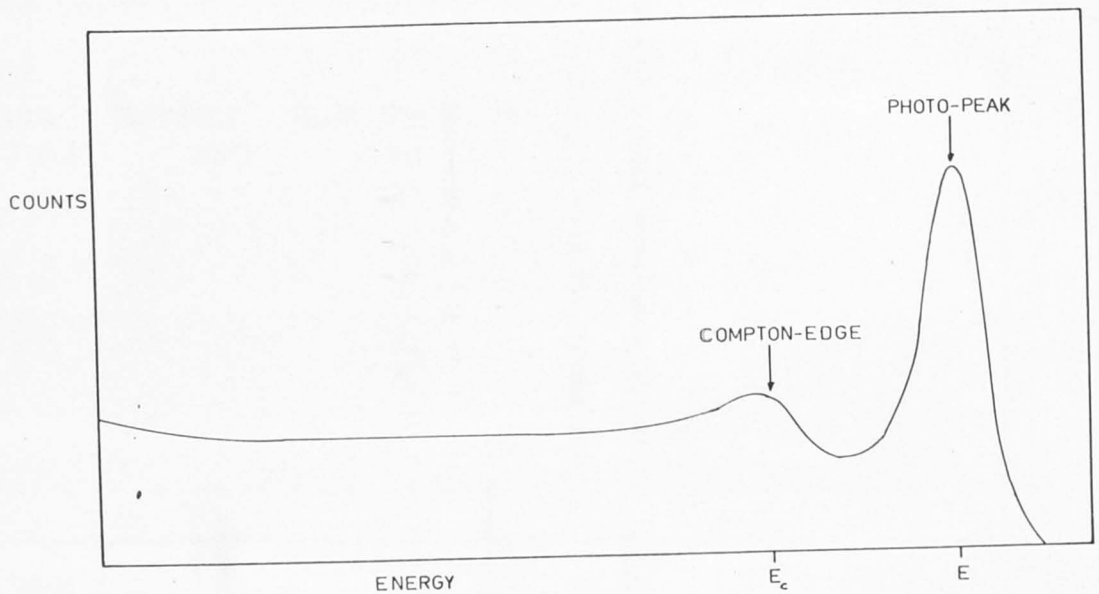

FIG. 15.

FIG.16. a. An idealised line shape for a gamma-ray of about 2.5 MeV.

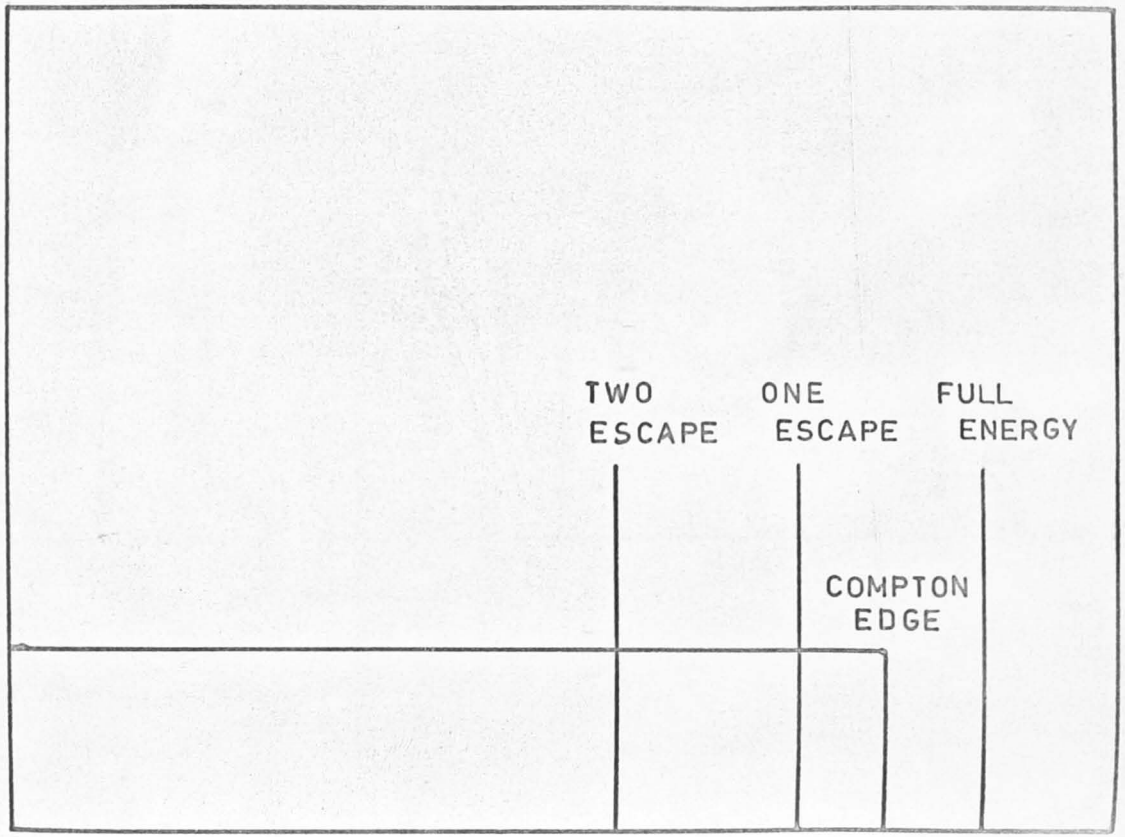
TWO
ESCAPE
ONE
ESCAPE
FULL
ENERGY
COMPTON
EDGE

FIG.16. b. A practical line shape for a gamma-ray of 2.61 MeV with 5" x 4" NaI(Tl) detectors. III

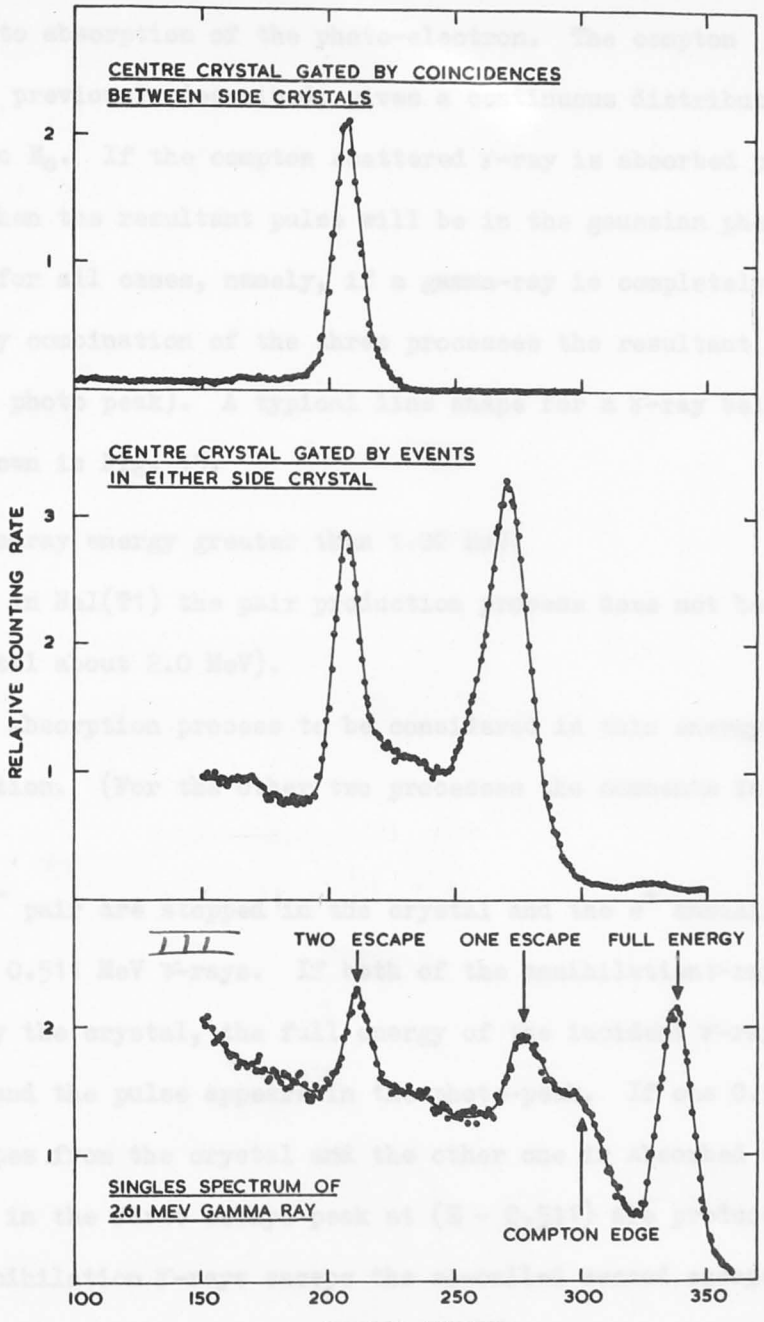
CENTRE CRYSTAL GATED BY COINCIDENCES
BETWEEN SIDE CRYSTALS
CENTRE CRYSTAL GATED BY EVENTS
IN EITHER SIDE CRYSTAL
RELATIVE COUNTING RATE
TWO ESCAPE
ONE ESCAPE
FULL ENERGY
SINGLES SPECTRUM OF
2.61 MEV GAMMA RAY
COMPTON EDGE
100
150
200
250
300
350
CHANNEL NUMBER

gives rise to pulses in the so-called photo-peak (or full energy peak) corresponding to absorption of the photo-electron. The compton scattering, as previously described, gives a continuous distribution of pulses up to E_c. If the compton scattered γ-ray is absorbed photo-electrically then the resultant pulse will be in the gaussian photo-peak. (This is true for all cases, namely, if a gamma-ray is completely absorbed by any combination of the three processes the resultant pulse will be in the photo peak). A typical line shape for a γ-ray below 1.02 MeV is shown in Fig. 15.

Case II Gamma-ray energy greater than 1.02 MeV.

(Actually in NaI(T1) the pair production process does not become significant until about 2.0 MeV).

The extra absorption process to be considered in this energy range is pair production. (For the other two processes the comments in Case I apply).

The e^+, e^- pair are stopped in the crystal and the e^+ annihilates to produce two 0.511 MeV γ-rays. If both of the annihilation γ-rays are absorbed by the crystal, the full energy of the incident γ-ray has been absorbed and the pulse appears in the photo-peak. If one 0.511 MeV γ-ray escapes from the crystal and the other one is absorbed completely pulses in the first escape peak at (E - 0.511) are produced. If both the annihilation γ-rays escape the so-called second escape peak at (E - 1.02) is produced. In addition there will be an underlying compton distribution. The ideal result is shown in Fig. 16a. and the practical case in Fig 16b. for an approximately 5 MeV gamma-ray.

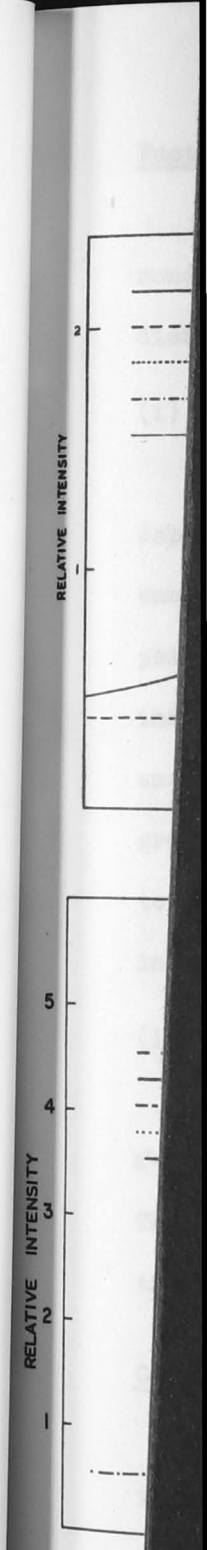

FIG.17. Typical line shapes obtained with 5" x 4" NaI(Tl) detectors for mono-energetic gamma-rays.

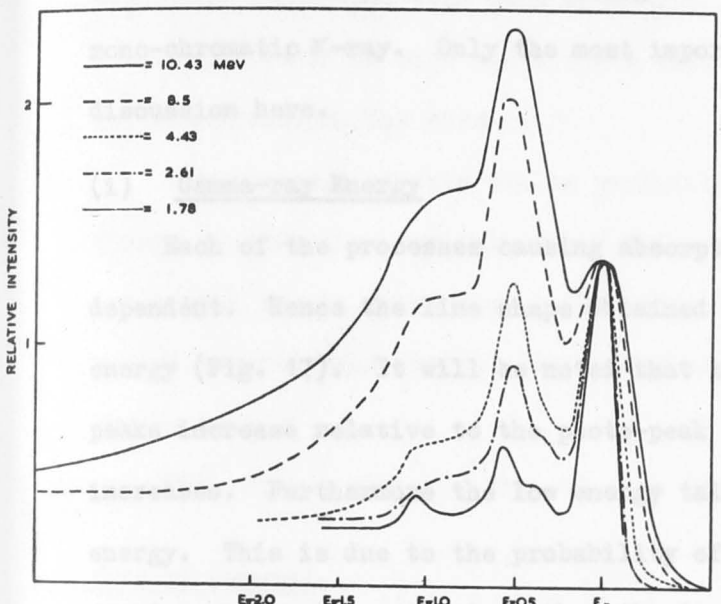
= 10.43 MeV
= 8.5
= 4.43
= 2.61
= 1.78
RELATIVE INTENSITY
GAMMA RAY ENERGY MeV

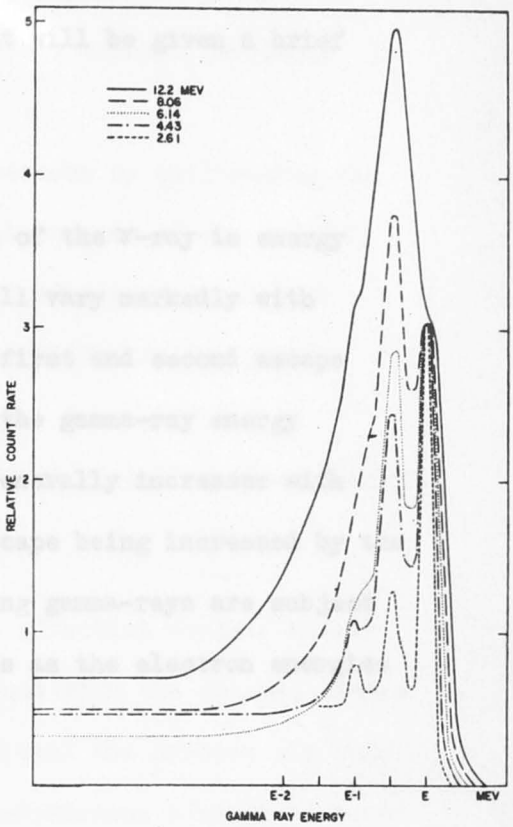
12.2 MEV
8.06
6.14
4.43
2.61
RELATIVE COUNT RATE
GAMMA RAY ENERGY
MEV

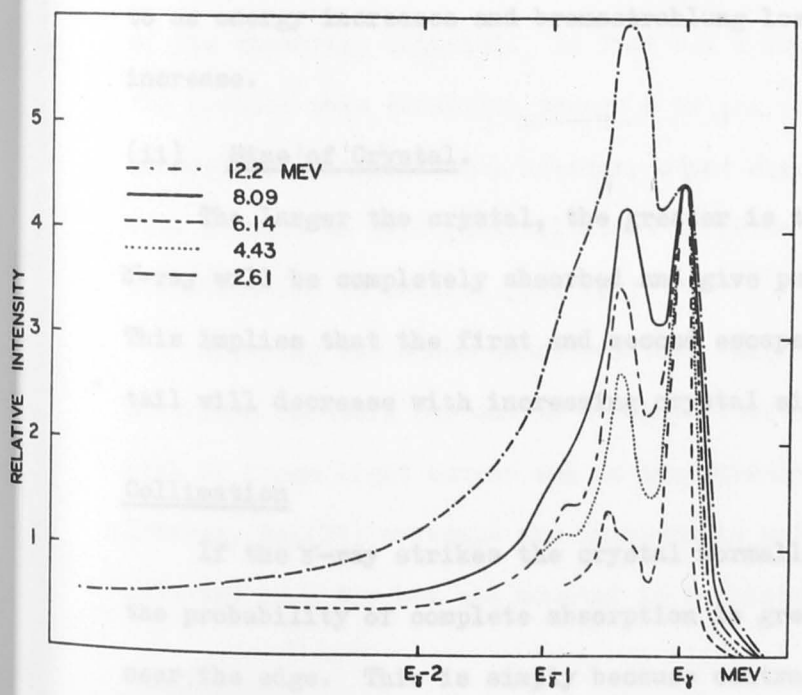
12.2 MEV
8.09
6.14
4.43
2.61
RELATIVE INTENSITY
MEV

Factors effecting the line shape.

There are many factors effecting the line shape of a detected mono-chromatic γ-ray. Only the most important will be given a brief discussion here.

(i) Gamma-ray Energy

Each of the processes causing absorption of the γ-ray is energy dependent. Hence the line shape obtained will vary markedly with energy (Fig. 17). It will be noted that the first and second escape peaks increase relative to the photo-peak as the gamma-ray energy increases. Furthermore the low energy tail generally increases with energy. This is due to the probability of escape being increased by the greater number of scatterings that the incoming gamma-rays are subject to as energy increases and bremsstrahlung loss as the electron energies increase.

(ii) Size of Crystal.

The larger the crystal, the greater is the probability that the γ-ray will be completely absorbed and give pulses in the photo-peak. This implies that the first and second escape peaks and the compton tail will decrease with increasing crystal size.

Collimation

If the γ-ray strikes the crystal normally and near the centre the probability of complete absorption is greater than if it strikes near the edge. This is simply because central incidence provides more crystal for the γ-ray, and secondary γ-rays, to pass through. Hence as the position of incidence moves towards the edge of the crystal the

escape peaks will become more prominent. If the gamma-ray enters obliquely there will also be a greater probability of escape than normal incidence as once again there will be less crystal available for absorption on the average.

The 'escape' effects can be partially overcome by collimating the γ-rays so that they can only enter the central portion of the crystal and normal to its front face. (However, this reduces the number of γ-rays entering the crystal, which may be prohibitive in low yield experiments.

The various parts of Fig. 17 show the effect of collimation clearly.

Type of crystal.

All the absorption effects depend on the effective nuclear charge of the absorbing material. In fact all increase with the charge. Hence the greater this effective charge Z of the crystal the greater the total absorption. In practice, however, other considerations have to be taken into account as well (scintillation efficiency, transparency to own scintillation to mention just two).

Applying the above considerations NaI(T1) is high on the list of materials suitable for use as a γ-ray detector. It has a relatively high Z, large light output and is transparent to its own light output. However, NaI(T1) crystals are hygroscopic and the crystals must be polished in a dry box and mounted in a moisture-proof container.

Conclusions

From the foregoing discussion it follows that complicated spectra

PROTO
BEAM

FIG.18. A typical detector assembly used in the $Mg^{26}(p,\gamma)Al^{27}$ experiments.
(The monitor detector was a 5" x 4" NaI(Tl) crystal).

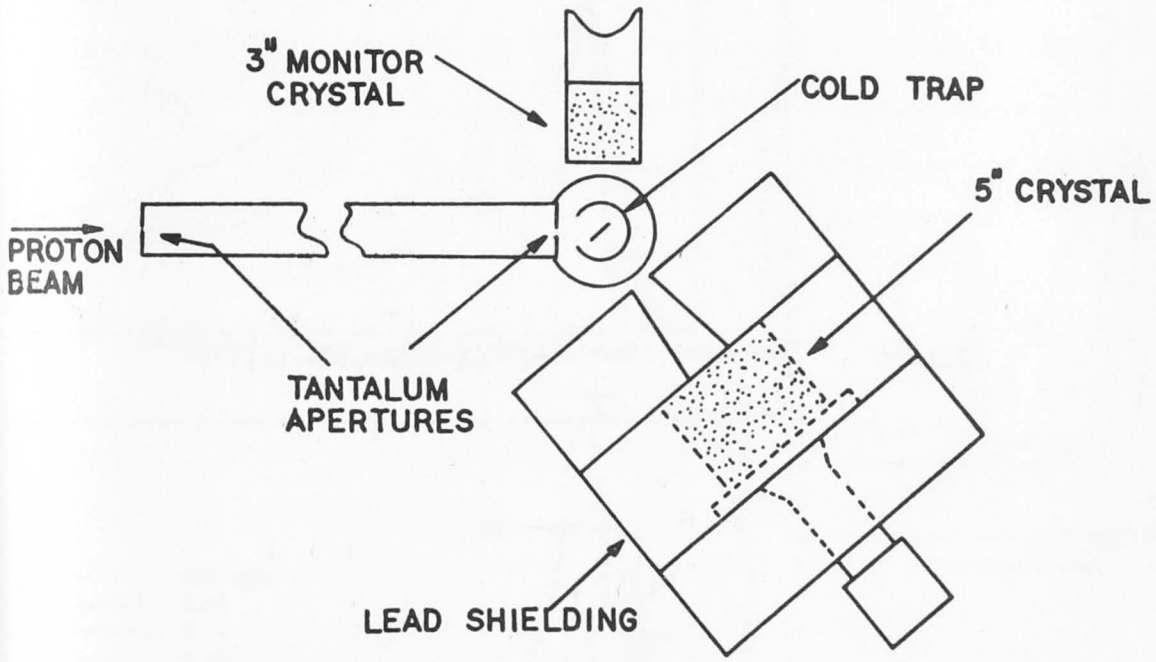
3" MONITOR CRYSTAL
COLD TRAP
5" CRYSTAL
PROTON BEAM
TANTALUM APERTURES
LEAD SHIELDING

FIG.19. Gamma-ray line shapes for the $Mg^{26}(p,\gamma)Al^{27}$ reaction. I

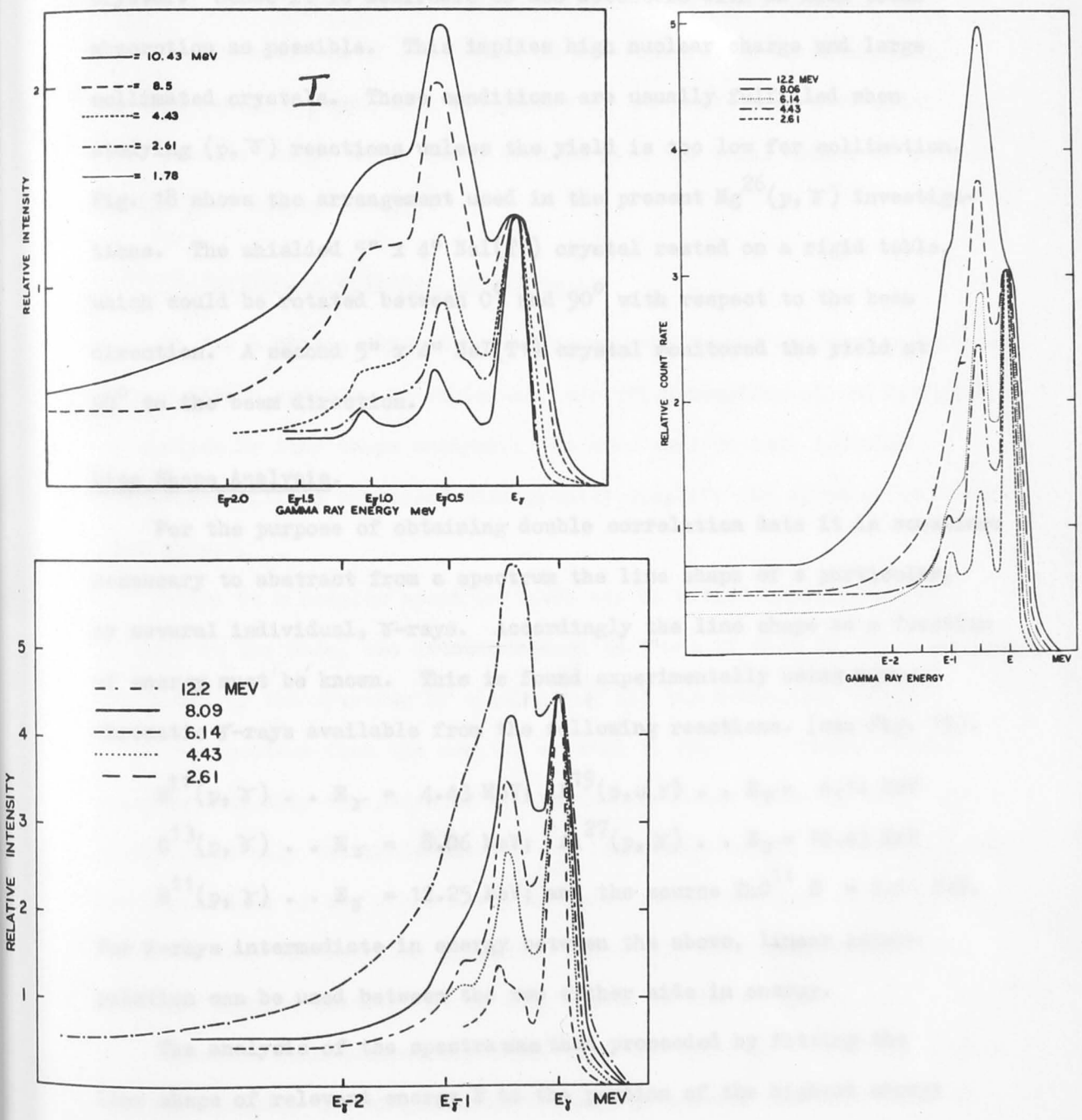
= 10.43 MeV
= 8.5
= 4.43
= 2.61
= 1.78
I
RELATIVE INTENSITY
Eγ2.0
Eγ1.5
Eγ1.0
Eγ0.5
Eγ
GAMMA RAY ENERGY MeV
12.2 MEV
8.09
6.14
4.43
2.61
RELATIVE INTENSITY
Eγ-2
Eγ-1
Eγ
MEV
12.2 MEV
8.06
6.14
4.43
2.61
RELATIVE COUNT RATE
E-2
E-1
E
MEV
GAMMA RAY ENERGY

FIG. 17.

will result when several mono-energetic γ-rays are detected in a single crystal. Hence it is desirable to use detectors with as much total absorption as possible. This implies high nuclear charge and large collimated crystals. These conditions are usually fulfilled when studying (p, γ) reactions unless the yield is too low for collimation. Fig. 18 shows the arrangement used in the present $Mg^{26}(p, \gamma)$ investigations. The shielded 5" x 4" NaI(T1) crystal rested on a rigid table, which could be rotated between 0° and 90° with respect to the beam direction. A second 5" x 4" NaI(T1) crystal monitored the yield at 90° to the beam direction.

Line Shape Analysis.

For the purpose of obtaining double correlation data it is sometimes necessary to abstract from a spectrum the line shape of a particular, or several individual, γ-rays. Accordingly the line shape as a function of energy must be known. This is found experimentally using monochromatic γ-rays available from the following reactions. (see Fig. 19).

$B^{11}(p, \gamma)$ . . E_{γ} = 4.43 MeV; $F^{19}(p, \alpha\gamma)$ . . E_{γ} = 6.14 MeV

$C^{13}(p, \gamma)$ . . E_{γ} = 8.06 MeV; $Al^{27}(p, \gamma)$ . . E_{γ} = 10.43 MeV

$B^{11}(p, \gamma)$ . . E_{γ} = 12.25 MeV; and the source ThC^{11} E = 2.61 MeV.

For γ-rays intermediate in energy between the above, linear interpolation can be used between the two either side in energy.

The analysis of the spectra was then proceeded by fitting the line shape of relevant energy E to the portion of the highest energy line shape uncontaminated by the next lower energy γ-ray. The highest

energy line shape was subtracted out from the spectrum and the process repeated for the remaining highest energy γ-ray. This enabled the relative intensities of the γ-rays in the spectrum to be determined. For low energy γ-rays, only the pulses in the photo-peak were added; the 'peak to total' ratio being used to give the total number of pulses in the line shape. (He 57).

2.2 Particular detector arrangements.

So far a single crystal detecting several γ-rays has been considered. The resultant spectra, as explained, are often complicated and difficult to analyse by line shape analysis. In this section some detector techniques will be discussed that greatly simplify the spectra and γ-ray line shapes.

Often in a complex spectrum there are so called cascade γ-rays. If such is the case, two detectors such as those of Fig. 18 in coincidence can simplify the spectrum by eliminating all non-coincident γ-rays.

The spectrum from the monitor crystal is fed to a single channel analyser and only the pulse of one particular γ-ray selected out. (This often means only the photo-peak of the line shape unless the escape peaks are also clear of any other γ-ray). These pulses are used to gate the spectrum from the rotating crystal. Hence only γ-rays in coincidence with the monitor selected γ-ray will appear in the spectrum.

Unwanted coincidences may arise from the tails of γ-ray line shapes. If, for example, the single channel analyser selects the photo-peak of the lower energy γ-ray of a cascade, pulses from the tail of the higher

FIG.21. Top view of the Three Crystal Spectrometer.

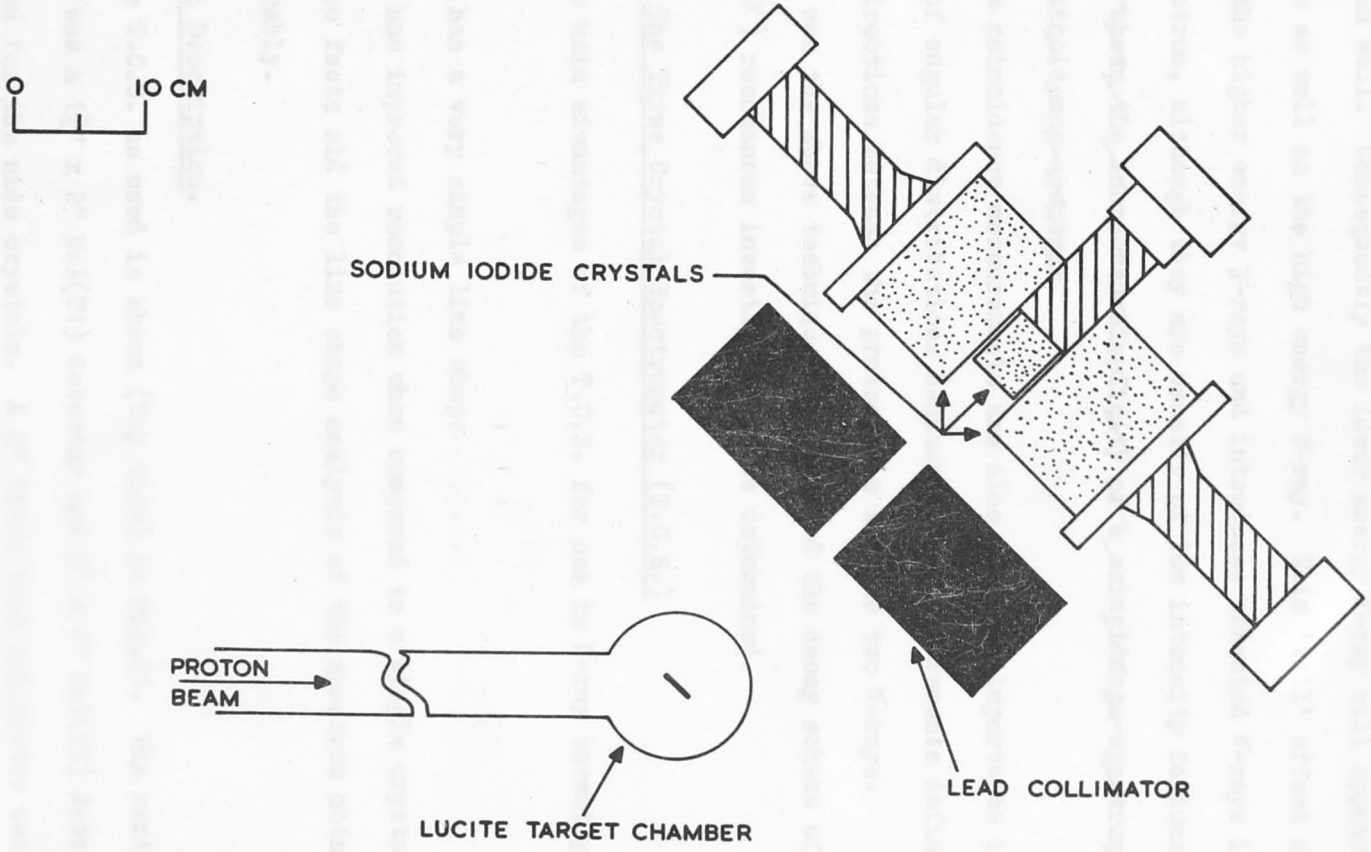
0
10 CM
SODIUM IODIDE CRYSTALS
PROTON
BEAM
LUCITE TARGET CHAMBER
LEAD COLLIMATOR

FIG. 21.

energy γ-ray line shape will fall within the single channel energy window as well. Consequently the lower energy γ-ray will appear in the spectrum as well as the high energy γ-ray. This 'tail' effect applies to all the higher energy γ-rays and introduces unwanted γ-rays into the spectrum, although they are usually of low intensity fortunately. ~~Fig. 20 shows the increased simplicity of a coincidence spectrum over a non-coincidence spectrum.~~

The coincidence measurements are alas of great importance in the theory of angular distributions because these measurements define the three directions between the proton beam and the two γ-rays.

It was the above technique that enabled the decay scheme of the $Mg^{26}(p,\gamma)$ resonances investigated to be determined.

2.3 The Three Crystal Spectrometer (T.C.S.)

The main advantages of the T.C.S. for use in γ-ray investigations are

(i) It has a very simple line shape

(ii) It has improved resolution when compared to a single crystal.

These two facts aid the line shape analysis of the spectrum obtained considerably.

Physical Description.

The T.C.S. as used is shown (Top view) in Fig.21. The centre crystal was a $1\frac{3}{4}$" x 2" NaI(T1) detector and 5" x 4" NaI(T1) detectors were used for the side crystals. A 4" thick lead collimator was used to present the direct γ-ray flux from entering the side crystals. The

FIG.22. The mechanism of the Three Crystal Spectrometer. (The relative counting rates in the three diagrams are unrelated).

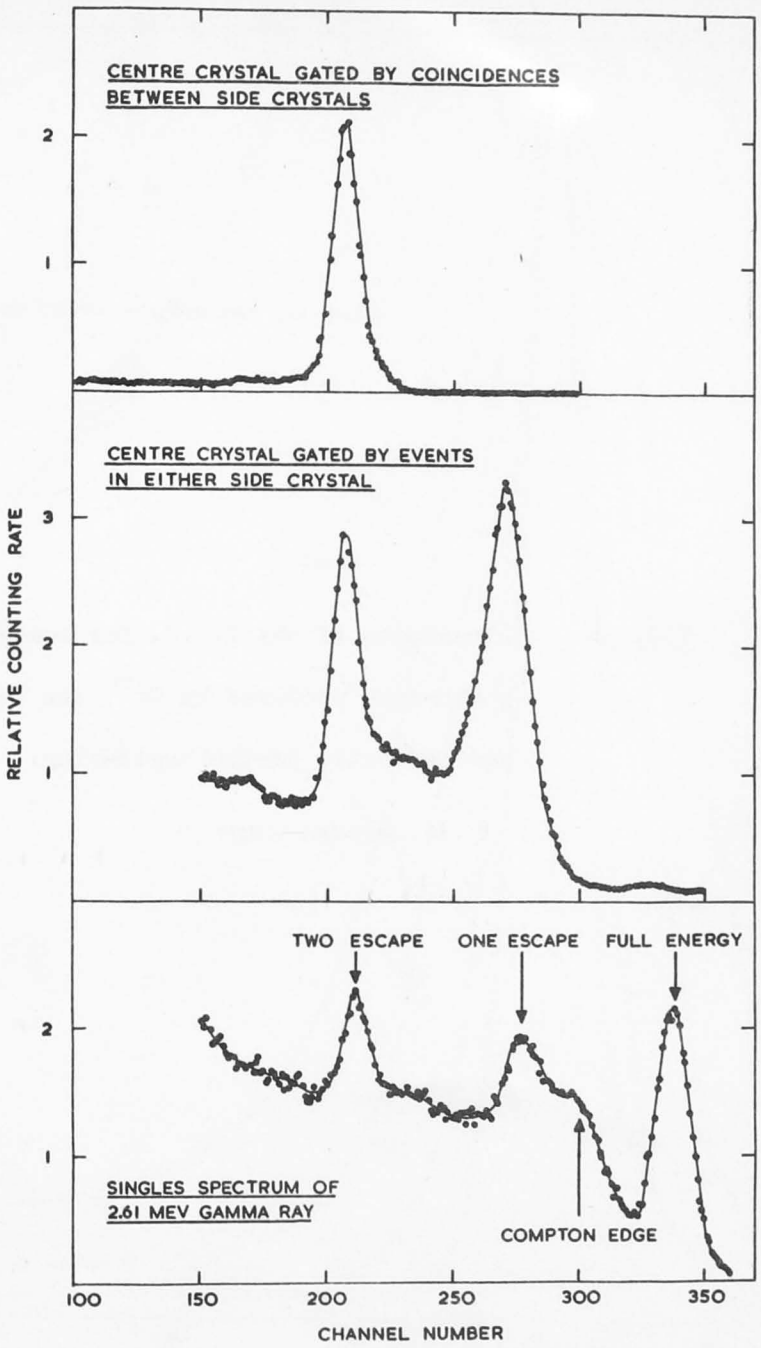
CENTRE CRYSTAL GATED BY COINCIDENCES BETWEEN SIDE CRYSTALS
CENTRE CRYSTAL GATED BY EVENTS IN EITHER SIDE CRYSTAL
TWO ESCAPE
ONE ESCAPE
FULL ENERGY
SINGLES SPECTRUM OF 2.61 MEV GAMMA RAY
COMPTON EDGE
RELATIVE COUNTING RATE
CHANNEL NUMBER
100
150
200
250
300
350

FIG. 22.

FIG.23. Lineshapes of the T.C.S. for mono-energetic gamma-rays produced by Co^{60} and ThC^{11} sources and inelastic proton scattering.

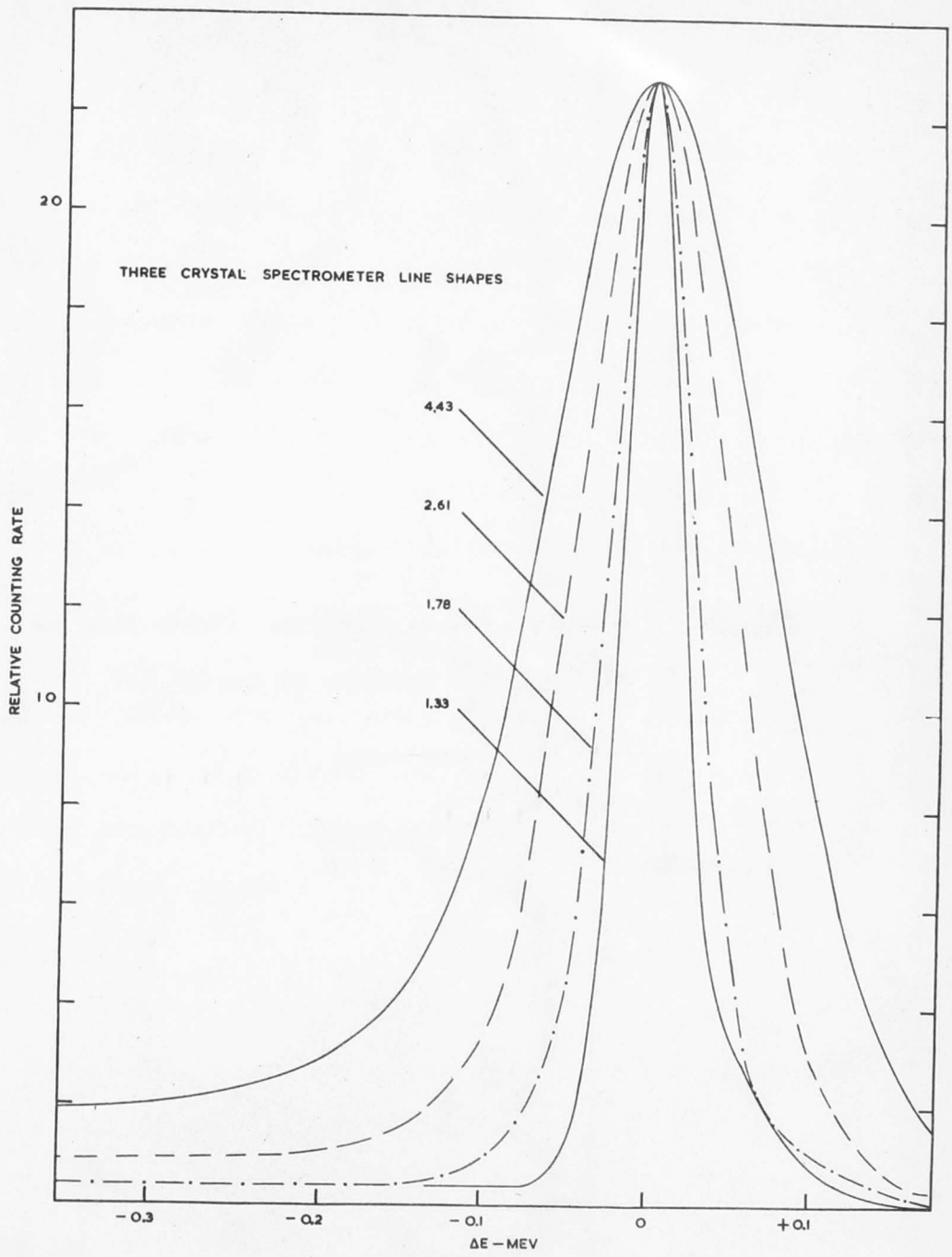
THREE CRYSTAL SPECTROMETER LINE SHAPES
RELATIVE COUNTING RATE
20
10
4.43
2.61
1.78
1.33
-0.3
-0.2
-0.1
0
+0.1
ΔE — MEV

FIG. 23.

FIG.24. A typical T.C.S. spectrum. (Taken from the $Al^{27}(p,\gamma)Si^{28}$ reaction at the 991 KeV resonance.)

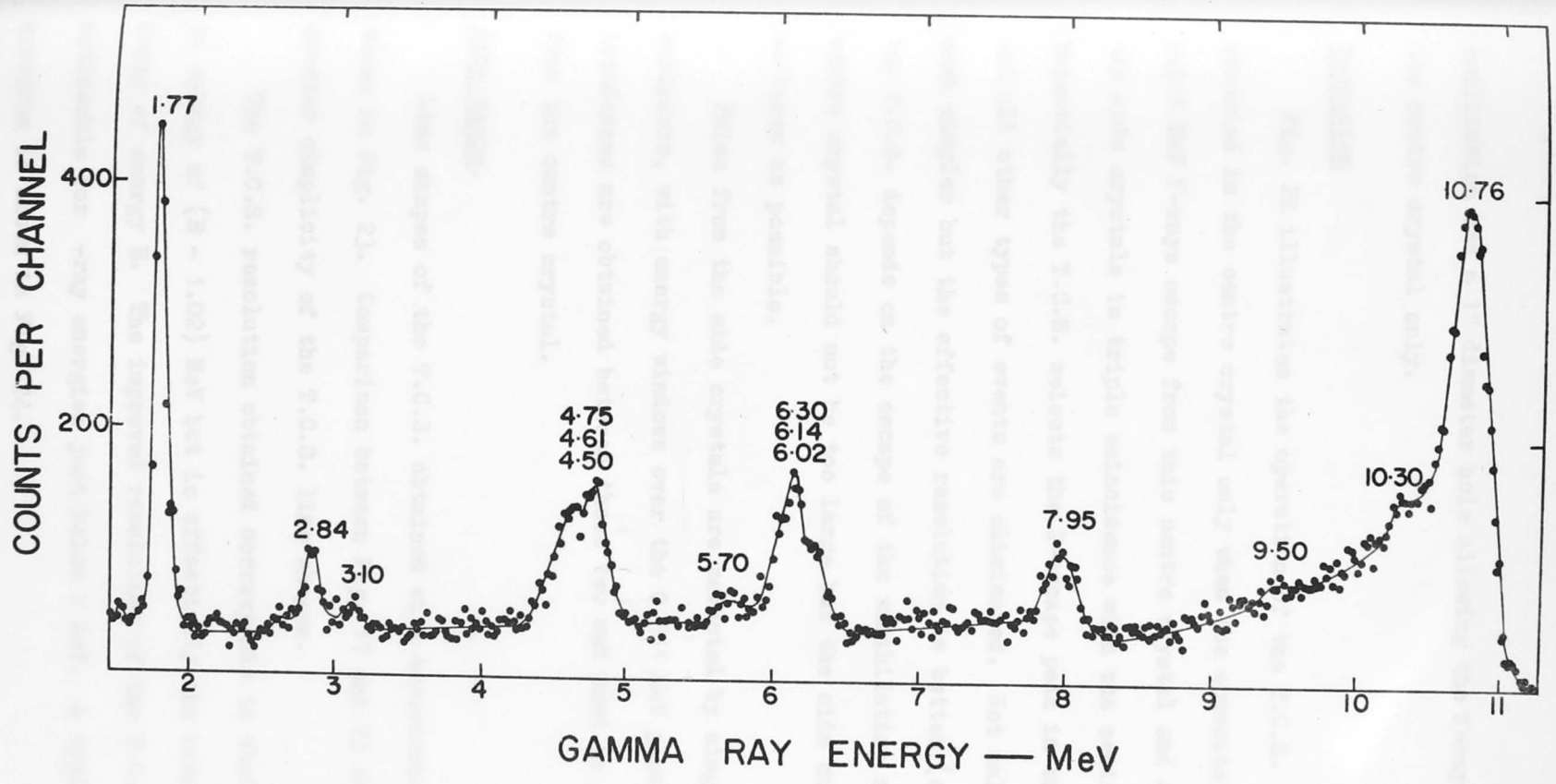
COUNTS PER CHANNEL
400
200
1·77
2·84
3·10
4·75
4·61
4·50
5·70
6·30
6·14
6·02
7·95
9·50
10·30
10·76
2
3
4
5
6
7
8
9
10
11
GAMMA RAY ENERGY — MeV

FIGURE 14

collimation had a 1" diameter hole allowing the γ-ray to impinge on the centre crystal only.

Mechanism

Fig. 22 illustrates the operation of the T.C.S. Events are recorded in the centre crystal only when the oppositely-directed 0.511 MeV γ-rays escape from this centre crystal and are recorded in the side crystals in triple coincidence with the centre crystal. Essentially the T.C.S. selects the 2-escape peak in the centre crystal and all other types of events are eliminated. Not only is the spectrum much simpler but the effective resolution is better (see later). Since the T.C.S. depends on the escape of the annihilation radiation the centre crystal should not be too large but the side crystals may be as large as possible.

Pulse from the side crystals are selected by single channel analysers, with energy windows over the 0.511 MeV photo-peaks. Coincidences are obtained between these two and used to gate the spectrum from the centre crystal.

Line shape.

Line shapes of the T.C.S. obtained with monochromatic γ-rays are shown in Fig. 23. Comparison between Fig. 17 and 23 shows the much greater simplicity of the T.C.S. line shapes.

The T.C.S. resolution obtained corresponds to that possible for an energy of (E - 1.02) MeV but is effectively the resolution for a γ-ray of energy E. The improved resolution of the T.C.S. is especially noticeable for -ray energies just below 2 MeV. A typical T.C.S. spectrum is shown in Fig. 24.

FIG.25. The relative detection efficiency of the T.C.S.

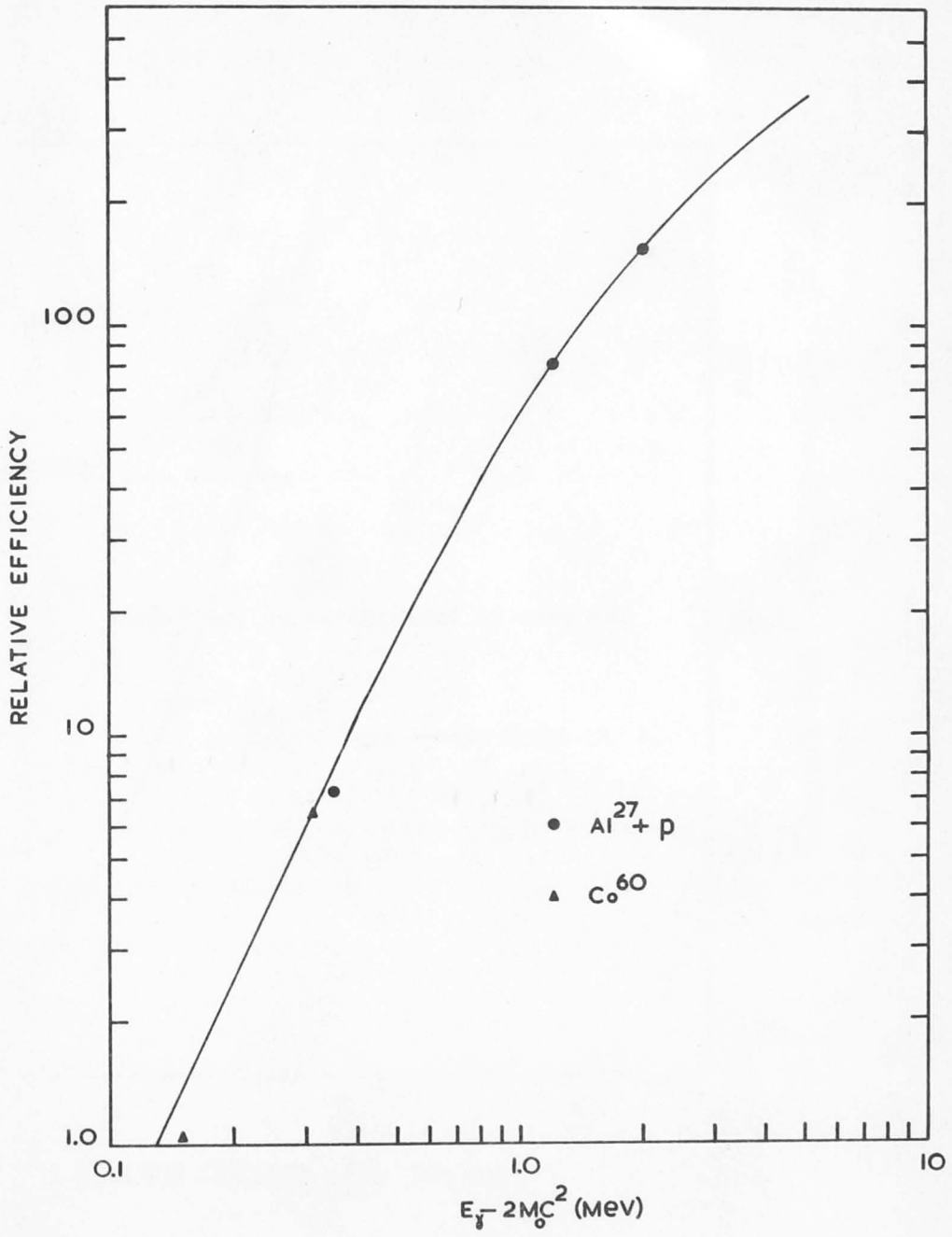
RELATIVE EFFICIENCY
100
10
1.0
0.1
1.0
10
$E_\gamma - 2M_oC^2$ (MeV)
$Al^{27} + p$
Co^{60}

FIG. 25.

FIG.26. The peak to total ratio of the T.C.S.

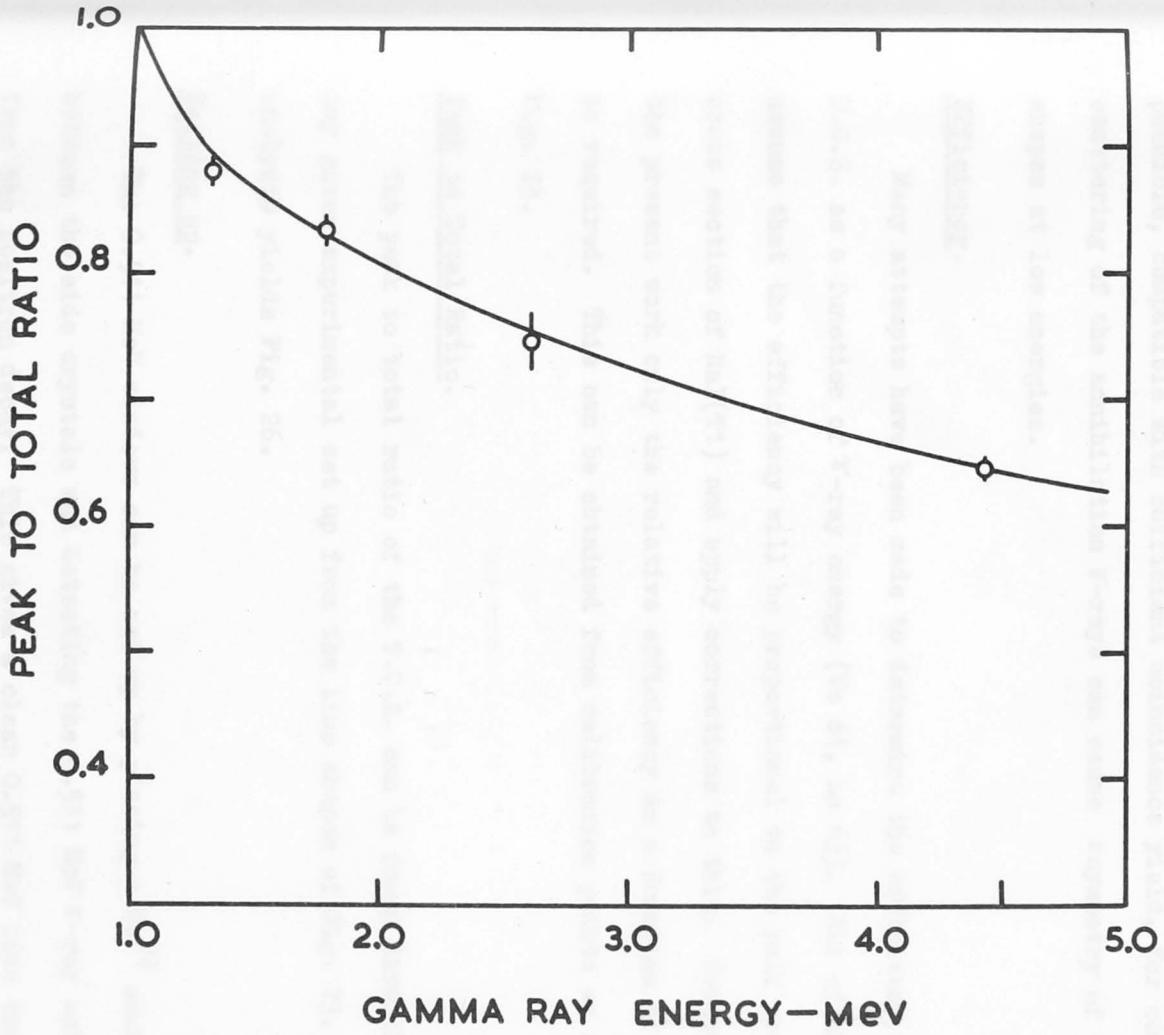
1.0
0.8
0.6
0.4
PEAK TO TOTAL RATIO
1.0
2.0
3.0
4.0
5.0
GAMMA RAY ENERGY—MeV

FIG. 26.

With the simpler line shape and improved resolution the analysis of T.C.S. spectra is much easier than single crystal spectra.

It is necessary to have the 0.511 MeV energy windows as narrow as possible, compatible with sufficient coincidence yield, for compton scattering of the annihilation γ-rays can cause asymmetry of the line shapes at low energies.

Efficiency.

Many attempts have been made to determine the efficiency of the T.C.S. as a function of γ-ray energy (Va 61, La 63). All of these assume that the efficiency will be proportional to the pair production cross section of NaI(T1) and apply corrections to this. However, in the present work only the relative efficiency as a function of energy is required. This can be obtained from calibration points as shown in Fig. 25.

Peak to Total Ratio.

The peak to total ratio of the T.C.S. can be found directly for any given experimental set up from the line shapes of Fig. 23. Such analysis yields Fig. 26.

Setting up.

The 0.511 MeV windows can be set up by placing a Na^{22} source between the side crystals and detecting the 0.511 MeV γ-ray emitted from the positron decay. This gives a clear 0.511 MeV line that permits accurate setting of the energy windows.

Disadvantages of the T.C.S.

One of the main disadvantages of the T.C.S. is its low efficiency.

FIG.27. A spectrum taken with a solid state gamma-ray detector of the ThC^{11} 2.61 MeV gamma-ray. The arrow shows the expected position of the first escape peak.

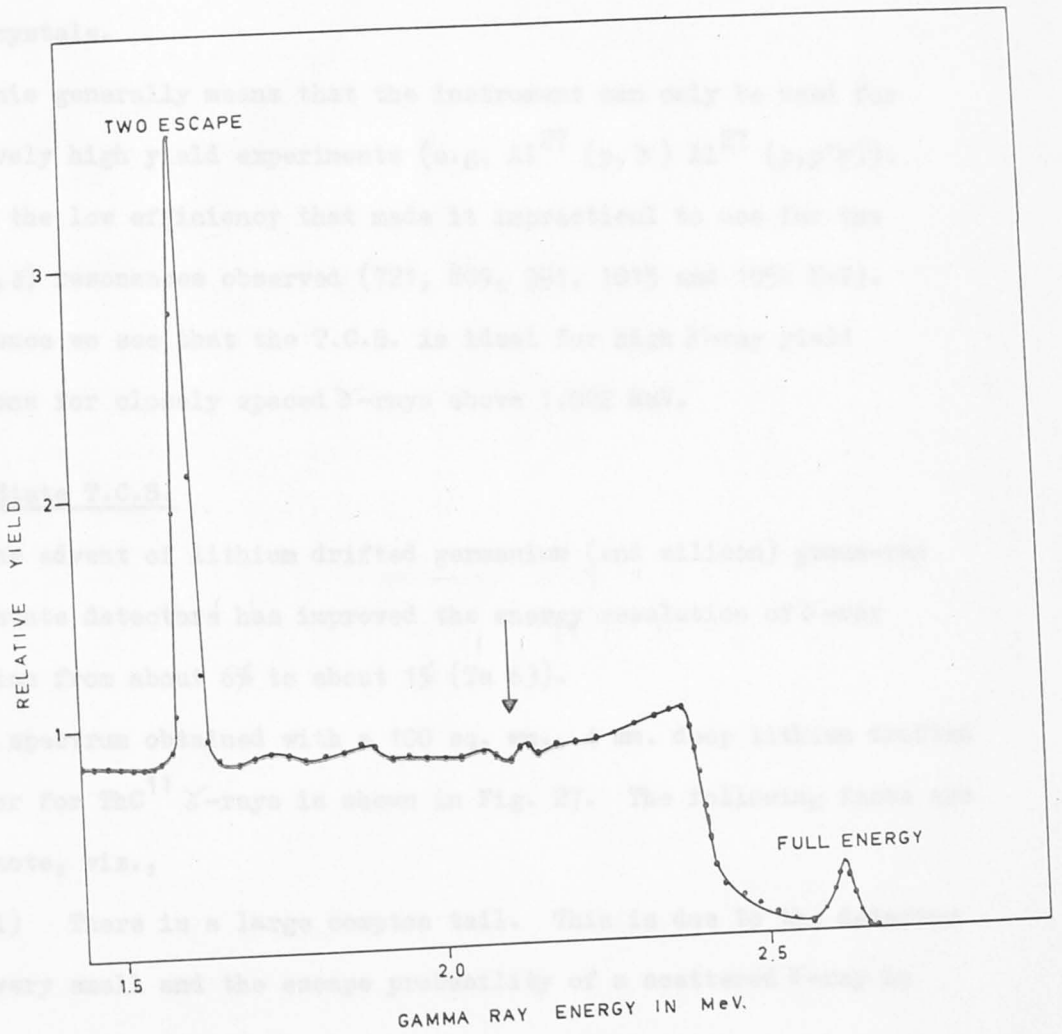
TWO ESCAPE
FULL ENERGY
RELATIVE YIELD
3
2
1
1.5
2.0
2.5
GAMMA RAY ENERGY IN MeV.

FIG. 27.

This is due to the fact that it is a coincidence arrangement between three crystals and hence depends on the product of three crystal detection efficiencies.

(i) The pair production efficiency of the central crystal

(ii) and (iii) The 0.511 MeV detection efficiency of the two side crystals.

This generally means that the instrument can only be used for relatively high yield experiments (e.g. Al^{27} (p,γ) Al^{27} (p,p'γ)). It was the low efficiency that made it impractical to use for the Mg^{26}(p,γ) resonances observed (721, 809, 991, 1015 and 1056 KeV).

Hence we see that the T.C.S. is ideal for high γ-ray yield reactions for closely spaced γ-rays above 1.022 MeV.

2.4 Solid State T.C.S.

The advent of lithium drifted germanium (and silicon) gamma-ray solid state detectors has improved the energy resolution of γ-ray detection from about 6% to about 1% (Ta 63).

A spectrum obtained with a 100 sq. mm., 4 mm. deep lithium drifted detector for ThC^{11} γ-rays is shown in Fig. 27. The following facts are worth note, viz.,

(i) There is a large compton tail. This is due to the detector being very small and the escape probability of a scattered γ-ray is high.

(ii) There is no first escape peak. This means that the full energy peak is due entirely to the photo-electric process.

FIG.28. A spectrum taken with a solid state detector as the central crystal of a T.C.S. A comparison of Figs.28 and 23 will show the increased resolution of the solid state detector.

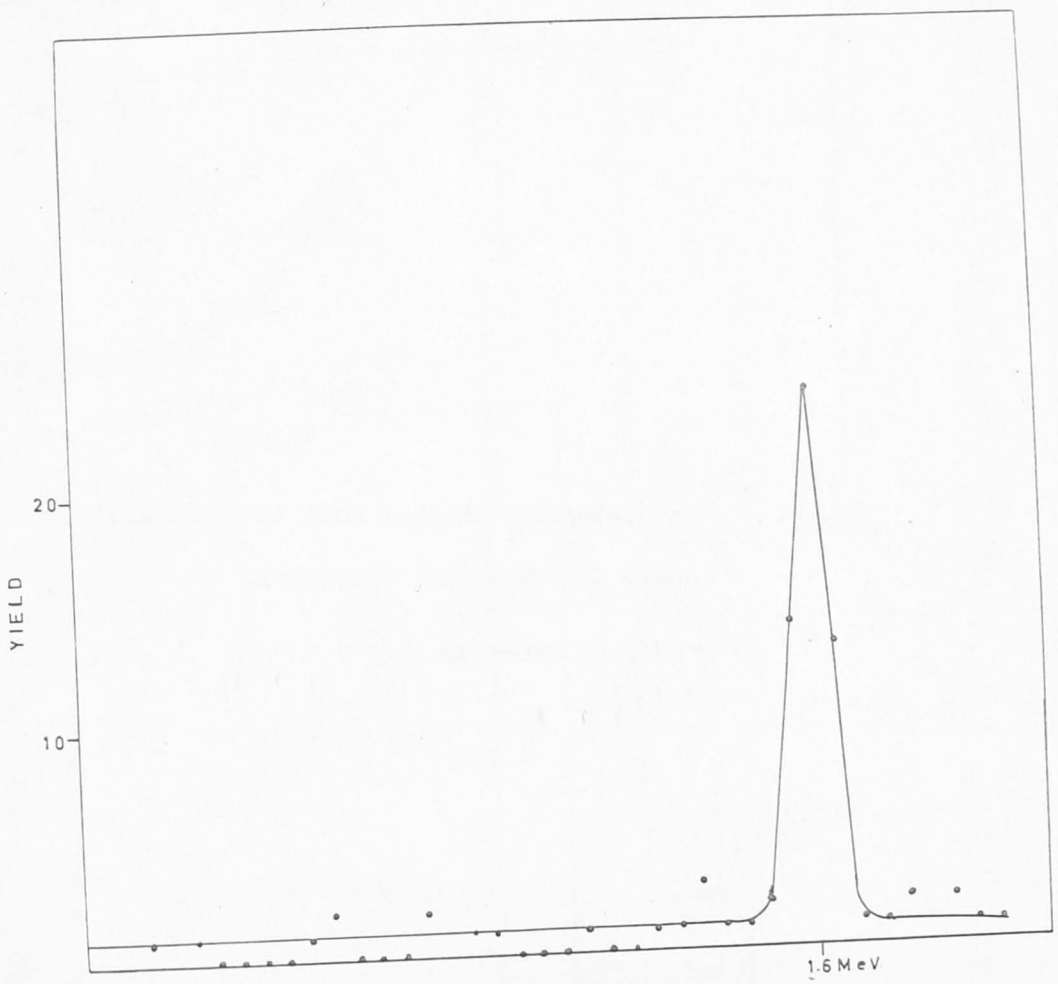

FIG. 28.

FIG.29. The detection chamber used with the solid state detector (not to scale).

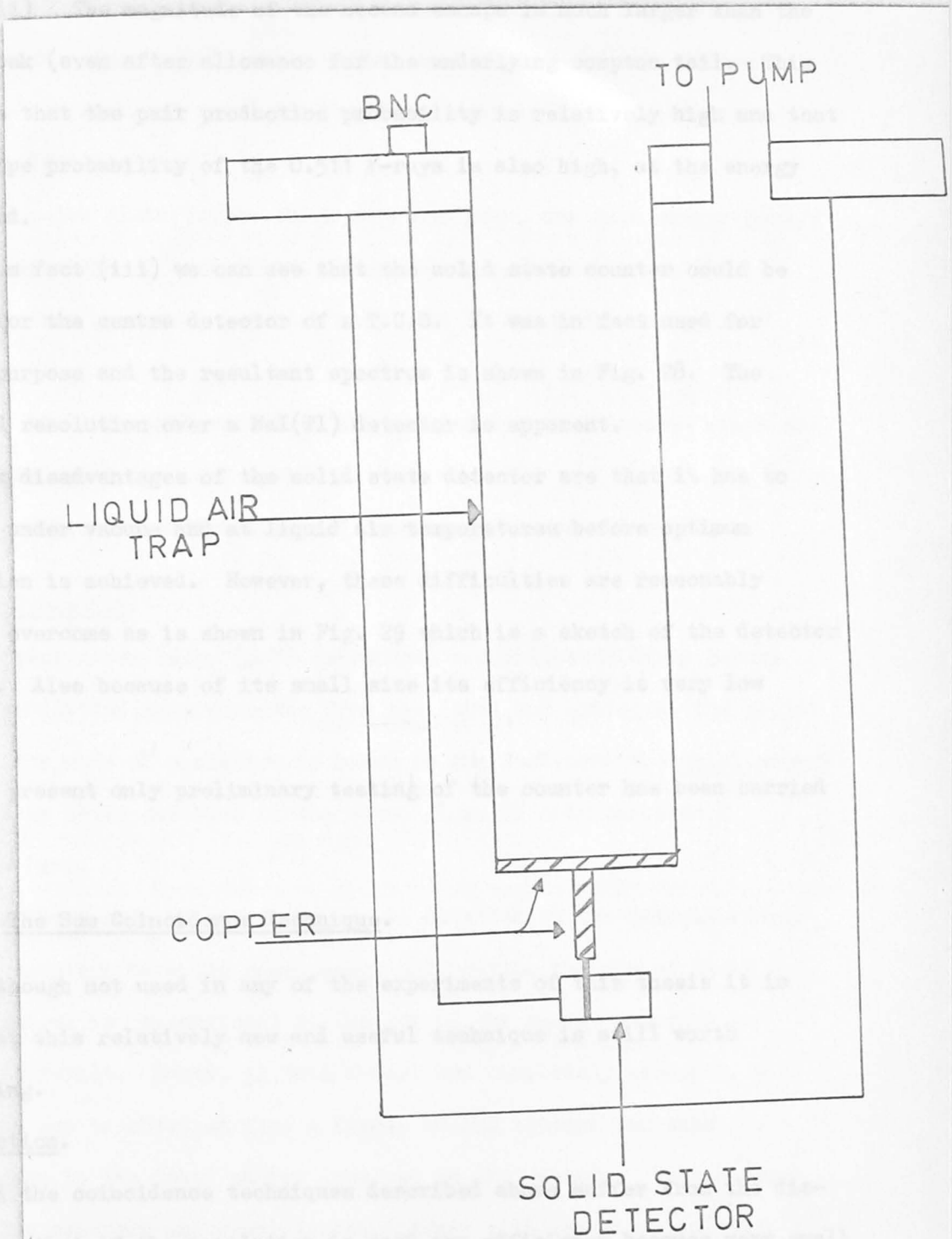
TO PUMP
BNC
LIQUID AIR
TRAP
COPPER
SOLID STATE
DETECTOR

(iii) The magnitude of the second escape is much larger than the photo-peak (even after allowance for the underlying compton tail. This suggests that the pair production probability is relatively high and that the escape probability of the 0.511 γ-rays is also high, at the energy indicated.

From fact (iii) we can see that the solid state counter could be useful for the centre detector of a T.C.S. It was in fact used for such a purpose and the resultant spectrum is shown in Fig. 28. The improved resolution over a NaI(Tl) detector is apparent.

The disadvantages of the solid state detector are that it has to be used under vacuum and at liquid air temperatures before optimum resolution is achieved. However, these difficulties are reasonably easy to overcome as is shown in Fig. 29 which is a sketch of the detector chamber. Also because of its small size its efficiency is very low indeed.

At present only preliminary testing of the counter has been carried out.

2.5 The Sum Coincidence Technique.

Although not used in any of the experiments of this thesis it is felt that this relatively new and useful technique is still worth describing.

Introduction.

All the coincidence techniques described above suffer from the disadvantage that if the resolution is good the efficiency becomes very small and vice versa. This is especially serious if the γ-ray spectrum contains

a number of coincident lines. Here I shall describe a coincidence spectrometer that is especially suited to measure γ-γ coincidence spectra. It has good resolution and a relatively high efficiency. The main features are:

(a) The pulse distribution shows only one peak, the full energy peak, for one specific γ transition. There is no contribution to the spectrum from processes in which only part of the γ-ray energy is absorbed.

(b) The absolute half-widths of the peaks due to coincident γ-rays are, to a first approximation, equal.

(c) The detection efficiencies of coincident γ-rays are equal.

Mode of Operation.

In many cases (e.g. (p,γ) reactions) a complicated decay scheme can be subdivided into cascades from one level and ending at the ground state. The mode of operation is based on the fact that the total energy involved in these cascades is the same. I shall only consider 2 cascades here.

The two γ-rays of a cascade can be detected by two scintillators. If both counters have the same energy calibration the sum of their output pulses is proportional to the sum of the energy absorbed in the two crystals. Hence, if both γ-rays are completely absorbed, a sum pulse can be obtained from a linear adding network and this corresponds to the total energy involved in the cascade. Pulses from one of the counters which are in coincidence with these sum pulses all belong to processes of full-energy absorption of one or both γ-rays

in this crystal. Thus this coincidence spectrum shows only the full-energy peaks of the γ-rays. In practice this "sum-coincidence" spectrum is obtained by gating a multi-channel analyser.

Resolution.

The optimum resolution is obtained when the sum channel is very narrow. Then the two γ-rays in the coincidence spectrum have the same width. Both peaks will be narrower than the narrowest of the two peaks in the single crystal spectrum. (This gives a great improvement for high energy γ-rays)

e.g. If a 1 MeV and a 6 MeV -ray are detected by this method, both having 6% full energy peaks in the singles spectrum, the resolution of the high energy peak will be 1%. If the γ-rays are of comparable energy the improvement will be about 2.

Efficiency.

The detection efficiency in the sum coincidence technique does not depend on γ-ray energy very strongly.

In every sum-coincidence spectrum a sum peak appears corresponding to the sum energy chosen. This arises from

(i) The full-energy peak of the cross over transition.

(ii) Events in which both γ-rays of the cascade add in one crystal.

(iii) Background.

Line Shape.

The line shapes of the γ-rays detected are almost solely gaussian peaks with a very small tail indeed, the tail being flat.

For high count rates it will also be necessary to obtain coincidences between the sum pulses and the coincident pulses from the cathode follower outputs of the detectors, before gating the singles spectrum.

It is worth note that when the coincidence spectrum is measured with one counter fixed and the other varied in angle the triple correlation of the γ-rays is measured in two different geometries at once.

* * * * * * *

CHAPTER III

The Helium-3 Reactions

From the point of view of studying reaction mechanisms He^3 induced reactions are particularly interesting. In recent years, with the advent of comparative availability and reasonable price, He^3 induced reactions have received much attention. (Br 56, Ku 64, Di 64). The compound nucleus and direct interaction may both be expected to play substantial roles. Since the success of Butler's stripping theory (Bu 57) of (d,p) and (d,n) reactions, the same general ideas have been applied to reactions produced by He^3. On the other hand a number of reactions which might be expected to proceed via stripping have shown compound nucleus formation.

Most of the reactions induced by He^3 are characterised by high Q-values, and therefore the compound systems are highly excited. It is possible in He^3 induced reactions to explore regions of excitation energy which would be inaccessible with protons and deuterons using the same accelerator.

The high charge to mass ratio of He^3 permits the study of the proton rich member of an isobaric multiplet by means of the (He^3,n) reaction. Also comparison of (He^3,n) and (He^3,p) reactions may give information regarding the charge independance of nuclear forces without complication from different reaction mechanisms.

3.1 The $B^{10}(He^3,t)C^{10}$ Reaction.

Introduction.

Before this experiment was carried out only one other (He^3,t) reaction had been reported in the literature. This was the $Be^9(He^3,t)B^9$ - 1.088 MeV reaction and it was observed with a differential cross section $\frac{d\sigma}{d\Omega} \sim 1$ m b at 0° at 25 MeV bombarding energy (We 60, Hi 59). A recent study at the A.N.U. of the $B^{10}(p,n)C^{10}$ reaction (Ea 63) suggested that an investigation of the $B^{10}(He^3,t)C^{10}$ - 3.629 MeV reaction may be of some interest. As in the (p,n) case the $\Delta J = 3$ difference between ground states with ingoing and outgoing spin $\frac{1}{2}$ particles is expected to inhibit the reaction at low energies. However, it is expected that the cross sections for the (He^3,t) case will be smaller than those of the (p,n) reaction since the bombarding and emitted particles have charges two and one respectively instead of one and zero. Hence the coulomb barrier will be greater.

The N^{13} nucleus.

In the $B^{10}(He^3,t)C^{10}$ reaction the compound nucleus, if any is formed, is the N^{13} nucleus. The excitation in this nucleus would be 25.27 MeV and upwards. Information on this energy region of N^{13} is very scarce. The $B^{10}(He^3,p)C^{12}$ reaction has been studied (Aj 62) and shown to exhibit compound nucleus like resonances at 23.2, 24.5, 24.8 and 25.2 MeV. However, as will be seen later the (He^3,t) reaction does not form a compound nucleus, which prohibits obtaining the information required on the N^{13} nucleus.

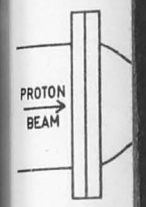

FIG.30 The activation apparatus, showing the tantulum lining and distribution of shielding materials for the NaI(Tl) detectors.

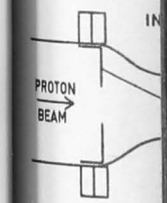

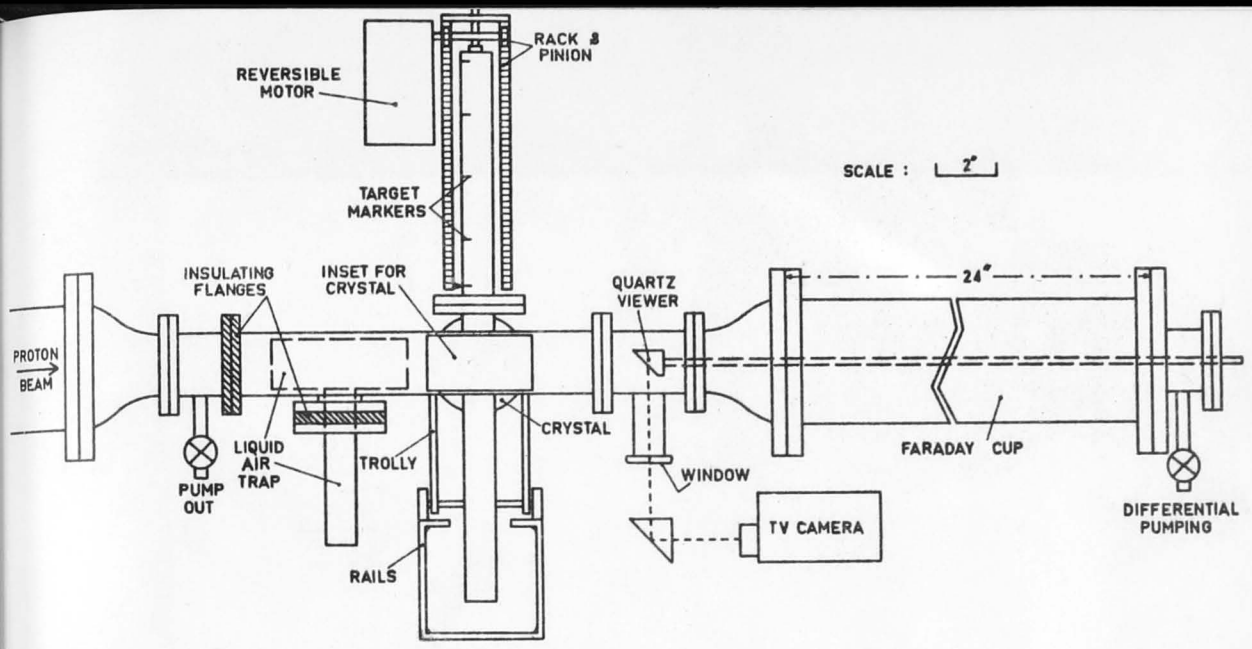
REVERSIBLE MOTOR
RACK & PINION
SCALE : 2"
TARGET MARKERS
INSULATING FLANGES
INSET FOR CRYSTAL
QUARTZ VIEWER
24"
PROTON BEAM
CRYSTAL
LIQUID AIR TRAP
TROLLY
PUMP OUT
WINDOW
FARADAY CUP
TV CAMERA
DIFFERENTIAL PUMPING
RAILS

(a)

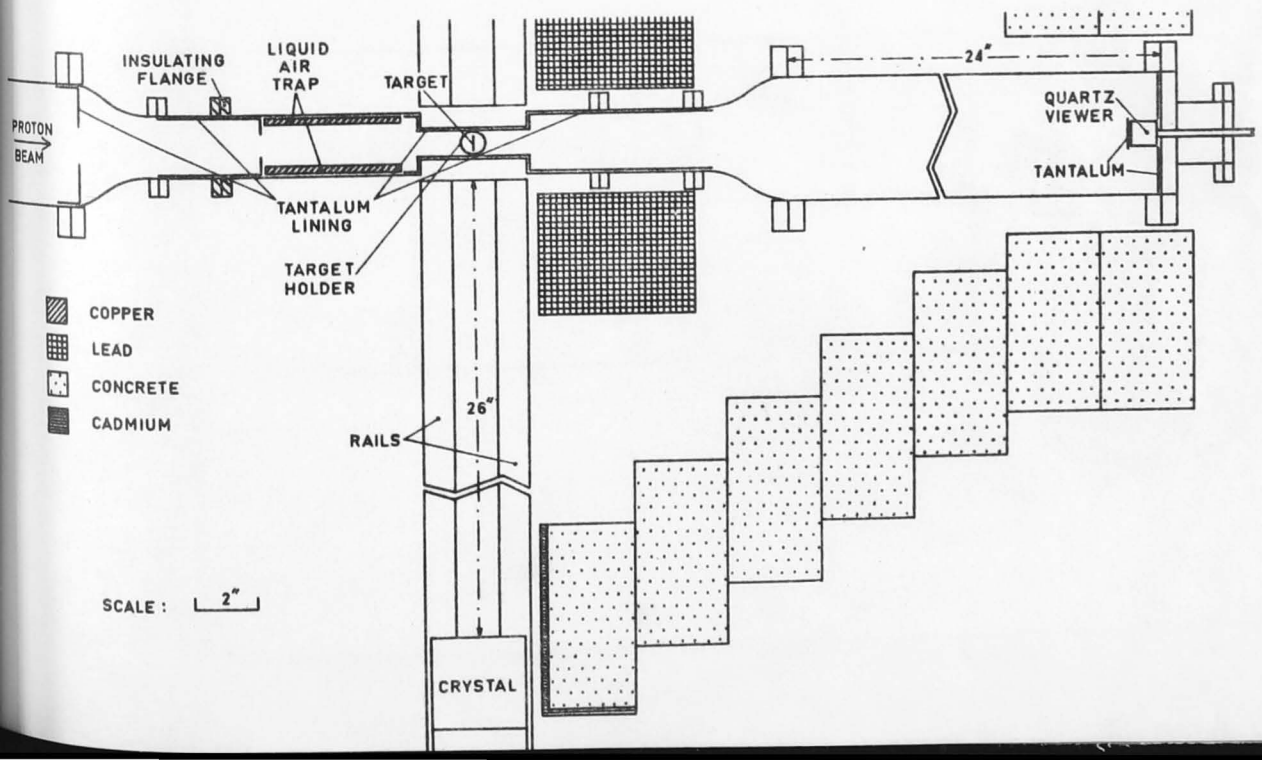
INSULATING FLANGE
LIQUID AIR TRAP
TARGET
24"
QUARTZ VIEWER
PROTON BEAM
TANTALUM
TANTALUM LINING
TARGET HOLDER
COPPER
LEAD
CONCRETE
CADMIUM
26"
RAILS
SCALE : 2"
CRYSTAL

FIG. 3·2 The positron decay scheme of C^{10}.

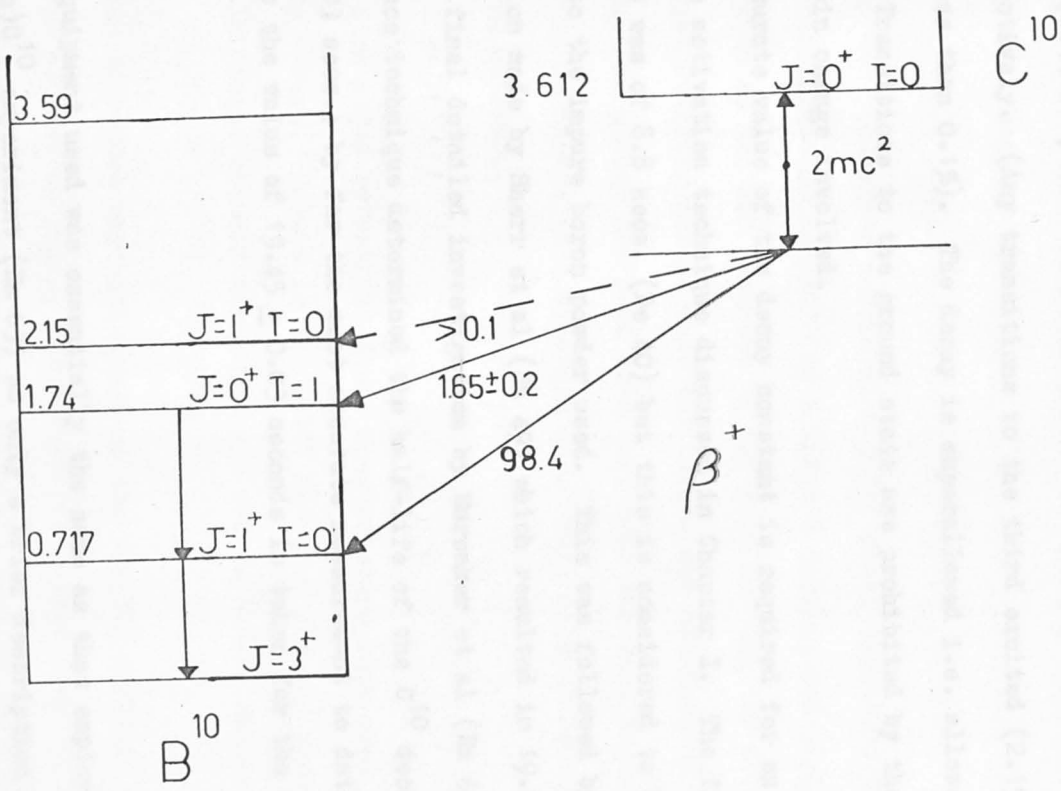
3.612
J=0+ T=0
C10
2mc2
3.59
2.15
J=1+ T=0
>0.1
1.74
J=0+ T=1
1.65±0.2
98.4
β+
0.717
J=1+ T=0
J=3+
B10

FIG. 3-2.

The C^{10} decay.

The $B^{10}(He^3,t)C^{10}$ reaction can be readily investigated using the activation technique described in Chapter I since the positron decay of C^{10} (see Fig. 3·2) is by positron emission to the first (0.717 MeV) and second (1.74 MeV) excited states of B^{10} in 98.4% and 1.74% probability respectively. (Any transitions to the third excited (2.15 MeV) state is less than 0.1%). The decay is superallowed i.e. allowed and favoured. Transitions to the ground state are prohibited by the three units of spin change involved.

An accurate value of the decay constant is required for an application of the activation technique discussed in Chapter I. The first measurement was of 8.8 secs. (De 40) but this is considered to be in error due to the impure boron powder used. This was followed by the determination made by Sherr et al (Sh 49) which resulted in 19.1 ± 0.8 secs. The final detailed investigation by Earwaker et al (Ea 62) using a coincidence technique determined the half-life of the C^{10} decay as 19.45 ± 0.03 secs.; by far the most accurate measurement to date. In this thesis the value of 19.45 ± 0.03 seconds is taken for the C^{10} decay.

Apparatus.

The equipment used was essentially the same as that employed in the $B^{10}(p,n)C^{10}$ experiment (Ea 63) so only a brief description will be given here with reference to Fig. 30.

The reaction chamber body was made of brass, completely lined with 0.02 cm. tantulum to prevent activation of the brass walls. In

order to increase the detection efficiency, two flat sections were inset into the side of the chamber. A tantulum cylinder capable of moving vertically inside two sleeves provided mounting positions for four targets. A remotely controlled motor was used to drive the target support and position the target to better than 0.05 cm. A retractable quartz disc was used to align the beam on the target.

Targets.

For all He^{3++} energies a separated boron metal target, 99.9% B^{10}, of nominal thickness 200 μgm/cm^2 on a thick W backing was employed. The energy loss of the He^3 beam was 80 KeV at 9 MeV and 110 KeV at 6 MeV. Target scanning showed that the target was non-uniform by as much as 30%. The quartz was used to ensure that the same region of the target was bombarded each time (Ea 63). This allowed reproducible results to be obtained.

Detectors.

Two 7.6 cm x 7.6 cm NaI(Tl) γ-ray spectrometers were used to detect the C^{10} decay γ-rays. Pulses in the 0.717 MeV (see Fig. 2) photo-peaks were selected with single channel analysers and fed to A.N.U. scalers for counting.

In order to reduce any activation of the NaI(Tl) crystals the counters were mounted on small, compressed air driven trolleys which were withdrawn to 66 cms. from the target during the bombardment period, and brought to within 2 cms. of the target for the counting period.

Because of gain variations in the photo-multipliers caused by the high counting rates when the beam was on the target the photo-

multipliers were shut off during the bombardment period by applying a reverse bias of -90V between the photo-cathode and the focus grid.

Experimental procedure.

As the reaction cross section was expected to be small, preliminary investigations were carried out at 10 MeV and, after bombardment, the presence of C^{10} formed on the target was sought by searching for the 0.717 MeV γ-ray line of half-life 19.45 secs. which follows β^+ transitions to both the 0.717 MeV and 1.74 MeV states of B^{10} that are populated with 98.4 and 1.6% probability respectively (see Fig. 3·2).

The experimental technique employed was essentially the same at that in (Ea 63). The target was irradiated for 60 secs. At time 60 secs. a switch simultaneously

(i) operated a plunger to intercept the beam

(ii) started an electronic timer

(iii) activated the compressed air cylinders to bring the crystals to the operating position.

At time 62 secs. the timer operated a relay switch which removed the 90V bias from the photo-multiplier tubes. Counts then terminated by re-applying the 90V bias. At time 180 secs. a 60 sec. background count was started.

The beam current was measured with an ELCOR A309A current integrator and was chosen so that counting losses were less than 1%.

The He^{3++} ions for the bombardment were obtained from the A.N.U. Tandem accelerator using the Helium injector and they produced considerable long live β^+ activities leading to a strong 0.511 MeV γ-ray line, mainly from the $B^{10}(He^3,)C^{11}$ reaction, but a clear 0.717 MeV

FIG.31. A gamma-ray spectrum taken with one of the 3" x 3" spectrometers after bombardment with He^{3++} ions of 10 MeV. The hatched area indicates the energy interval selected for the relative yield measurements.

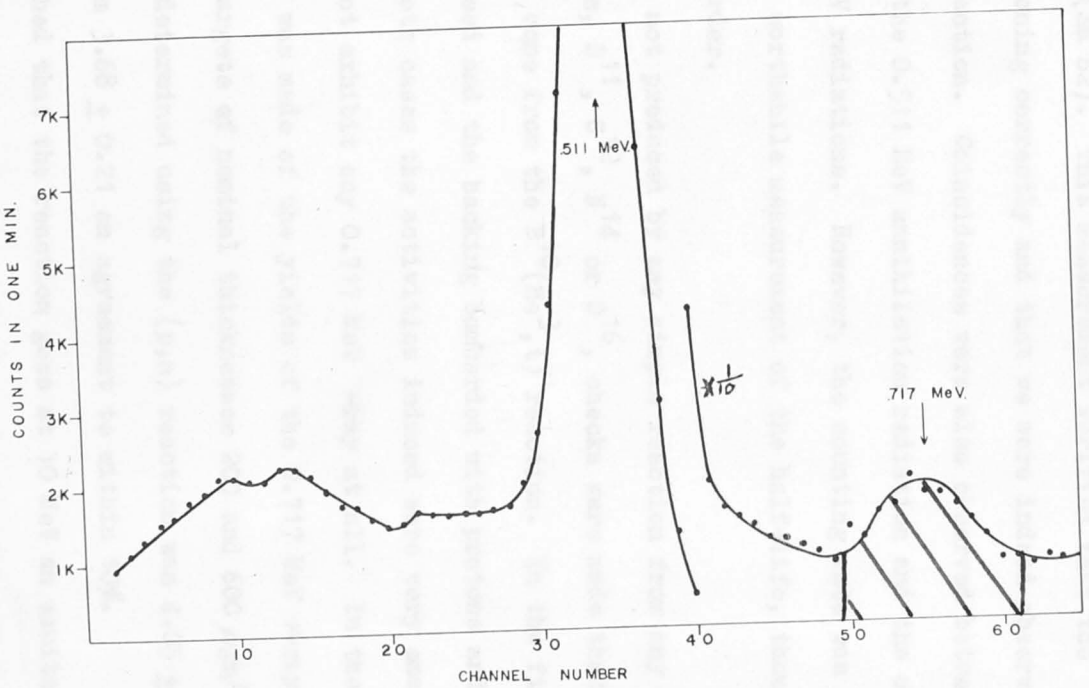

FIG 2. SPECTRUM FROM $B^{10}(He^3,t)C^{10}$ AT 9 MeV.

-ray line could be identified on the high energy side of this 0.511 MeV peak (see Fig. 31). An 80 KeV window was placed over the peak (shaded area in Fig. 31) and its decay was observed combining the data from a number of runs. A figure of (19 ± 1) secs. was obtained for the half-life (Computer fit) which compares well with (19.45 ± 0.03) secs. measured previously (Ea 62). This measurement verified that the apparatus was functioning correctly and that we were indeed observing the $B^{10}(He^3,t)C^{10}$ reaction. Coincidences were also observed between a crystal detecting the 0.511 MeV annihilation radiation and the other crystal the 0.717 MeV radiations. However, the counting rate was then too small to allow a worthwhile measurement of the half-life, though it was of the correct order.

Although C^{10} is not produced by any simple reaction from any of the expected contaminants, B^{11}, C^{12}, N^{14} or O^{16}, checks were made that the activity did in fact come from the $B^{10}(He^3,t)$ reaction. In the first, the target was reversed and the backing bombarded with protons and Helium-3 ions. In both cases the activities induced were very small, long lived and did not exhibit any 0.717 MeV -ray at all. In the second, a comparison was made of the yields of the 0.717 MeV γ-ray from two 99.9% B^{10} targets of nominal thicknesses 200 and 600 $\mu gm/cm^2$. The thickness ratio determined using the (p,n) reaction was 4.05 ± 0.22 and with the He^3 beam 3.68 ± 0.21 an agreement to within 10%.

Having established that the reaction goes at 10 MeV an excitation function was measured at 250 KeV intervals from threshold to 10.5 MeV by observing the 0.717 MeV yield as a function of He^3 energy. Three

FIG.32. The total cross section for the $B^{10}(He^3,t)C^{10}$ reaction as a function of He^3 energy from threshold to 10.5 MeV.

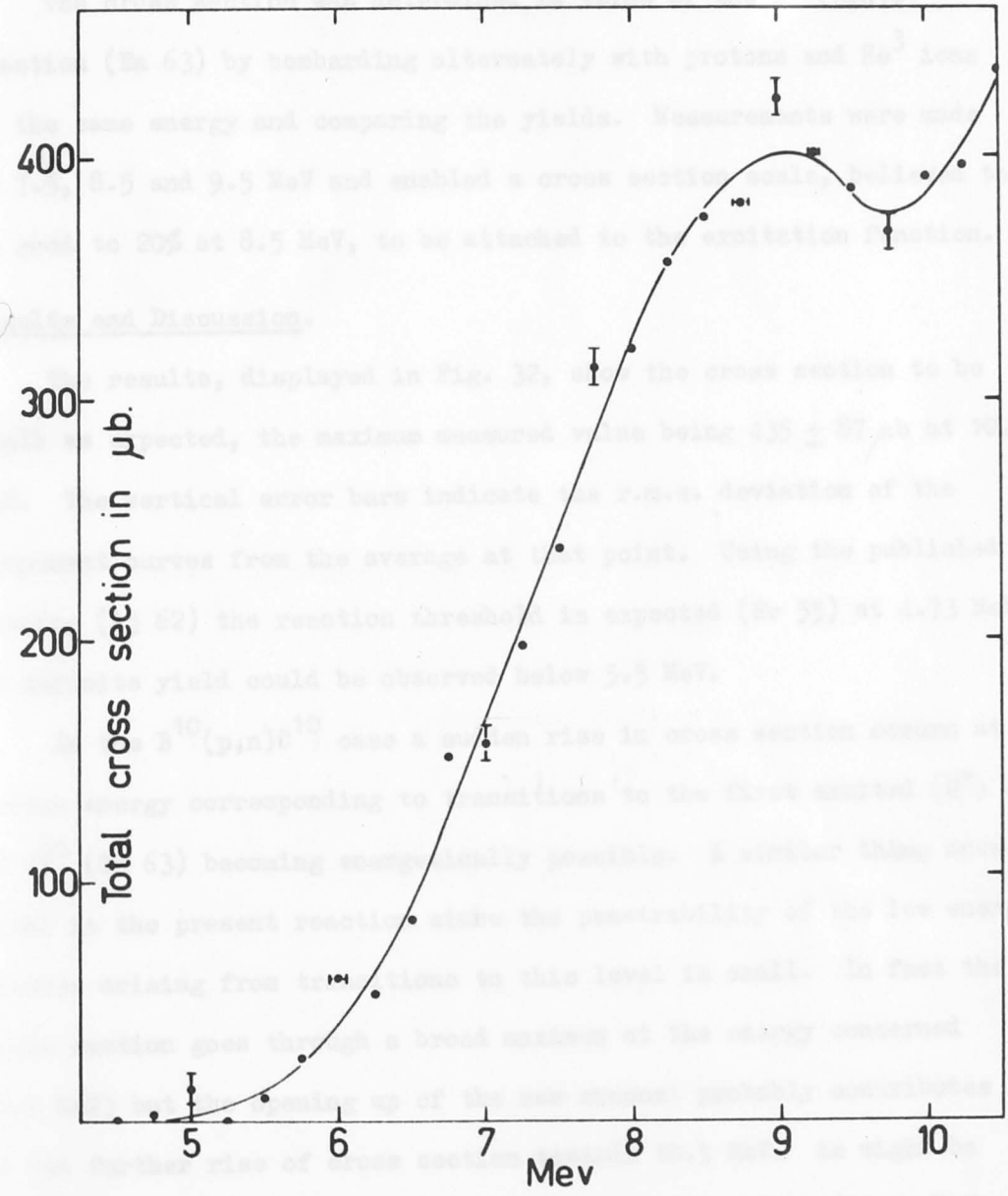

fig. 32.

runs were made at each energy and the entire energy range was covered twice.

The cross section was determined in terms of the $B^{10}(p,n)C^{10}$ reaction (Ea 63) by bombarding alternately with protons and He^3 ions at the same energy and comparing the yields. Measurements were made at 7.5, 8.5 and 9.5 MeV and enabled a cross section scale, believed to be good to 20% at 8.5 MeV, to be attached to the excitation function.

Results and Discussion.

The results, displayed in Fig. 32, show the cross section to be small as expected, the maximum measured value being 435 ± 87 μb at 10.5 MeV. The vertical error bars indicate the r.m.s. deviation of the component curves from the average at that point. Using the published Q-value (Aj 62) the reaction threshold is expected (Ev 55) at 4.73 MeV. No definite yield could be observed below 5.5 MeV.

In the $B^{10}(p,n)C^{10}$ case a sudden rise in cross section occurs at a proton energy corresponding to transitions to the first excited (2^+) state of C^{10} (Ea 63) becoming energetically possible. A similar thing does not occur in the present reaction since the penetrability of the low energy tritons arising from transitions to this level is small. In fact the cross section goes through a broad maximum at the energy concerned (9.1 MeV) but the opening up of the new channel probably contributes to the further rise of cross section towards 10.5 MeV. As might be expected from the high excitation of the compound system (25.27 MeV upwards) and the energy resolution achieved (section 3.1.4) no detailed structure is apparent in the excitation function.

FIG. 3·3 The O^{15} nucleus in the region of interest for the $C^{12}(He^3,n)O^{14}$ reaction.

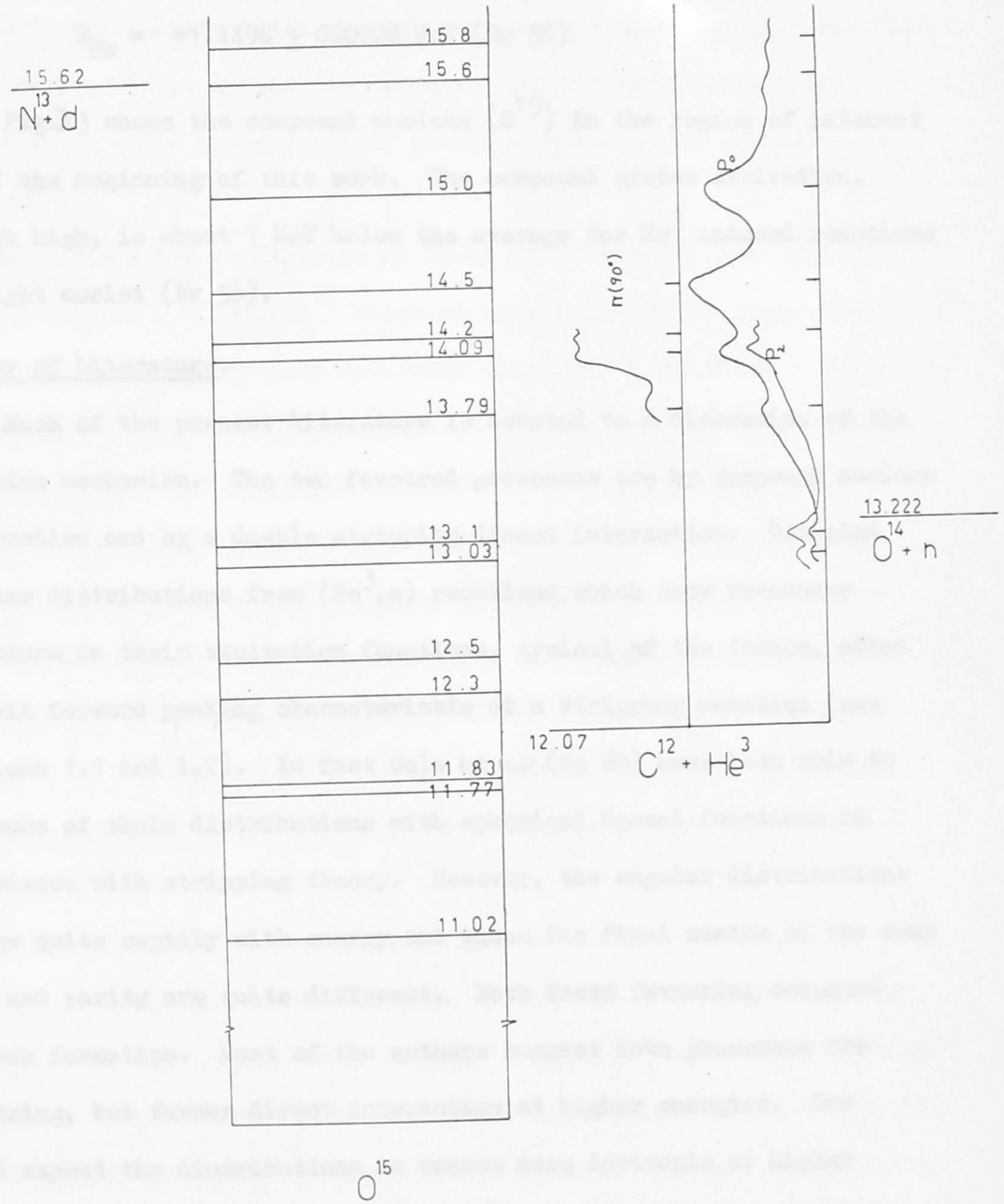
15.62
$N^{13} + d$
15.8
15.6
15.0
14.5
14.2
14.09
13.79
13.1
13.03
12.5
12.3
11.83
11.77
11.02
O^{15}
n(90°)
p_0
p_2
13.222
$O^{14} + n$
12.07
$C^{12} + He^3$

FIG. 3·3

3.2. The $C^{12}(He^3,n)O^{14}$ Reaction.

$Q = -1.167$ MeV

$E_{Th} = +1.4496 \pm 0.0028$ MeV (Br 56)

Fig.3.3 shows the compound nucleus (O^{15}) in the region of interest as of the beginning of this work. The compound system excitation, though high, is about 7 MeV below the average for He^3 induced reactions on light nuclei (Br 56).

Survey of Literature.

Much of the present literature is devoted to a discussion of the reaction mechanism. The two favoured processes are by compound nucleus interaction and by a double stripping direct interaction. Detailed angular distributions from (He^3,n) reactions which show resonance structure in their excitation functions, typical of the former, often exhibit forward peaking characteristic of a stripping reaction (see Sections 1.1 and 1.2). In fact Gale et al (Ga 60) have been able to fit some of their distributions with spherical Bessel functions in accordance with stripping theory. However, the angular distributions change quite rapidly with energy and those for final states of the same spin and parity are quite different. Both facts favouring compound nucleus formation. Most of the authors suggest both processes are occurring, but favour direct interaction at higher energies. One would expect the distributions to become more isotropic at higher energies for CN production (section 1.1). In fact the distributions remain anisotropic.

It is interesting to note with reference to the present work that both Bromley (Br 57) and Towle and Macefield (To 61) make the point that since the distributions change quite rapidly with energy, especially in the region of the higher resonances, a measurement of the total cross section would be required to locate accurately the resonances to levels of O^{15}.

Using the 3 MeV accelerator at Chalk River Bromley et al (Br 57) investigated the $C^{12}(He^3,n)O^{14}$ reaction from 1 to 3 MeV. They measured angular distributions at four different energies, 1.89, 2.16, 2.40 and 2.51 MeV as well as excitation curves of $\frac{d\sigma}{d\Omega}$ at 0° and 90° up to 3 MeV. They found pronounced resonance structure. They integrated their differential cross sections to give approximate values for the total cross section at each of the energies mentioned. The neutron angular distributions show a change from isotropy to asymmetry characteristic of stripping. There is also evidence in the 90° excitation curve for resonances at 2.1 and 2.5 MeV. It was concluded that these results were best explained as a mixture of compound nucleus and direct interaction.

Towle and Macefield (To 61) used the neutron time of flight technique to investigate the reaction. Nearly all the known levels of O^{14} are due to this paper. They measured 0° and 90° excitation functions and angular distributions up to 5.26 MeV. They compared the results with a double stripping theory and suggest that a direct process is competing strongly with compound nucleus formation.

Ajtenberg and Dunning (Aj 61) extended the excitation function to 5.5 MeV.

Gale et al (Ga 60) measured angular distributions at 4.09, 4.62, 5.16 and 5.70 MeV to test Newns' double stripping theory. They obtained a reasonable fit with spherical Bessel functions. The authors point out that in a (He^3,n) double stripping reaction the selection rules are very restrictive. For X(He^3,n)Y

$$\underline{Jy} = \underline{Jx} + \underline{l} + \underline{s}$$

where s = combined spin of He^3 + n.

l = combined orbital A.M., and is restricted by parity selection.

Where Jx or Jy is zero as here l is single valued. This immediately gives a unique spin assignment for the other Jx or Jy. They suggest that this may be a useful spectroscopic tool if double stripping is dominant.

Manley (Ma 63) investigated the angular distributions from 19 to 23 MeV. He found double stripping to be the dominant process for these energies.

This was the state of the $C^{12}(He^3,n)O^{14}$ reaction at the commencement of the present work.

The Present Work.

Introduction

As seen in section 3.1. the $C^{12}(He^3,n)O^{14}$ reaction has been studied by several groups in recent years because of interest in the reaction mechanism. Both it and the $C^{12}(He^3,p.)N^{14*}$ reaction show three corresponding resonances in the region of 2 to 3 MeV bombarding energy,

and this strongly suggests a compound nucleus mechanism for this region.

Whilst the present work was in progress three reports on the $C^{12}(He^3,n)O^{14}$ reaction have been published. Fulbright et al (Fu 62) have extended the 0^o excitation function up to 11 MeV, finding more structure, and carried out angular distribution measurements at a number of energies up to 10.75 MeV. They found very strong forward peaking in the 5-10.75 MeV range and on the basis of fits by double stripping theory to these forward peaks expressed a strong view that a direct reaction mechanism was dominant at these higher energies.

Din et al (Di 64) have recently published work on 0^o and 90^o excitation functions and more angular distribution data for the region below 5.2 MeV. They also made a direct measurement of the total cross section as a function of energy up to 5.2 MeV. Kuan et al (Ku 64a) have made a general study of C^{12}+ He^3 for all possible reaction channels in the 2-3 MeV region and have obtained consistent fits to the data using dispersion theory and including interference between broad compound nuclear states.

In the present experiment it was planned to measure the total cross section as a function of energy from threshold to 11.5 MeV, using the Canberra Tandem accelerator and helium injector. This could be done conveniently using the activation technique (section 1.5) since 99.4% of the positron decay of the O^{14} nuclei proceed via the 2.31 MeV first excited state of N^{14} (section 3.2). Hence the 2.31 MeV γ-ray yield provides a measurement of the total cross section for the reaction. Since the threshold for breakup of the O^{14} into N^{13} + p occurs below

FIG. 3·4 The positron decay scheme of O^{14}.

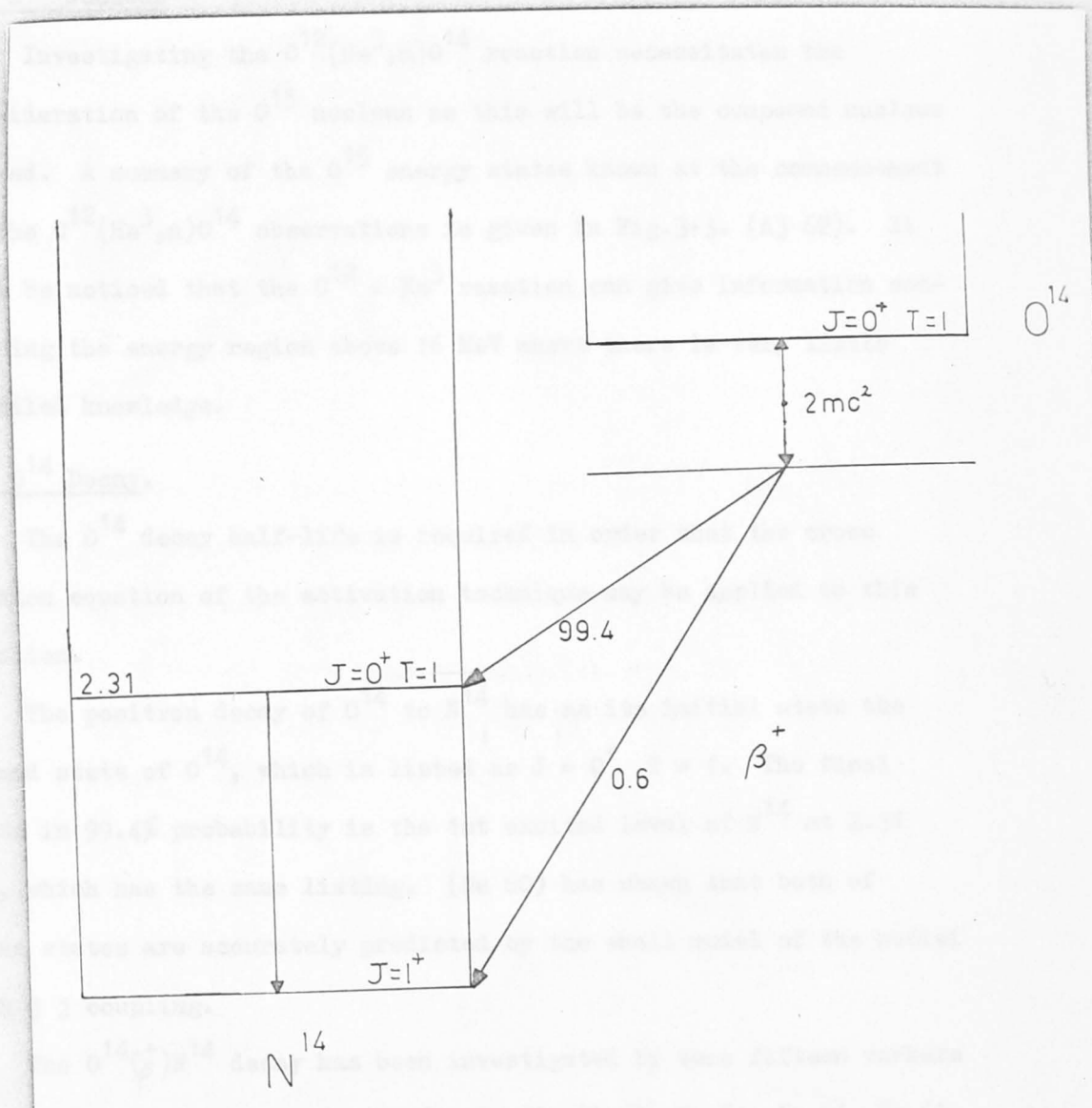

FIG 3·4.

the known first excited state of O^{14}, the method yields the cross section for neutron transitions to the ground state uniquely.

The O^{15} Nucleus

Investigating the $C^{12}(He^3,n)O^{14}$ reaction necessitates the consideration of the O^{15} nucleus as this will be the compound nucleus formed. A summary of the O^{15} energy states known at the commencement of the $C^{12}(He^3,n)O^{14}$ observations is given in Fig.3·3. (Aj 62). It will be noticed that the C^{12} + He^3 reaction can give information concerning the energy region above 16 MeV where there is very little detailed knowledge.

The O^{14} Decay.

The O^{14} decay half-life is required in order that the cross section equation of the activation technique may be applied to this reaction.

The positron decay of O^{14} to N^{14} has as its initial state the ground state of O^{14}, which is listed as $J = 0^+$ $T = 1$. The final state in 99.4% probability is the 1st excited level of N^{14} at 2.31 MeV, which has the same listing. (Wa 60) has shown that both of these states are accurately predicted by the shell model of the nuclei with j j coupling.

The $O^{14}(\beta^+)N^{14}$ decay has been investigated by some fifteen workers (Al 58, Ge 59, Ja 59, Ba 60, Du 60, Ho 60, Bl 61, Bu 61, Ha 61, Ho 61, Al 62, Ba 62, Ma 62, We 62, Bl 62) with the result that the decay scheme of Fig. 3·4 is well established as is the half-life of 72.1 $\pm$ 0.4 secs.

FIG.33 A gamma-ray spectrum taken with one of the 3" x 3" NaI(Tl) spectrometers after bombardment of the C^{12} foil with He^{3++} ions of 6.75 MeV. The hatched area indicates the energy interval selected for the yield measurements.

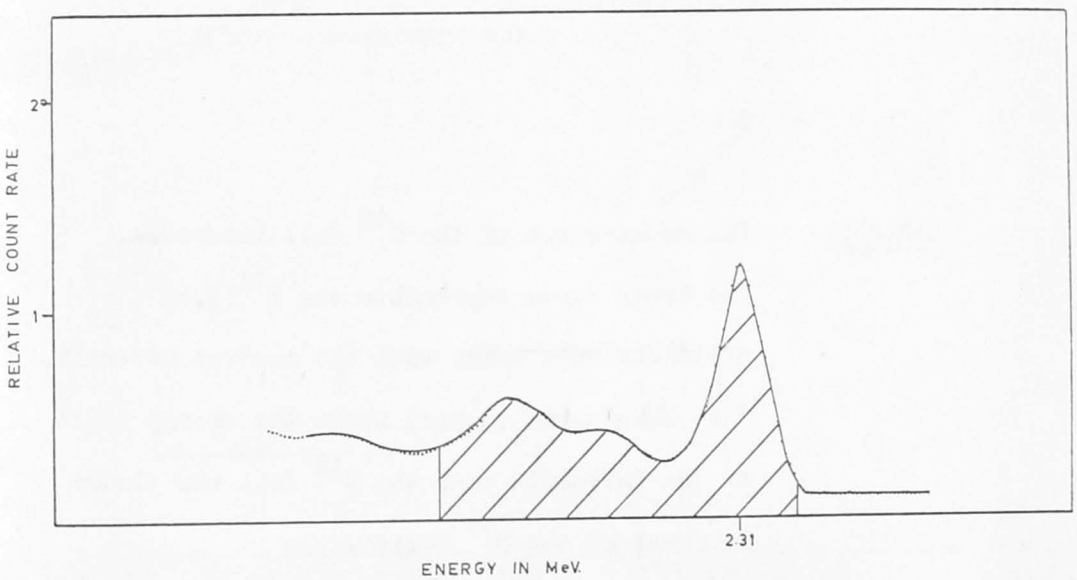

FIG. 33.

FIG. 34 The measurement of the C^{12} foil thickness. The lower curve represents the $B^{11}(p,n)$ threshold data taken with the neutron detector. The other curve (upper) shows the energy shift of the threshold when the C^{12} foil was placed in front of the B^{11} target.

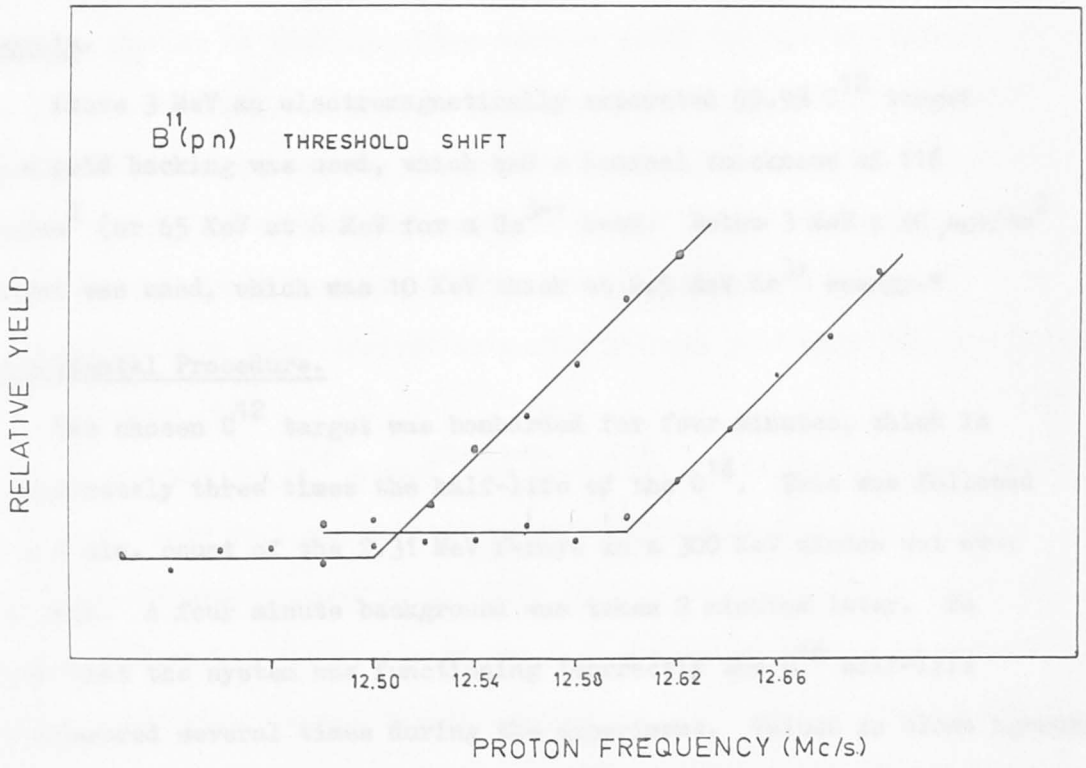
$B^{11}(p\,n)$ THRESHOLD SHIFT
RELATIVE YIELD
12.50
12.54
12.58
12.62
12.66
PROTON FREQUENCY (Mc/s.)

FIG. 34.

The Apparatus.

The apparatus employed was basically similar to that used in earlier activation studies in this laboratory (Ea 63). The only major modification was the introduction of a 'leaky' integrator (section 1.6) for measuring the total charge incident on the target. This was necessary as, in the early stages of operation of the He^3 injector, the beam tended to fluctuate considerably.

Targets.

Above 3 MeV an electromagnetically separated 99.9% C^{12} target on a gold backing was used, which had a nominal thickness of 116 $\mu gm/cm^2$ (or 65 KeV at 6 MeV for a He^{3++} beam. Below 3 MeV a 40 $\mu gm/cm^2$ target was used, which was 10 KeV thick at 2.5 MeV He^{3+} energy.*

Experimental Procedure.

The chosen C^{12} target was bombarded for four minutes, which is approximately three times the half-life of the O^{14}. This was followed by a 4 min. count of the 2.31 MeV γ-rays in a 300 KeV window set over the peak. A four minute background was taken 2 minutes later. To check that the system was functioning correctly the O^{14} half-life was measured several times during the experiment. Values in close agreement with the accepted figure of 71.0 seconds (Ba 62) were obtained. Counting losses were kept below 1% (section 3.1.4.). By placing a $\frac{1}{8}$" lead shield in front of the crystals the ratio of the counts in the 2.31 MeV peak to those in the 0.511 MeV peak was improved considerably. Coincidences between the 2.31 MeV γ-rays and the annihilation radiation were observed

---

* We are indebted to the Harwell Electromagnetic Separation Group who prepared these targets.

but were not used as the count rate was too small.

The range from threshold to 11.45 MeV was covered initially in 150 KeV steps. Where necessary to confirm the observed structure 75 KeV increments were used. Below 3 MeV the thinner target was used and the energy steps reduced to 37.5 KeV. The spectrum is shown in Fig. 35.

Absolute Cross Section.

To provide an absolute cross section scale for the excitation function a self-supporting natural carbon target was made. With this the yield per micro-coulomb was measured at several energies to provide a good fit to the curve. Measurements of the target thickness and efficiency of the NaI crystals for the detection of the 2.31 MeV γ-radiation were then required to enable a cross section to be calculated from equation (1).

To prevent the O^{14} nuclei from recoiling out of the counting region a 3 mg/cm^2 gold foil was mounted immediately behind the carbon foil. In the yield measurements an R.I.D.L. 400 channel pulse height analyser was used to enable the counts in the 2.31 MeV photo-peak to be corrected for an underlying Compton background and the 0.511 - 2.31 coincidence peak. The total charge in micro-coulombs incident on the target was measured with an ELCOR current integrator model A 309A.

The target thickness was measured by the displacement in the $B^{11}(p,n)C^{11}$ threshold energy which resulted following its insertion into the beam. The neutrons were detected with a boron loaded plastic scintillator type (N.E.401.). A value of 4.6 KeV $\pm$ 10% was obtained

at E_p = 3.02 MeV which gave a target thickness of 43 μgm/cm^2. (Fig.34).

To determine the crystal efficiency a standard Na^{22}(1.28 MeV line) and a non-standard thorium source (2.61 MeV line) were used as follows:-

First the ratio of the shielded to the unshielded efficiency was measured at 1.28 MeV and 2.61 MeV; linear interpolation then gave this ratio at 2.31 MeV. Then the unshielded efficiency for the crystal was measured at 1.28 MeV and compared with the tables (Ke 58). The measured efficiency was 7% lower than that indicated by the tables. The efficiency at 2.31 MeV therefore was taken as the tabulated value reduced by 7%. The corrected shielded efficiency was then found to be 4.8% at 2.31 MeV.

The measurement of the total cross section was carried out at 3.0, 3.3 and 6.6 MeV. The values obtained are given in table 2.

Table 2

Absolute cross section measurements.

E (MeV)	σ (mb)
3.00	15.2 ± 2.0
3.30	5.6 ± 0.7
6.60	26.2 ± 3.7

The distribution of errors shown in Table 3 places a probable error of 13% on the cross section scale attached to the excitation function.

Table 3

Errors in Absolute Cross Section.

Source of error	Percentage.
Fit to excitation function	7%
Target Thickness	10%
Detection efficiency	5%
Dead time loss correction	1%
Decay Constant	0.1%
R.M.S.	13%

Results and Discussion.

Fig. 35 shows the excitation function from threshold to 11.45 MeV. The curves used in obtaining the final excitation function were all in good agreement and the peaks which appear in the final averaged curve also appeared in the individual curves. The error bars assigned are the mean square deviations of the component curves from the average at each point. The total cross section at 3 MeV is (15.2 $\pm$ 2.2) m b and agrees within the errors with that measured by Din et al (Di 64). However, above 4.5 MeV the cross sections obtained in this experiment are smaller than those of Di64.

The thin target experiment gave evidence for the previously observed resonances at 2.45, 2.70 and 2.99 MeV corresponding to levels in O^{15} at 14.03, 14.23 and 14.43 MeV excitation. Detailed investigations

on these levels has recently been reported by Kuan et al (Ku 64a) and Lindeman et al (Li 63). The weak resonances reported by Bromley et al (Br 57) were not observed in this work.

Other resonances appeared in the excitation function at laboratory He^3 energies of 4.65, 5.10, 5.85, 6.80, 7.70, 8.70 and 9.80 (all $\pm$ 0.05) MeV. These may be associated with previously unknown levels in O^{15} at 15.79, 16.15, 16.75, 17.50, 18.23, 19.05 and 19.91 ($\pm$ 0.05) MeV respectively.

As can be seen some of the resonances are broad and may indicate short lived compound states of the O^{15} system. However, the spacing of the known O^{15} levels at these excitations is of the order of 500 KeV, while for levels in the analogue N^{15} nucleus it is approximately 200 KeV. The spacing of the resonances in the present excitation function is about 700 KeV, which suggests that either not all the available states are being excited (and it should be remembered that in the present case only $T = \frac{1}{2}$ states are available, whereas in N^{15} the first $T = 3/2$ state lies as low as 11.61 MeV), or that the peaks observed represent groups of unresolved levels. The trend of the peak to valley ratio with energy suggests a rising cross section underlying the structure which may be due to a direct interaction mechanism as is suggested by the angular distribution measurements. The fall off in the cross section above 10 MeV could be due to the opening up of new reaction channels to the excited states of O^{14}.

A comparison of the present excitation function with that obtained by Din et al (Di 64), with the 0° excitation functions of Towle and

FIG.35 The total cross section for the $C^{12}(He^3,n)O14$ reaction as a function of energy from threshold to 11.5 MeV.

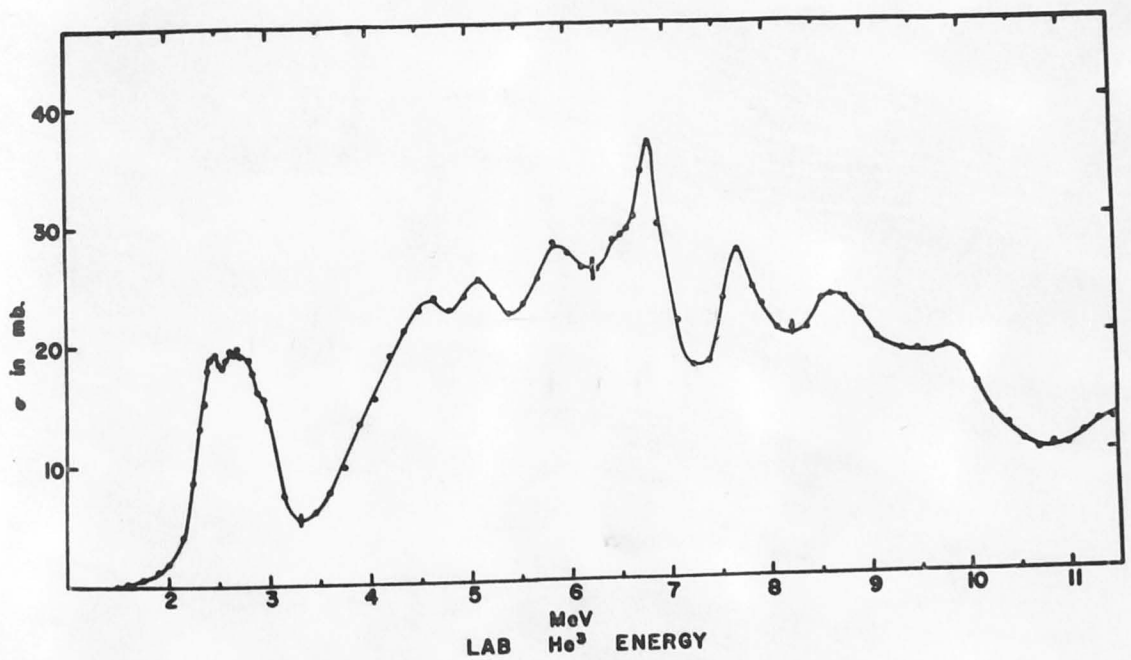
40
30
20
10
σ in mb.
2
3
4
5
6
7
8
9
10
11
MeV
LAB He³ ENERGY

FIG. 36 A comparison of the data on the O^{15} nucleus.

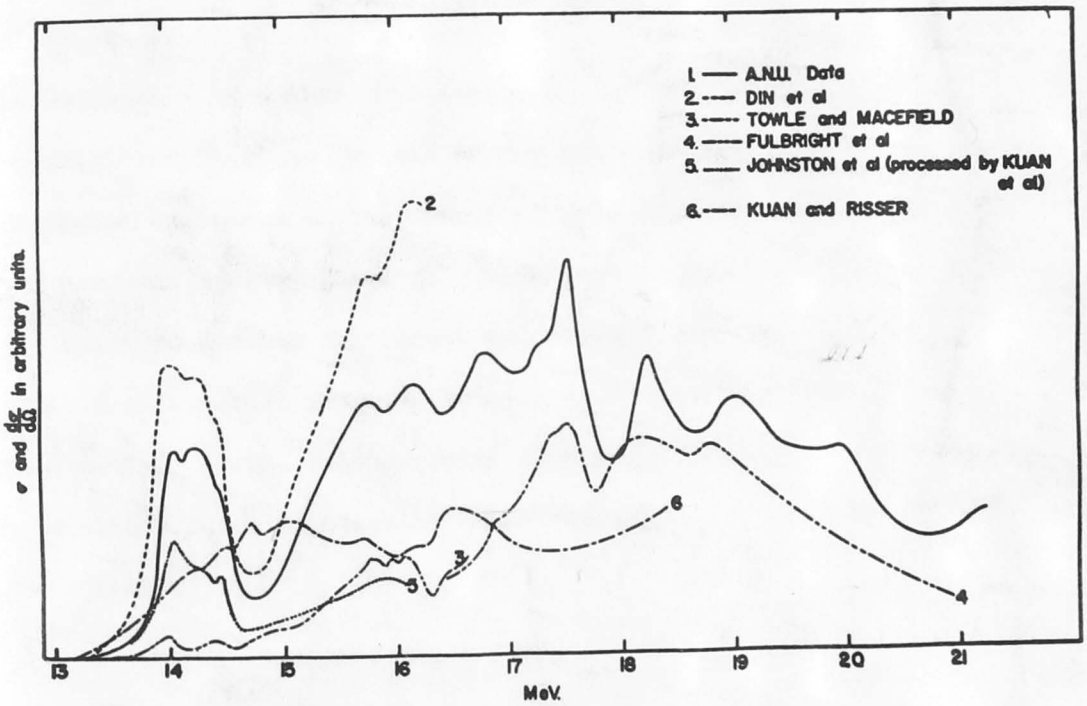

O^{18} EXCITATION.

Macefield (To 61) and Fulbright et al (Fu 62) is shown in Fig. 36, where the energy scale is the excitation energy in O^{15}. Included also on the same plot are excitation functions for the reactions $C^{12}(He^3,p_1)N^{14}$ (Ku 64a) and $N^{14}(p,n)O^{14}$ (Ku 64b) which have the same compound nucleus.

The overall data does not support the strongly expressed view of Fulbright et al (Fu 62) that above 5 MeV the reaction proceeds predominantly as a direct process. The forward peaking of the angular distributions in this energy range is striking, but can be partially explained as the result of interference between levels in the compound system; there will also be interference effects between the compound nuclear and direct mechanisms. The structure in the excitation function reported here is too marked for explanation by fluctuations of the Ericson type. The structure observed appears to be evidence for a substantial contribution by the compound nucleus mechanism.

* * * * * * * * * * *

CHAPTER IV

The Al^{27} Investigations

4.1 Introduction

For various reasons such as checks on the validity of nuclear model predictions, nuclei in the 2s1d shell have been examined in some detail (Fe 55, Go 56, Th 60, Th 62). In particular Ophel and Lawergren at the A.N.U. investigated the Al^{27} nucleus in much detail up to 3.0 MeV (Op 62, Op 62a, Op 63, La 62, La 62a) to determine accurately the spins and decay properties of the low-lying levels. The results were used to test the validity of various nuclear models. The interest in the present work was to extend the results to the levels above 3 MeV if possible and to check several points e.g. the spins of the 2.73 MeV level and the 2.98 MeV level and the $\frac{\text{quadrupole}}{\text{dipole}}$ amplitude mixing ratio for the 2.98→0 transition.

The low lying levels of Al^{27} can be examined reasonably conveniently by means of

(i) The $Mg^{26}(p\gamma)Al^{27}$ reaction at the various resonances. The study of the cascade γ-rays will provide information on level spins, γ-ray de-excitation modes and γ-ray quadrupole/dipole mixing ratios. As pointed out in section 1.4, the interpretation of the experimental results is much simplified in cases such as Mg^{26} targets where the target spin is zero and the proton is captured into a single compound state of

well defined spin and parity. The resonance level de-excites to the lower energy levels. If the resonance level spins have been determined the angular distributions of the de-excitation γ-rays can determine the spins of the low lying levels.

(ii) The $Al^{27}(p,p'\gamma)$ Reaction.

When Al^{27} is bombarded with protons between 2 and 5 MeV energy the most probable processes are scattering and the (p,α) reaction. The γ-ray yields from the inelastic scattering process are very much higher than can be obtained from the $Mg^{26}(p,\gamma)Al^{27}$ resonances. Because of this high yield low efficiency detector arrangements, such as the T.C.S. or single detectors in coincidence, can be used to simplify and resolve the γ-rays from the de-excitation of the low lying levels. As long as the bombarding energy stays fixed and the target thickness is unchanged for a particular measurement the population of the magnetic substates of a particular level remains constant and the correlation data can be analysed in terms of the population parameters of the level. This technique has been used by Ophel and Lawergren (La 63) with success on the levels up to 3.0 MeV in Al^{27}. However they found that for proton energies up to about 6 MeV the levels above 3.0 MeV could not be excited with sufficient intensity. The proton energy was extended up to 9.0 MeV in an attempt to excite the 3.68 MeV level and higher levels by the $(p,p'\gamma)$ reaction. Again it proved not possible to excite any level above 3.0 MeV with an intensity that would warrant systematic investigation. (The inelastic scattering of alpha particles from Aluminium was also investigated to see if this process would excite the 3.68 MeV or higher

levels. As in the proton case no success was achieved with the alpha scattering process.)

Since the two inelastic scattering processes were unsuccessful it was necessary to return to an investigation of the $Mg^{26}(p,\gamma)$ resonances. At resonances investigated to date it has been shown that the 3.68 MeV level is excited at the 339 KeV, 661 KeV, 721 KeV, 839 KeV, and 954 KeV resonances. (Va 56, Op 62). Of these the 661 KeV resonance and the 839 KeV resonance both have spin $\frac{1}{2}$. This severely limits the information obtainable from the correlation data. e.g. The angular distribution of the r→3.68 MeV γ-ray would be isotropic. The mixing ratio cannot, therefore, be determined. This then necessitates a two parameter analysis of the triple angular correlation data. (The two parameters being X, X_1). The 339 KeV resonance is very close to a strong $F^{19}(p,\alpha\gamma)O^{16}$ resonance and hence very clean targets must be used or a large background will result that will be troublesome. The 721 KeV resonance, however, is not spin $\frac{1}{2}$ and is not close to a $F^{19}(p\alpha\gamma)O^{16}$ resonance and so results may be forthcoming from measurements at this energy.

Neither the 2.98 MeV nor the 3.0 MeV levels are excited to any appreciable amount at any of the $Mg^{26}(p,\gamma)$ resonances so far explored. The decision was made, therefore, to investigate other unexplored resonances within the capability of the Cockcroft-Walton accelerator (below 1.2 MeV). The resonances explored were those at 991 KeV, 1015 KeV and 1056 KeV. Of these only the 991 KeV resonance populated the 2.98 MeV level.

Unfortunately there are shortcomings that arise out of having to

investigate $Mg^{26}(p,\gamma)$ resonances in order to obtain information on the low-lying levels of Al^{27}. The excitation in the compound nucleus is about 9 MeV. Hence a cascade must occur before levels in the 3-4 MeV region are populated. To analyse the data on these low-lying levels it is necessary to determine several parameters, such as the resonance spin and the r $\rightarrow$(low-lying level) $\frac{\text{quadrupole}}{\text{dipole}}$ mixing ratio (X), which are not of immediate interest. In addition many of the resonances have several cascades occurring simultaneously, giving rise to a complex spectrum that is difficult to analyse accurately unless coincidence techniques (such as those described in Chapter II) are used, with the subsequent addition to the time scale of the investigations.

At the time of the present measurements the spins and parities of the first four excited states of Al^{27} were known. The spins of the doublet levels at 3 MeV were unknown (apart from a tentative assignment of 3/2, albeit by several investigations (Va 56, La 62). (La 62) had suggested that the 721 KeV resonance was either spin 3/2 or 5/2 because of the r $\rightarrow$ 2.21 transition.

4.2 Experimental Procedures.

Accelerators

All of the investigations carried out on the $Mg^{26}(p,\gamma)Al^{27}$ resonances were made with the Canberra Cockcroft-Walton 1.2 MeV accelerator (Ba 61). The proton currents were limited to about 10μA on the target except when water cooled targets were used. The water-cooling enabled currents up to about 80μA to be employed. The energy stability of the accelerator was about $\pm$ 2 to 3 KeV.

The $Al^{27}(p,p'\gamma)$ and the $Al^{27}(\alpha,\alpha'\gamma)$ investigations demanded proton and alpha particle energies well above 1 MeV. These experiments were carried out with the Canberra Tandem van de Graaff accelerator. The intensity of the proton and alpha beams was adjusted to keep the pulse height analyser dead time and the random coincidence rate corrections small.

Target Chambers

The target chambers were made of plexiglass to facilitate any optical alignment that may be necessary and to reduce the γ-ray absorption to a minimum. The water cooling provision was only provided in the $Mg^{26}(p,\gamma)Al^{27}$ case. (Ba 63a, Ba 61) give full descriptions of the target chambers and angular distribution tables employed.

Targets

For the inelastic particle scattering from Aluminium only natural Aluminium targets were used. These targets were prepared by evaporating natural aluminium in vacuo.

In the case of the $Mg^{26}(p,\gamma)$ resonances targets of enriched (>98%)Mg^{26} on thick copper backings were used. These were prepared by evaporating $Mg^{26}O$ from a tantulum strip in vacuo onto the copper. The tantulum reduces the oxide, hence liberating the magnesium. The copper backing had been carefully cleaned before hand to remove all contaminants such as F^{19}.

The magnesium proved by far the more difficult to evaporate in large quantities and only thin targets could be produced (about 4 KeV thick for 1 MeV protons). In an attempt to produce thicker magnesium

targets the magnesium was evaporated onto water-cooled tantulum. The water cooling enabled the backing material to be placed closer to the $Mg^{26}O$ layer on the tantulum strip. This was not successful, however, and thicker targets were not produced.

Detection System

1. $Mg^{26}(p,\gamma)Al^{27}$.

The γ-ray detectors used were two 5" x 4" NaI(Tl) scintillation crystals (Harshaw) optically coupled to 3" Dumont photomultiplier tubes. The photomultipliers were supplied with the required high voltage (about 900 volts) by high voltage supplies (John Fluke Mfg. Co. Inc.) that were continuously adjustable from 0 to 3000 volts. Further amplification was provided by pre and main amplifiers model A8 from Franklin Electronics Inc.. Double delay line amplifiers are particularly suitable because of their ability to handle heavy overload pulses without introducing excessive dead time, and their ability to handle high count rates without excessive base line shifts. Also, time jitter can be greatly reduced by using discriminators and single channel analysers which trigger off the cross-over point of these pulses. Such reduced time jitter allows smaller resolving times to be used in any coincidence circuits and therefore reduces the accidental coincident rate.

Pulses from the line shapes of the coincident γ-rays to be measured were selected by means of single channel analysers and used to gate the spectrum in the other crystal.

Throughout the whole of this thesis a Cosmic Radiation Lab. Inc. model 801 multiple fast-slow coincidence unit was used. The

resolving time of the slow unit was $2\tau = 2$ μsec and that of the fast unit was $2\tau = 0.050$ μsec. The resolving time of the fast unit was capable of variation from 0 to 0.180 sec. The lowest value which could be used without losing true coincidences however, was limited to 0.050 μsec by the time jitter of the cross over points of the pulses from the amplifiers. The beam current was measured by an Elcor Model A309B current integrator which was accurate to ± 1%. The analysis of detector spectra was carried out by pulse height analysers of two varieties.

(i) 400 channel display manufactured by Radiation Instruments Development Laboratories (R.I.D.L.)

(ii) The much more extensively used 512 channel display instrument manufactured by R.C.L.

Angular Measurements

All of the counters and the target chamber were optically aligned with a theodolite, and checked each day by measurements of the angular distribution of the isotropic yield from the reaction $Mg^{26}(p,\gamma)$ at $E_p = 839$ KeV. This reaction yields isotropic γ-rays from the $r \rightarrow 1.01$ MeV transition (8.05 MeV). The 8.05 γ-ray was selected by a single channel analysers and fed to A.N.U. scalers. Any deviations from isotropy were used to correct subsequent measurements accordingly.

In general angular distributions were measured by recording spectra at six equal intervals of $\cos^2\theta = 0.0$, 0.2, 0.4, 0.6, 0.8, and 1.0. Occasionally only $0^\circ/90^\circ$ ratios were taken, to check measurements previously made usually. Measurements at a constant bombarding energy, for example angular distributions, were monitored by one counter in a

fixed position. The yields in various energy regions were counted by fast scalers. Only those sets of data were used for which the ratios between the yields were constant (to within 2%).

The pulse height analysers employed count and record the length of time that the analyser is open for acceptance of pulses (T_c). The continuous laboratory time was measured by an electronic timer (T_1). In order to obtain the total number of pulses arriving to the pulse height analyser, the observed counts must be corrected with the ratio T_1/T_c. This correction was kept small ($<5\%$) since the accuracy depends on the beam intensity stability. (The R.C.L. clock pulses were subject to sizable errors, $\sim 5\%$. However, this was not important as the total dead time was kept small.

Geometrical Configurations

The measurements of triple angular correlations were carried out for Geometries I and II of Chapter I. Again, generally, the data were taken at the six intervals mentioned above for the double correlations.

The pulses from the rotating detector were displayed on the pulse height analyser and gated by a selected energy region of the detector at 90° to the beam. The 90° detector served as the monitor at the same time.

Geometrical Corrections

As discussed in Chapter I it is necessary to apply geometrical corrections to the angular distributions. The geometrical corrections are given in the text where appropriate.

Relative Intensities

To determine the relative intensities of the various -ray cascades spectra were measured at 55° to the proton beam. After dead time corrections, target and room background corrections the spectra were analysed into their component -rays by line shape analysis. Following this procedure the strongest transition was generally assumed to be of Intensity 100 units and all other -rays were normalized to these units, Gamma-ray efficiency corrections were applied from the Nuclear data sheets Part III. (U.S.A.E.C. 60). If the γ-ray energy was above 4 MeV the complete line shape was added; for energies of γ-rays below this value only the photo-peak was added the peak to total ratio (U.S.A.E.C. 60) being used to derive the total counts in the line shape, subtraction of higher energy γ-rays was achieved by the fraction of counts under the photo peak derived from the line shapes.

The line shapes for this line shape analysis were derived from the reactions cited in Chapter II.

Where possible the relative intensities were also computed by line shape analysis of all the γ-rays in the spectra taken at 55°.

Backgrounds

Studies of γ-rays induced by protons or alpha particles are frequently complicated by the presence of contaminants either in the target material itself or on the backing. In the case of proton induced reactions the most troublesome contaminant is F^{19} which gives rise, through the reaction $F^{19}(p,\alpha\gamma)O^{16}$, to 6 and 7 MeV gamma-rays.

The cross section for this reaction is generally several orders of magnitude higher than for (p,γ) reactions and fluorine compounds show an astonishing affinity for common backing materials. In the present $Mg^{26}(p,\gamma)$ resonances the F^{19} background manifested itself with a 6.14 MeV γ-ray at all the resonances.

Other important contaminants for protons are nitrogen which produces 4.43 MeV gamma-rays from the $N^{15}(p,\alpha\gamma)$ reaction, carbon which produces γ-rays from a number of $C^{12}(p,\gamma)$ and $C^{13}(p,\gamma)$ resonances and sodium which produces γ-rays from $Na^{23}(p,\gamma)$ and $Na^{23}(p,\alpha\gamma)$.

The amount of fluorine contamination depends greatly on the cleaning of the backing. The copper backing of the water cooled target was tested and found to be free of fluorine. The other target was fluorine contaminated, probably be being fingered. Considerable care was taken in preparing, storing and handling targets to ensure that no additional fluorine was added to the target.

Carbon contaminants generally build up on the target during bombardment. This can be reduced considerably by placing a cold surface as close to the target as possible. The present experiments did not experience carbon troubles as generally the beam currents were sufficient to heat the targets and so prevent the condensation of the carbon.

The main room backgrounds were from ThC^{11}(2.61 MeV) and K^{40}(1.46 MeV). These were observed with the beam off and subtracted from the resonance spectra.

The experiments were carried out only when the Tandem van de Graaff

FIG. 37 The 55° spectrum at the 721 KeV resonance of the $Mg^{26}(p,\gamma)Al^{27}$ reaction. The spectrum has been corrected for room background and dead time of the analyser but not for target background.

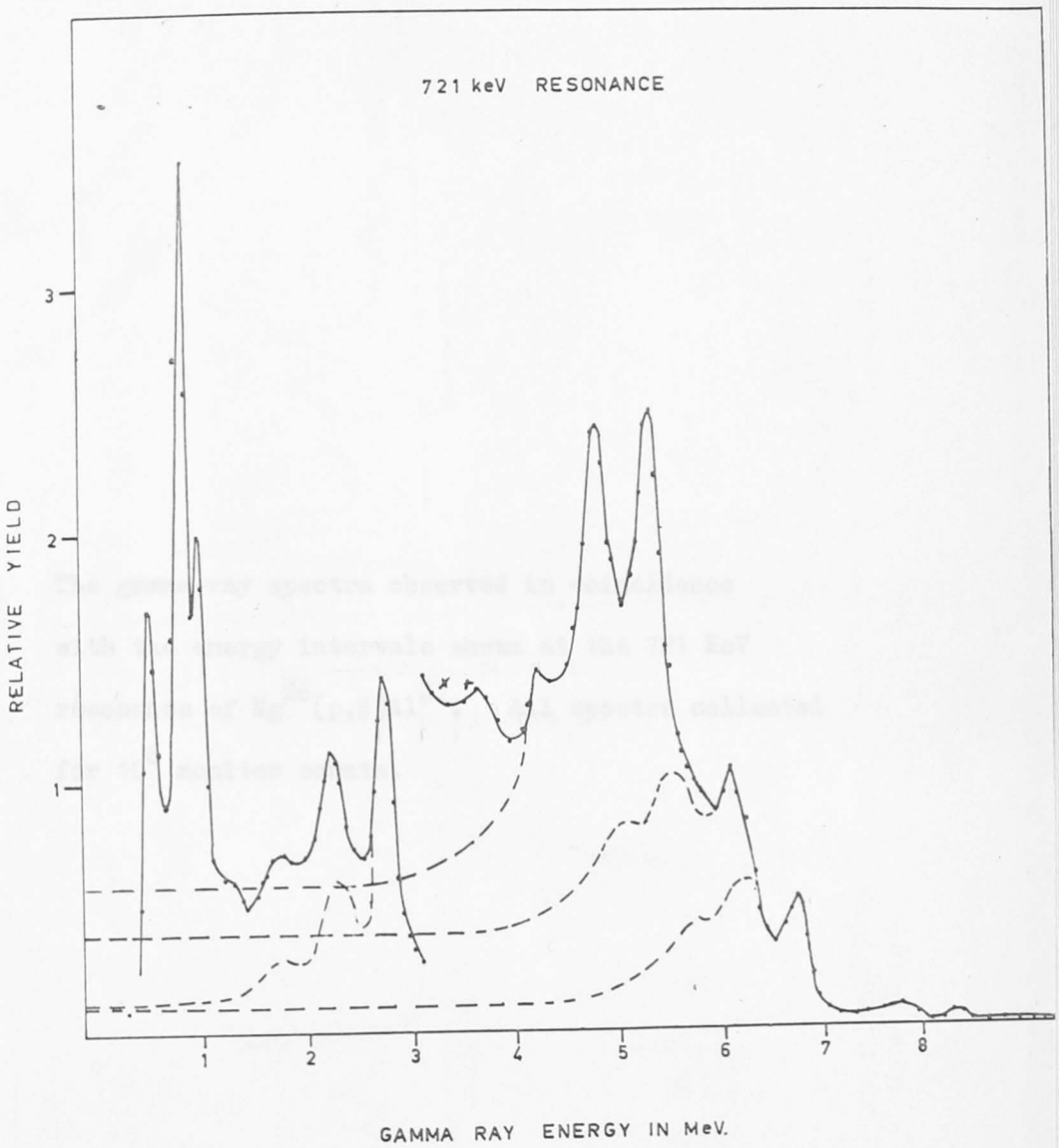
721 keV RESONANCE
RELATIVE YIELD
3
2
1
1
2
3
4
5
6
7
8
GAMMA RAY ENERGY IN MeV.

FIG. 37

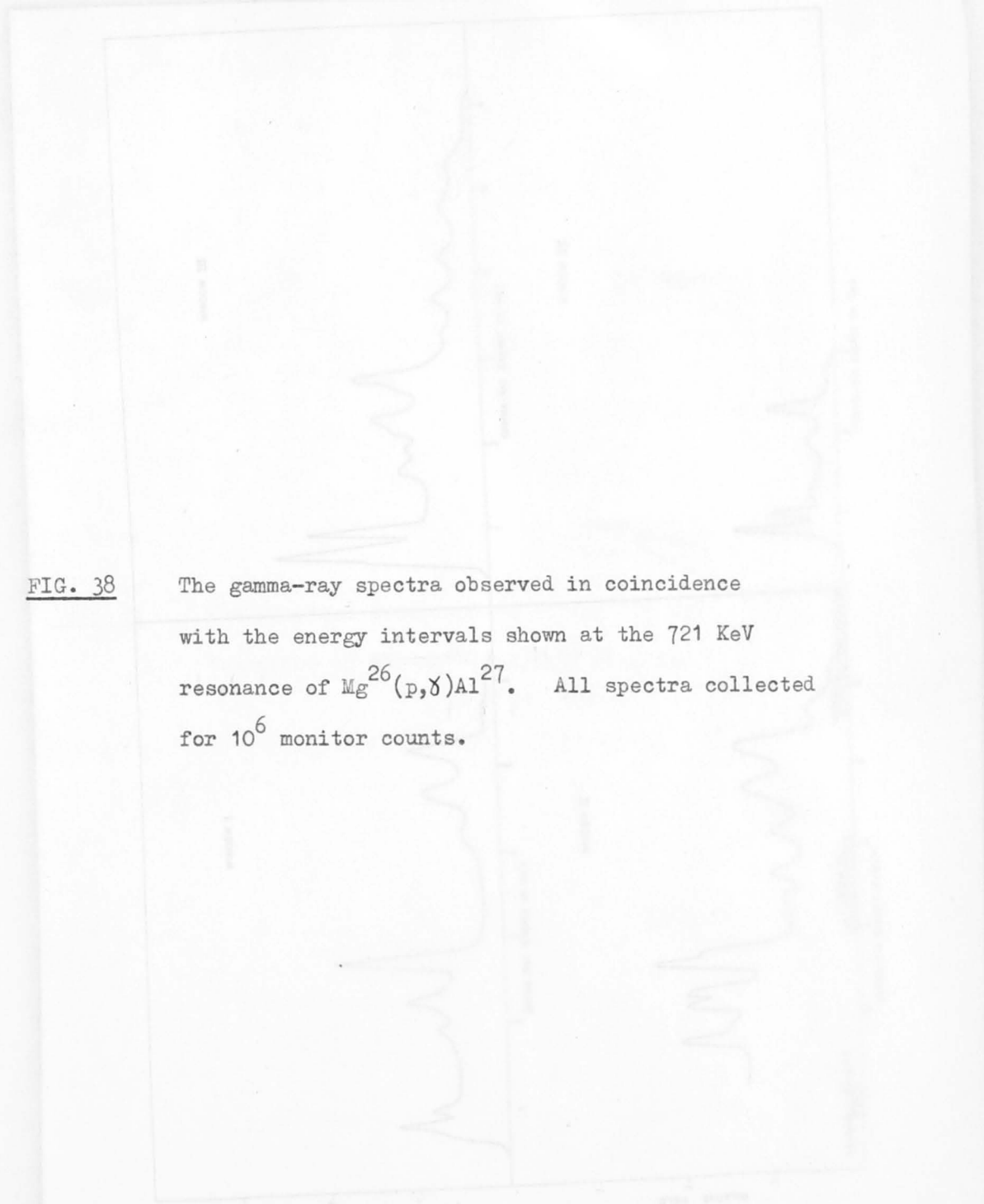

FIG. 38 The gamma-ray spectra observed in coincidence with the energy intervals shown at the 721 KeV resonance of $Mg^{26}(p,\gamma)Al^{27}$. All spectra collected for 10^6 monitor counts.

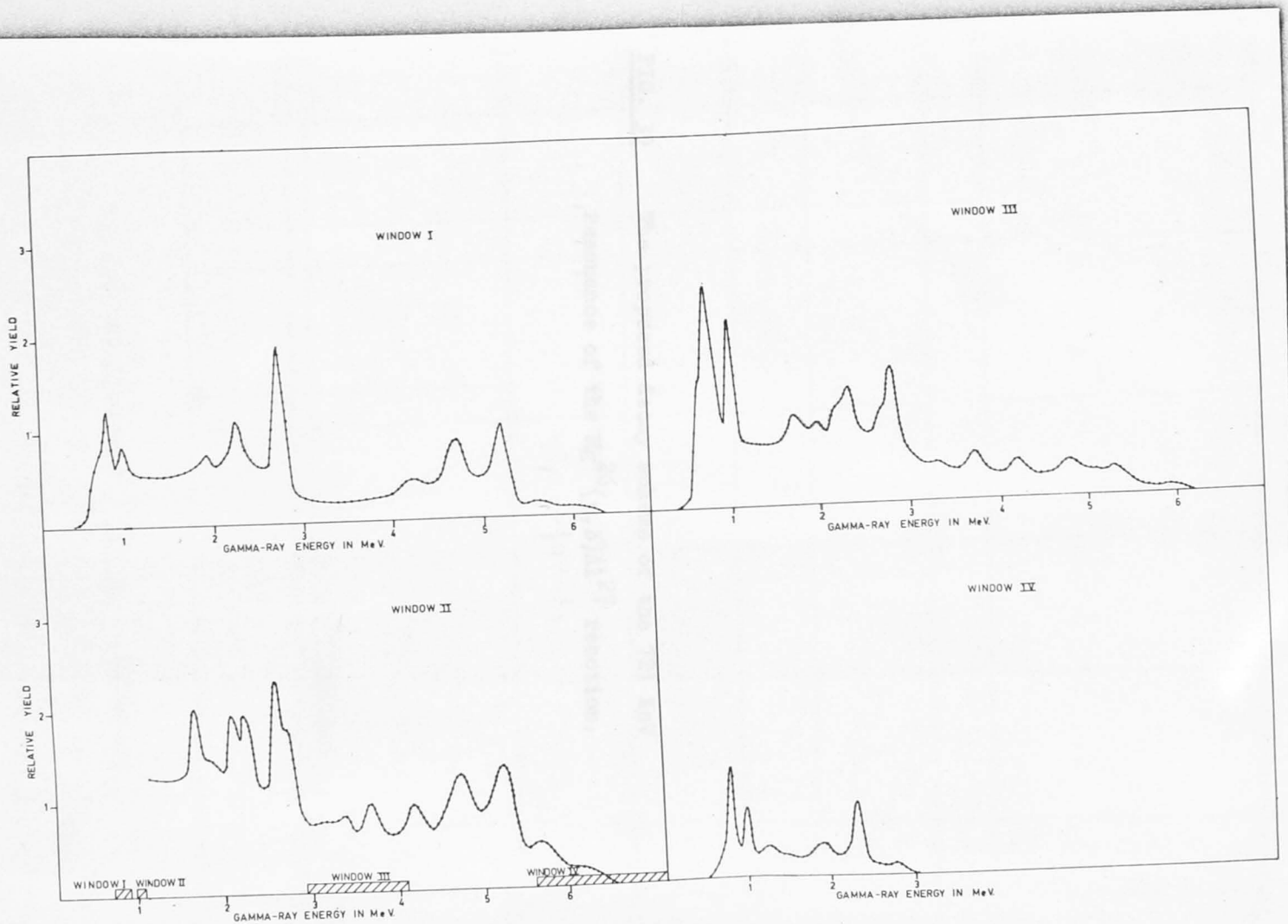
WINDOW I
WINDOW II
WINDOW III
WINDOW IV
RELATIVE YIELD
GAMMA-RAY ENERGY IN MeV.
WINDOW I
WINDOW II
WINDOW III
WINDOW IV

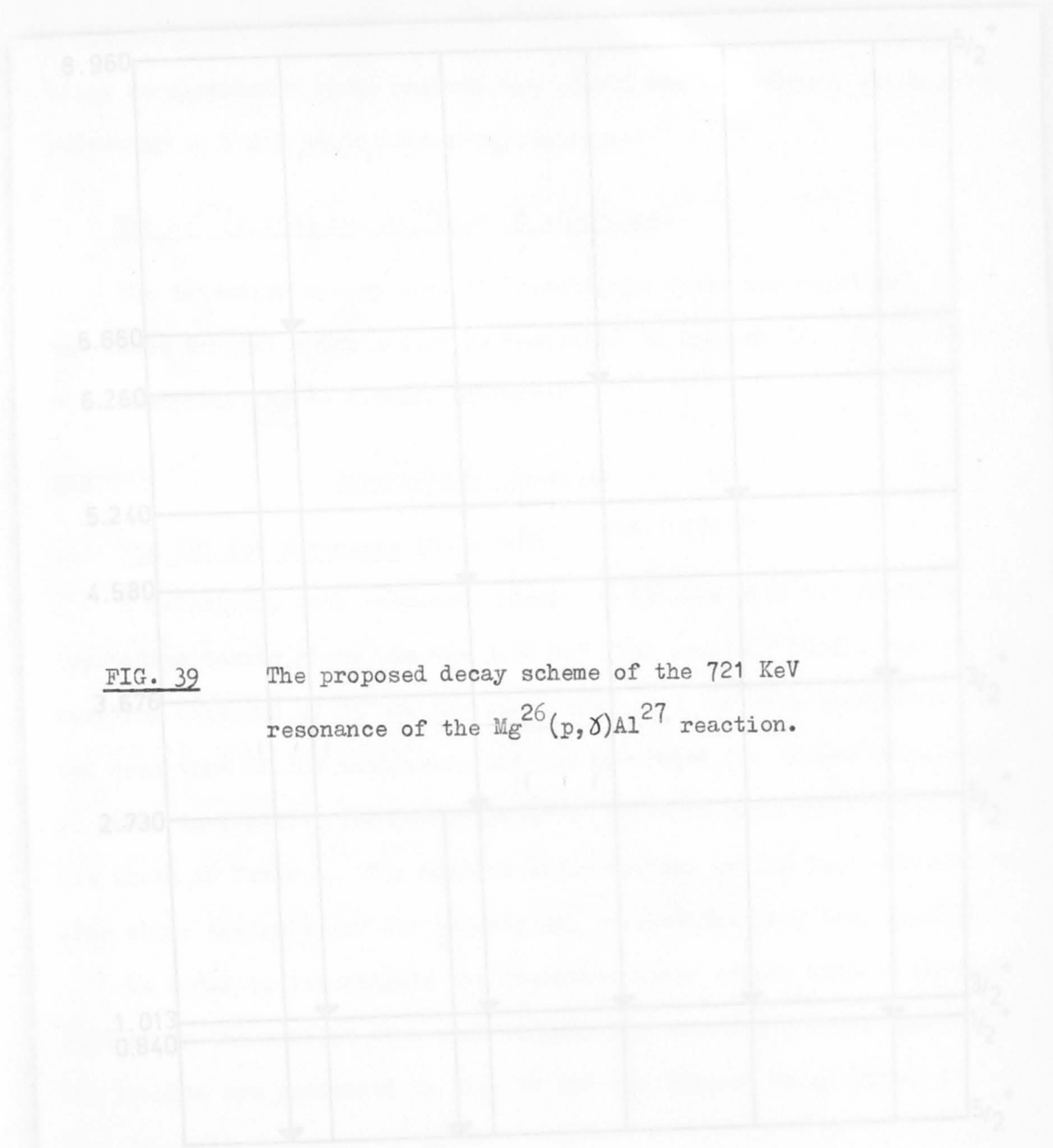

FIG. 39 The proposed decay scheme of the 721 KeV resonance of the $Mg^{26}(p,\gamma)Al^{27}$ reaction.

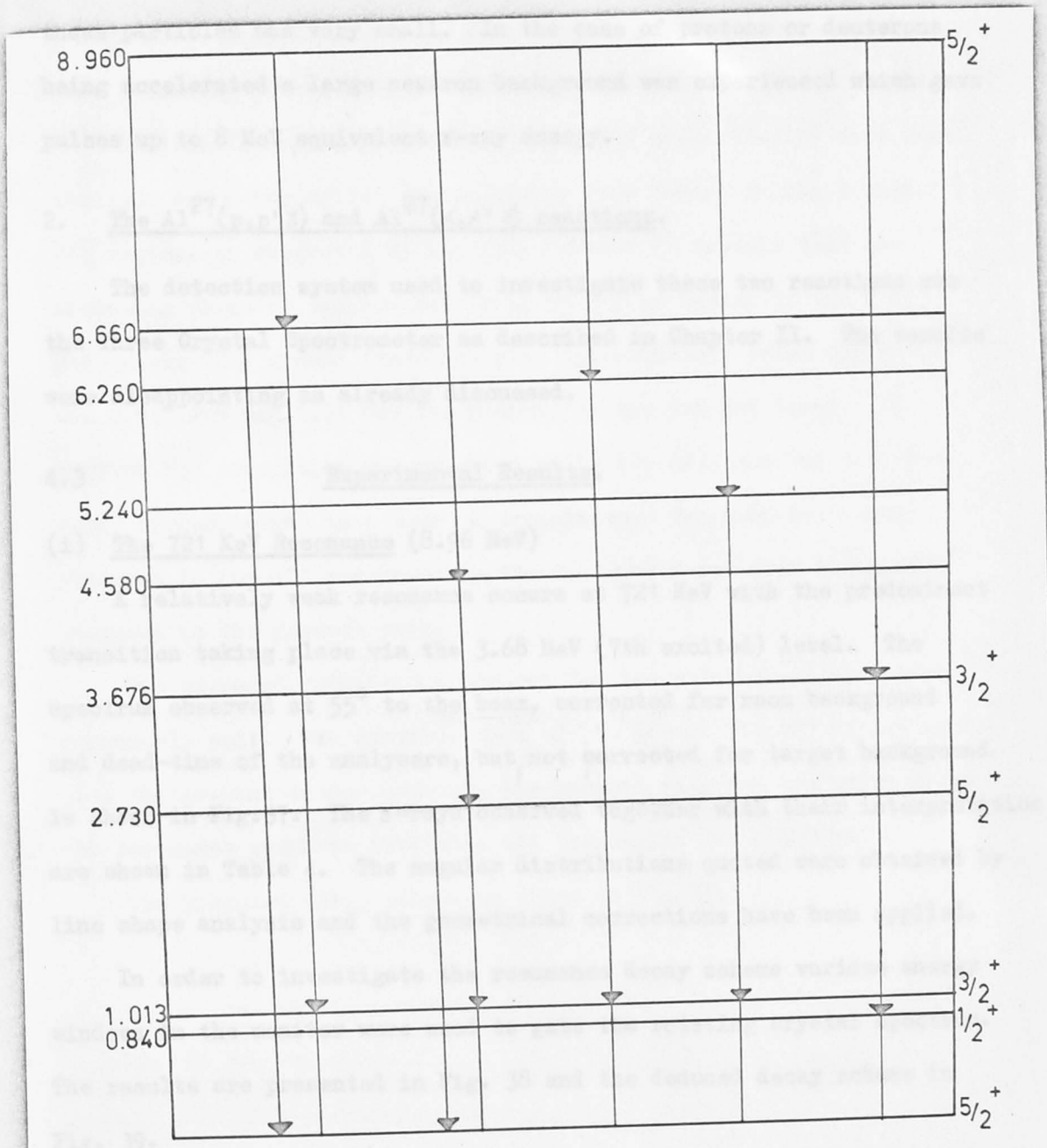

721 keV RESONANCE DECAY SCHEME

FIG. 39.

was accelerating He^3 or He^4 particles. The background produced by these particles was very small. In the case of protons or deuterons being accelerated a large neutron background was experienced which gave pulses up to 8 MeV equivalent γ-ray energy.

2. The $Al^{27}(p,p'\gamma)$ and $Al^{27}(\alpha,\alpha'\gamma)$ reactions.

The detection system used to investigate these two reactions was the Three Crystal Spectrometer as described in Chapter II. The results were disappointing as already discussed.

4.3 Experimental Results.

(i) The 721 KeV Resonance (8.96 MeV)

A relatively weak resonance occurs at 721 KeV with the predominant transition taking place via the 3.68 MeV (7th excited) level. The spectrum observed at 55° to the beam, corrected for room background and dead-time of the analysers, but not corrected for target background is shown in Fig.37. The γ-rays observed together with their interpretation are shown in Table 4. The angular distributions quoted were obtained by line shape analysis and the geometrical corrections have been applied.

In order to investigate the resonance decay scheme various energy windows in the monitor were used to gate the rotating crystal spectrum. The results are presented in Fig. 38 and the deduced decay scheme in Fig. 39.

In (Op 62) the 6.7 MeV γ-ray was attributed to a $r \rightarrow 2.21$ MeV transition (6.73 MeV). The present measurement demonstrated that the

6.7 MeV γ-rays were coincident with γ-rays with an energy of 2.34 $\pm$ 0.02 MeV. Thus these γ-rays arise from a r $\rightarrow$ 6.60 $\rightarrow$ 0 cascade. Some branching of the 6.60 MeV level via the 1.01 MeV level occurs.

Windows II and III (1.01 MeV, 3-4.5 MeV respectively) show that the 1.01 MeV γ-ray arises predominantly from γ-rays in the 3 to 4.5 MeV region, as suggested by (Op 62). Window IV reveals that the branching ratio of the 6.6 MeV level is 3/2 in favour of the 0.840 MeV level. The ground state decay is approximately twice the sum of the 0.840 MeV and 1.01 MeV transition for the 6.6 MeV level. No r$\rightarrow$3.00 MeV transition was observed as in (Op 62), nor any 3.00 MeV γ-ray corresponding to a 3.00 0 transition. The 6.00 MeV γ-ray observed in (Op 62) was probably the 6.14 MeV γ-ray from $F^{19}(p,\alpha\gamma)O^{16}$ observed in the present work.

The proposed transitions account for the relative intensities reasonably well. The previous data of (Va 56) or (Op 62) do not agree with the present data. However, the present data are preferred since the resonance was more carefully and thoroughly investigated.

The proposed decay scheme is shown in Fig 39.

Table 4 Gamma-rays observed at the 721 KeV Resonance.

γ-ray energy MeV	Interpretation	Calculated energy MeV	Geometrical Correction Factor	Angular Distribution	Relative Intensity
6.70 ± 0.05	6.60→0	6.60	-	-	26
6.14 ± 0.05	F^{19}	6.14	-	-	30
5.38 ± 0.05	r→3.68	5.26	0.79	$P_o-(0.22\pm0.05)P_2$	100
2.84 ± 0.05	3.68→0.840	2.84	0.78	$P_o+(0.22\pm0.01)P_2$	>97
2.34 ± 0.05	r→6.60	2.36	-	-	40
1.04 ± 0.04	1.01→0	1.01	-	-	50 *
0.840	0.840→0	0.840	-	isotropic	100 *
3→4.5 MeV	see decay scheme		-	-	-

* Separate intensity measurement.

(ii) The 809 KeV Resonance (9.03 MeV)

Apart from strong r→0 and r→1.01 MeV transitions observed at the 809 KeV resonance there is a relatively intense r→2.73→1.01 cascade. As this resonance was only investigated to check the spin of the 2.73 MeV level and the angular distribution of the r→2.73 MeV γ-ray had already been accurately measured (Op 62), measurements were carried out on the r→2.73→1.01 cascade for Geometries I and II of the triple correlations. The angular distribution data for the

FIG. 40 The triple angular correlations for the $r \rightarrow 2.73 \rightarrow 1.01$ cascade at the 809 KeV resonance. The unhatched rectangular blocks show the position of the gating energy windows of the detector fixed at the 90^{o} direction. The distributions are

Geometry I $W = P_o - (0.10 \pm 0.008)P_2 - (0.13 \pm 0.008)P_4$

Geometry II $W = P_o - (0.002 \pm 0.03)P_2 - (0.01 \pm 0.03)P_4$.

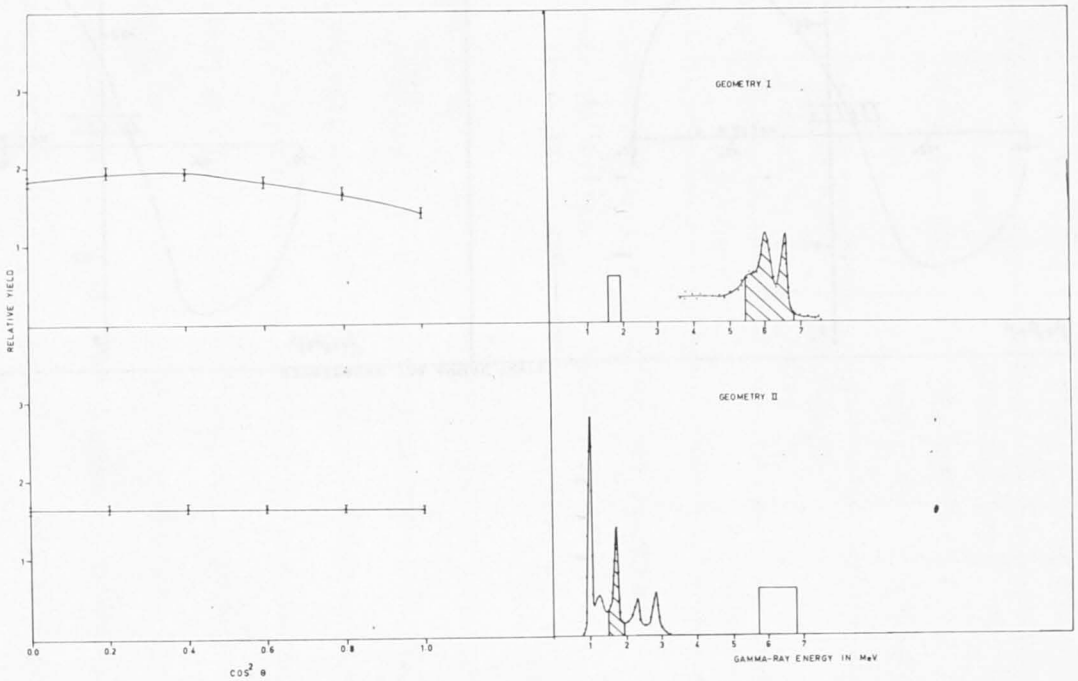
GEOMETRY I
GEOMETRY II
RELATIVE YIELD
$\cos^2\theta$
GAMMA-RAY ENERGY IN MeV

FIRST GAMMA RAY UNOBSERVED

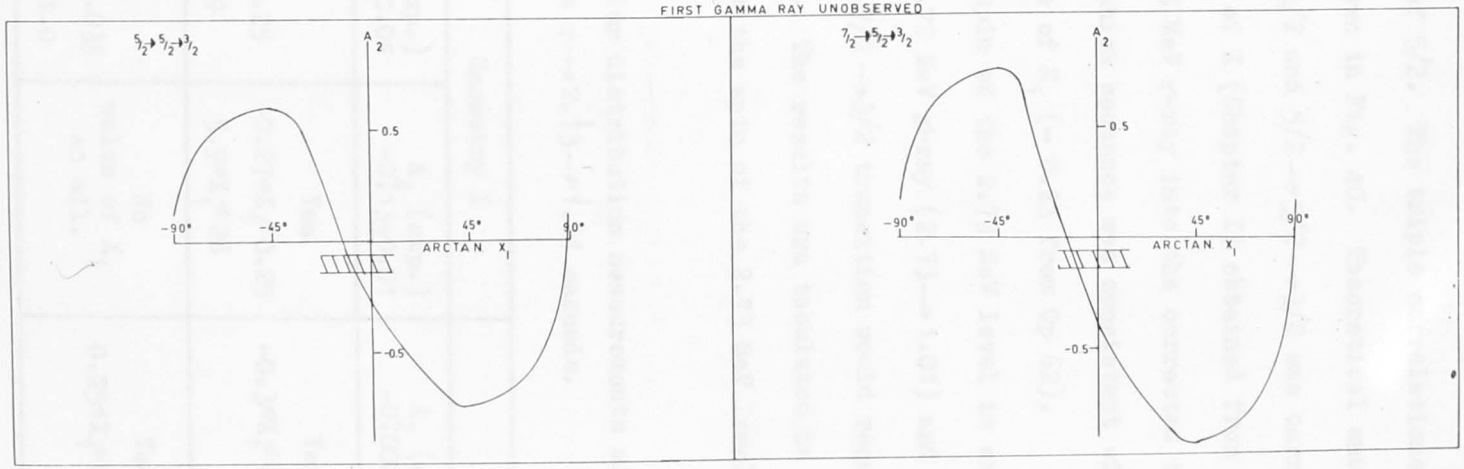

r $\rightarrow$ 2.73 MeV transition of (Op 62) was accepted together with the determined resonance spin of 5/2. The triple correlations for Geometries I and II are shown in Fig. 40. Theoretical analysis of the sequences 5/2 $\rightarrow$ 3/2 $\rightarrow$ 3/2 and 5/2 $\rightarrow$ 5/2 $\rightarrow$ 3/2 was carried out by substituting the values of X (Chapter I) obtained from the angular correlation of the r $\rightarrow$ 2.73 MeV γ-ray into the corrected theoretical correlations to determine which sequence was consistent with the previously determined value of X_1 (- 0.23 from Op 62).

A value of $\frac{1}{2}$ for the spin of the 2.73 MeV level is excluded by the anisotropy of the 1.72 MeV γ-ray (2.73 $\rightarrow$ 1.01) and 7/2 was considered unlikely as the 7/2 $\rightarrow$ 3/2 transition would require a large quadrupole component. The results are tabulated in Table 5. The conclusion is made that the spin of the 2.73 MeV level of Al^{27} is indeed 5/2.

Table 5 Analysis of Angular distribution measurements at the 809 KeV resonance for the r $\rightarrow$ 2.73 $\rightarrow$ 1.01 cascade.

Spin Sequence	Geometry I		Geometry II	
	A_2 (exp.) -0.10 ± 0.01	A_4 (exp.) -0.13 ± 0.01	A_2 (exp.) -0.002 ± 0.03	A_4 (exp.) -0.015 ± 0.03
5/2 $\rightarrow$ 5/2 $\rightarrow$ 3/2	Yes $-0.2 \leq X_1 \leq +0.25$ $+5.7 \leq X_1 \leq +29$	Yes $-0.27 \leq X_1 \leq 0.25$ $5.9 \leq X_1 \leq 28$	Yes $-0.3 \leq X_1 \leq 0.84$	Yes $-0.1 \leq X_1 \leq -0.36$
5/2 $\rightarrow$ 3/2 $\rightarrow$ 3/2	Yes $-0.25 \leq X_1 \leq 0.035$ $-1.2 \leq X_1 \leq -1.0$	No value of X_1 at all.	Yes $0.25 \leq X_1 \leq 0.30$	No theoretical P_4 term.

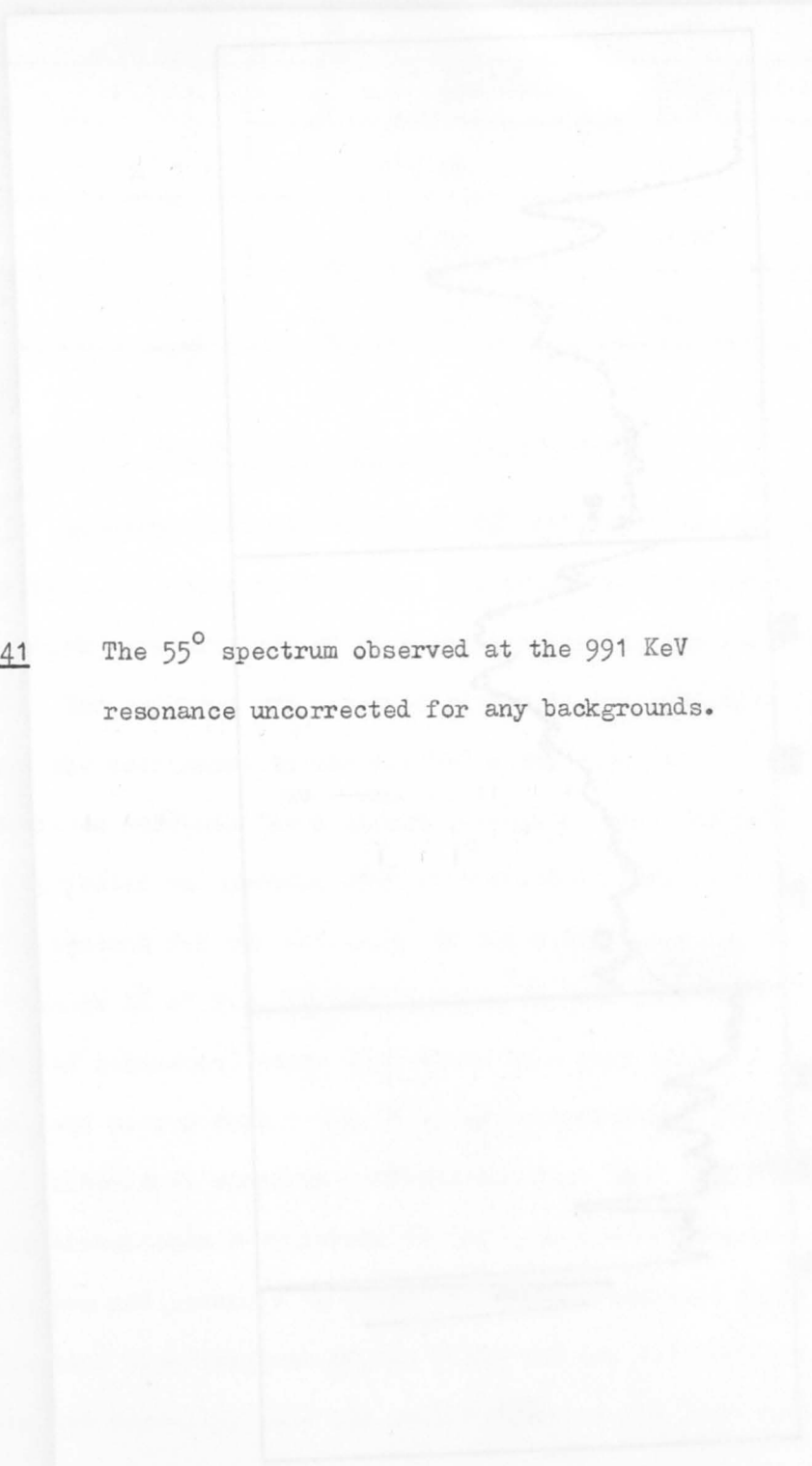

FIG. 41 The 55° spectrum observed at the 991 KeV resonance uncorrected for any backgrounds.

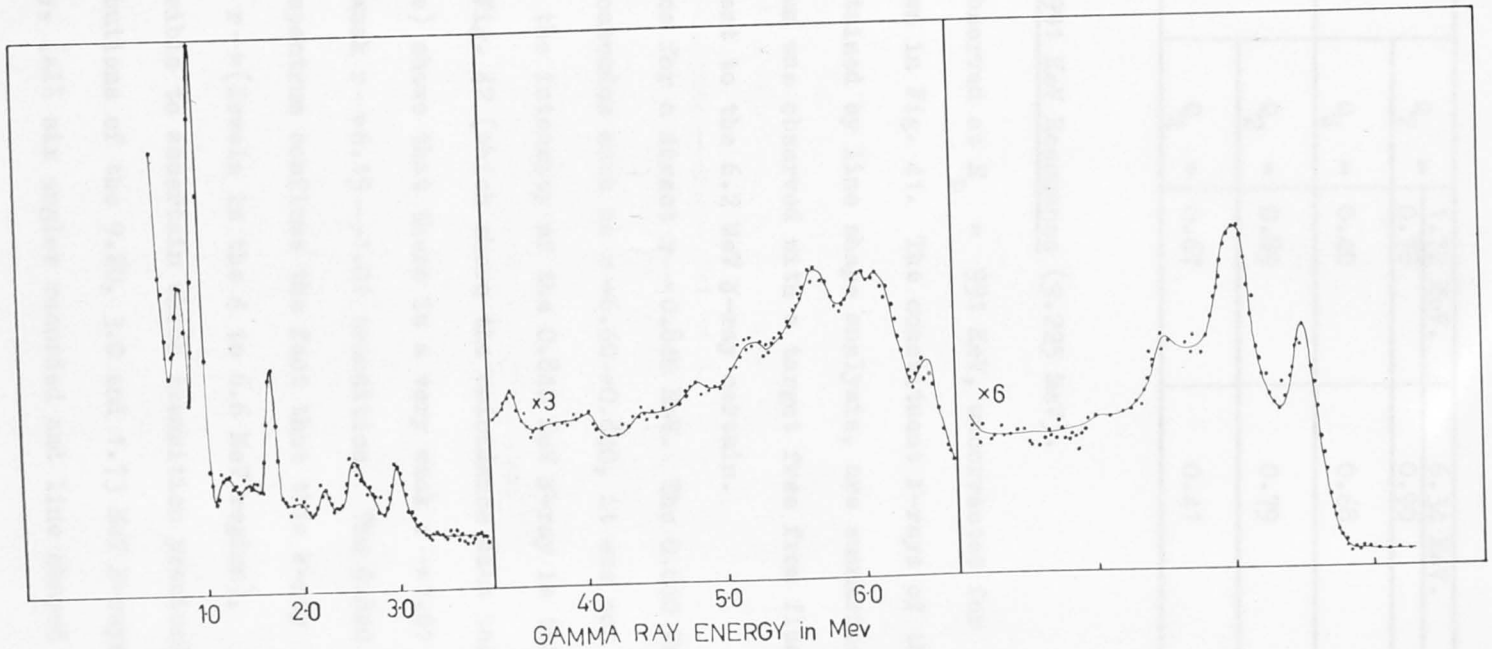
×3
×6
1·0
2·0
3·0
4·0
5·0
6·0
GAMMA RAY ENERGY in Mev

The geometrical correction factors were

		1.72 MeV.	6.34 MeV.
Geometry I	Q_2 =	0.78	0.90
	Q_4 =	0.40	0.68
Geometry I	Q_2 =	0.89	0.79
	Q_4 =	0.67	0.41

(iii) The 991 KeV Resonance (9.225 MeV).

The 55° spectrum observed at E_p = 991 KeV, uncorrected for any backgrounds, is shown in Fig. 41. The constituent γ-rays of the spectrum, which were obtained by line shape analysis, are summarised in Table 6. The spectrum was observed with a target free from fluorine, which makes the assignment to the 6.2 MeV γ-ray certain.

There is no evidence for a direct r$\longrightarrow$0.840 MeV. The 0.840 MeV γ-ray is attributed to cascades such as r$\rightarrow$6.60$\rightarrow$0.840, it was not possible to account for the intensity of the 0.840 MeV γ-ray in this way however. Window II of Fig. 42 (which shows the coicidence data taken at the 991 KeV resonance) shows that there is a very weak r$\longrightarrow$1.01 MeV transition, and also a weak r$\longrightarrow$6.15$\longrightarrow$1.01 transition. The 0.840 MeV (Window I) coincidence spectrum confirms the fact that this γ-ray arises from transitions r$\longrightarrow$(levels in the 4 to 6.6 MeV region), although it was not possible to ascertain which transition precisely.

The angular distributions of the 9.20, 3.0 and 1.73 MeV γ-rays were determined normally, (all six angles recorded and line shaped

FIG. 42 The gamma-ray spectra observed at the 991 KeV resonance in coincidence with the energy intervals indicated. All spectra collected for 10^6 monitor counts.

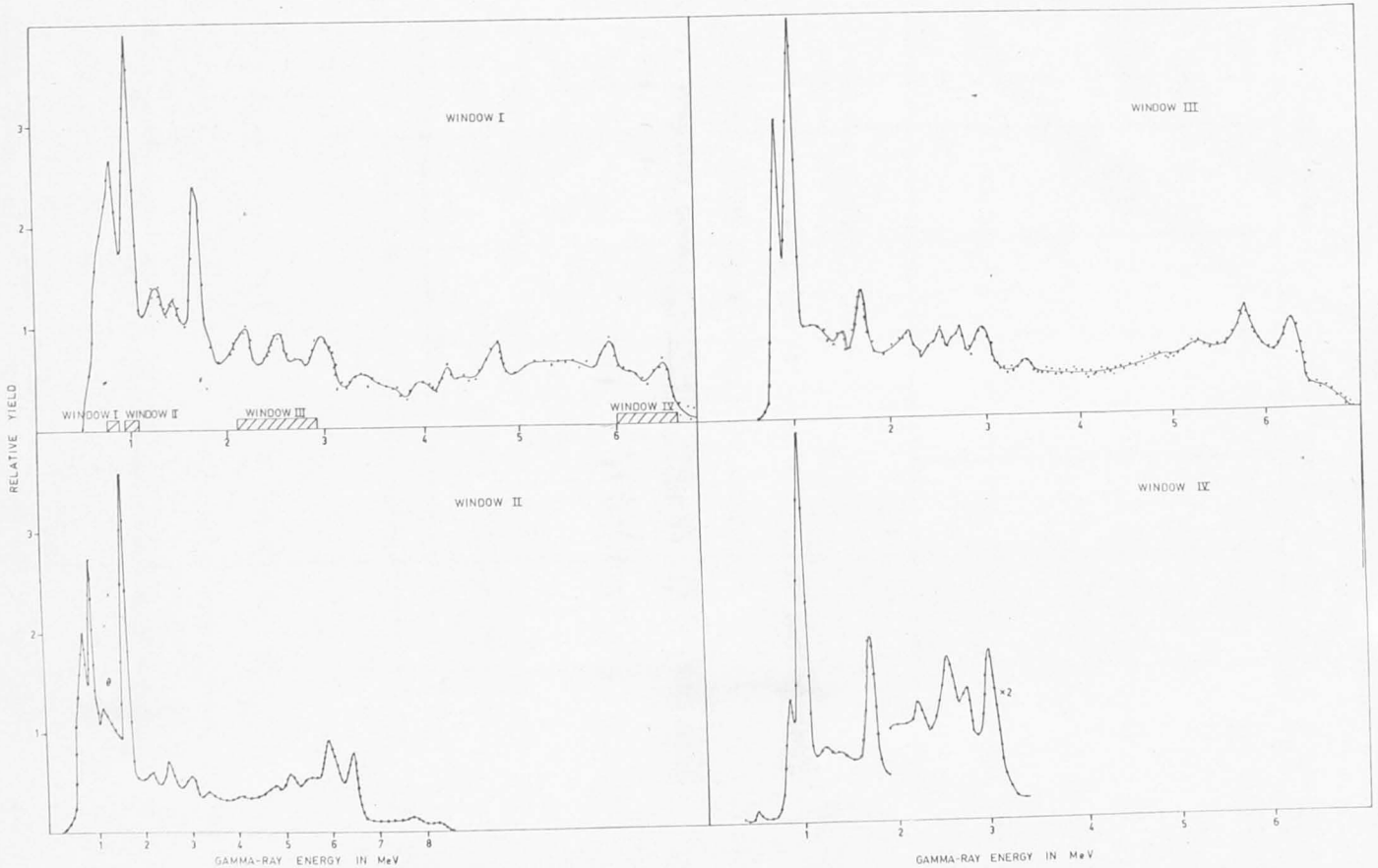
WINDOW I
WINDOW III
WINDOW II
WINDOW IV
WINDOW I WINDOW II
WINDOW III
WINDOW IV
RELATIVE YIELD
GAMMA-RAY ENERGY IN MeV
GAMMA-RAY ENERGY IN MeV
×2

FIG. 42a The 991 KeV resonance decay scheme.

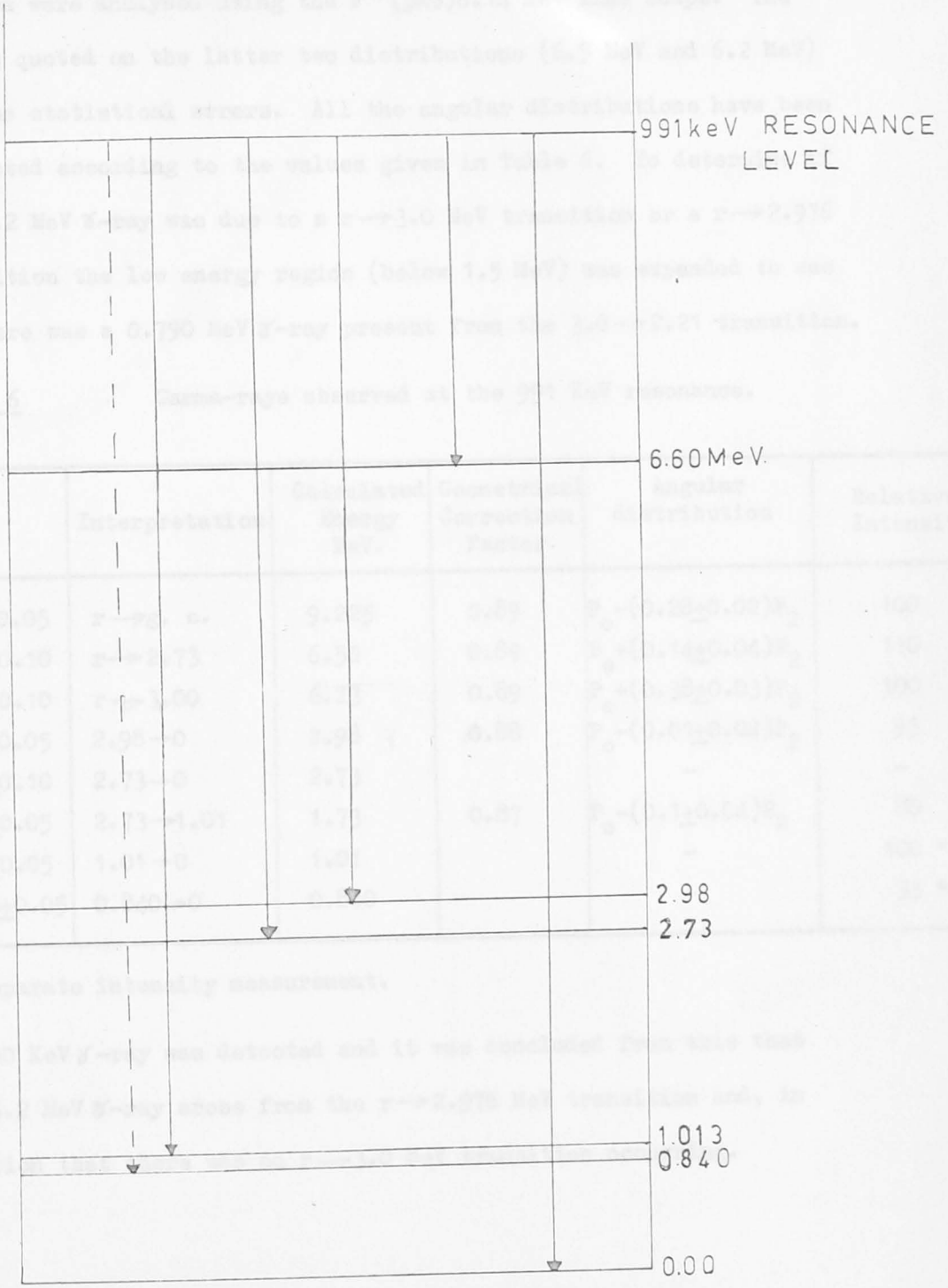
991keV RESONANCE LEVEL
6.60MeV.
2.98
2.73
1.013
0.840
0.00

analysed) but for the 6.5 MeV and 6.2 MeV γ-rays only the 0° and 90° spectra were analysed using the $F^{19}(p\alpha\gamma)6.14$ MeV line shape. The errors quoted on the latter two distributions (6.5 MeV and 6.2 MeV) are the statistical errors. All the angular distributions have been corrected according to the values given in Table 6. To determine if the 6.2 MeV γ-ray was due to a r $\rightarrow$ 3.0 MeV transition or a r $\rightarrow$ 2.976 transition the low energy region (below 1.5 MeV) was expanded to see if there was a 0.790 MeV γ-ray present from the 3.0 $\rightarrow$ 2.21 transition.

Table 6 Gamma-rays observed at the 991 KeV resonance.

E_γ MeV	Interpretation	Calculated Energy MeV.	Geometrical Correction Factor	Angular distribution	Relative Intensity
9.20±0.05	r $\rightarrow$ g. s.	9.225	0.89	$P_o-(0.28\pm0.02)P_2$	100
6.50±0.10	r $\rightarrow$ 2.73	6.50	0.89	$P_o+(0.14\pm0.04)P_2$	110
6.2 ±0.10	r $\rightarrow$ 3.00	6.23	0.89	$P_o+(0.38\pm0.03)P_2$	100
3.0 ±0.05	2.98 $\rightarrow$ 0	2.98	0.88	$P_o-(0.01\pm0.04)P_2$	95
2.73±0.10	2.73 $\rightarrow$ 0	2.73		-	-
1.75±0.05	2.73 $\rightarrow$ 1.01	1.73	0.87	$P_o-(0.1\pm0.04)P_2$	80
1.01±0.05	1.01 $\rightarrow$ 0	1.01		-	100 *
0.840±0.05	0.840 $\rightarrow$ 0	0.840		-	33 *

* Separate intensity measurement.

No 790 KeV γ-ray was detected and it was concluded from this that the 6.2 MeV γ-ray arose from the r $\rightarrow$ 2.976 MeV transition and, in addition that there was no r $\rightarrow$ 3.0 MeV transition occurring.

FIG. 43 The gamma-ray spectra obtained at the 1015 KeV resonance. The data were collected at 90° to the proton beam as the gamma-rays proved to be isotropic.

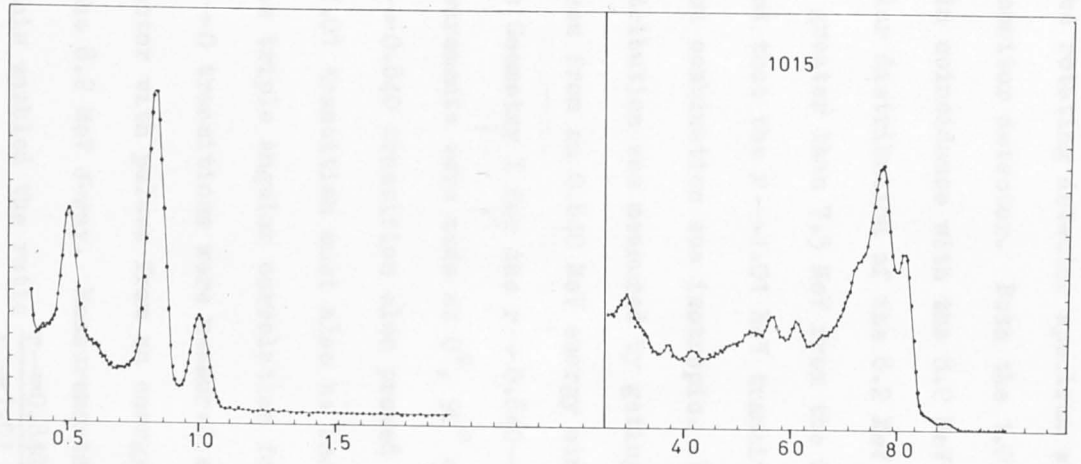
1015
0.5
1.0
1.5
4.0
6.0
8.0
GAMMA RAY ENERY IN MeV.

(iv) The 1015 KeV Resonance (9.250 MeV)

The spectrum obtained at the 1015 KeV resonance is relatively simple. (Fig. 43). The predominant transitions, by at least an order of magnitude, are to the 0.840 MeV and 1.01 MeV levels of Al^{27}. This was determined by gating the rotating detector spectrum with the 8.2 MeV γ-ray window from the monitor detector. Both the 1.01 MeV and the 0.840 MeV γ-rays were in coincidence with the 8.2 MeV γ-ray as required. A complete angular distribution of the 8.2 MeV γ-ray, obtained by feeding pulses greater than 7.5 MeV from the rotating detector to a scaler, showed that the $r \rightarrow 1.01$ MeV transition and the $r \rightarrow 0.840$ MeV transition combination was isotropic. The $r \rightarrow 0.840$ MeV transition angular distribution was measured by gating the rotating detector spectrum with pulses from an 0.840 MeV energy window from the monitor detector. (This is Geometry I for the $r \rightarrow 0.840 \rightarrow 0$ triple angular correlation). Measurements were made at 0°, 90° and 45° to the beam direction. The $r \rightarrow 0.840$ transition also proved to be isotropic. Hence the $r \rightarrow 1.01$ transition must also be isotropic.

The geometry II for the triple angular correlation for the $r \rightarrow 1.01 \rightarrow 0$ and $r \rightarrow 0.840 \rightarrow 0$ transitions were measured simultaneously by gating the rotating detector with pulses from an energy window in the monitor detector over the 8.2 MeV γ-ray. Measurements were carried out at all six angles and this enabled the ratio $\frac{r \rightarrow 0.840}{r \rightarrow 1.01}$ to be determined as $\frac{74}{26}$. (After allowance for efficiency and peak to total ratio variations had been made.)

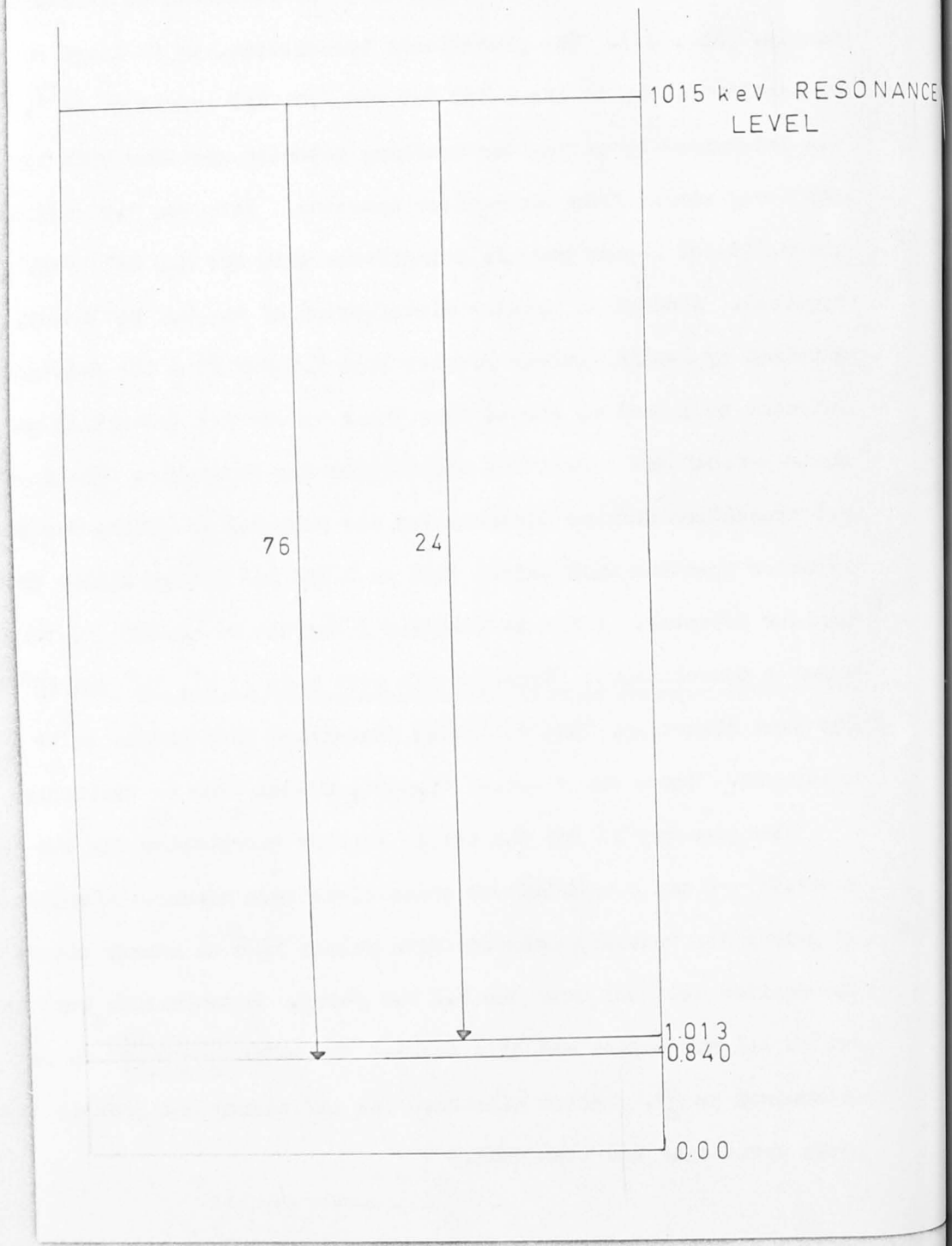
1015 keV RESONANCE
LEVEL
76
24
1.013
0.840
0.00

FIG. 43a The 1015 KeV decay scheme. Only the two predominant transitions are shown.

The γ-rays in coincidence with 1,01 MeV show that there are possibly some very weak transitions to levels in Al^{27} from the 5 - 6 MeV region.

The γ-ray at 6.14 MeV is attributed to $F^{19}(p,\alpha\gamma)$.

The results are summarised in table 7.

Table 7 Gamma-rays observed at the 1015 KeV resonance.

γ-ray Energy MeV	Interpretation	Calculated Energy MeV	Angular Distribution	Relative Intensity
8.3±0.10	r → 1.01 r → 0.840	8.24 8.41	Isotropic Isotropic	100
6.14	F^{19}	-	-	-
1.01±0.05	1.01 → 0	1.01		24
0.840±0.02	0.840 → 0	0.840		76

The 1015 KeV resonance does not decay, in any appreciable intensity, to any low lying Al^{27} levels and is therefore of no great interest for the present investigations.

(v) The 1056 KeV Resonance (9.289 MeV)

The spectrum obtained is shown in Fig. 44. Present in the spectrum is an intense r→g.s transition together with transitions to the 0.840 MeV, 1.01 MeV and 2.73 MeV levels which are much weaker in intensity. A large F^{19} background was observed.

The coincident data are mildly interesting. (Fig. 44a). Window I

FIG. 44 The spectrum obtained at 55° at the 1056 KeV resonance, corrected for room background and dead time of the analyser,

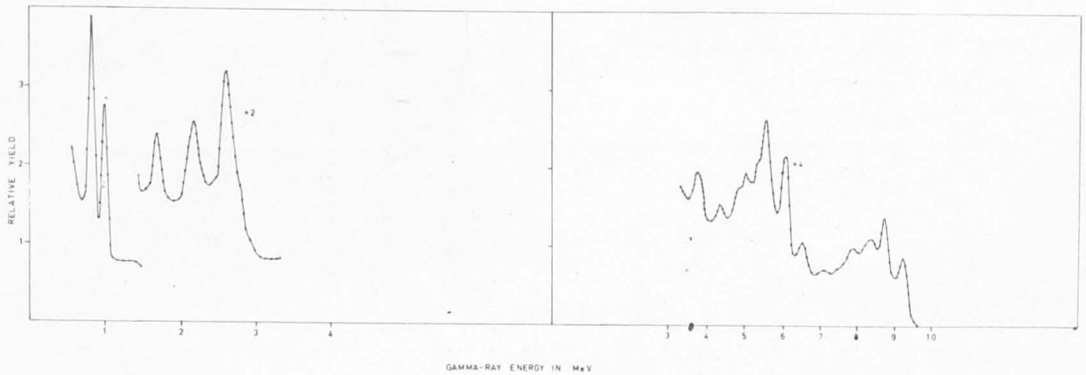
RELATIVE YIELD
1
2
3
1
2
3
4
3
4
5
6
7
8
9
10
GAMMA-RAY ENERGY IN MeV

FIG. 44a The spectra obtained, for 10^6 monitor counts, in coincidence with the various energy intervals indicated by the hatched areas at 1056 KeV.

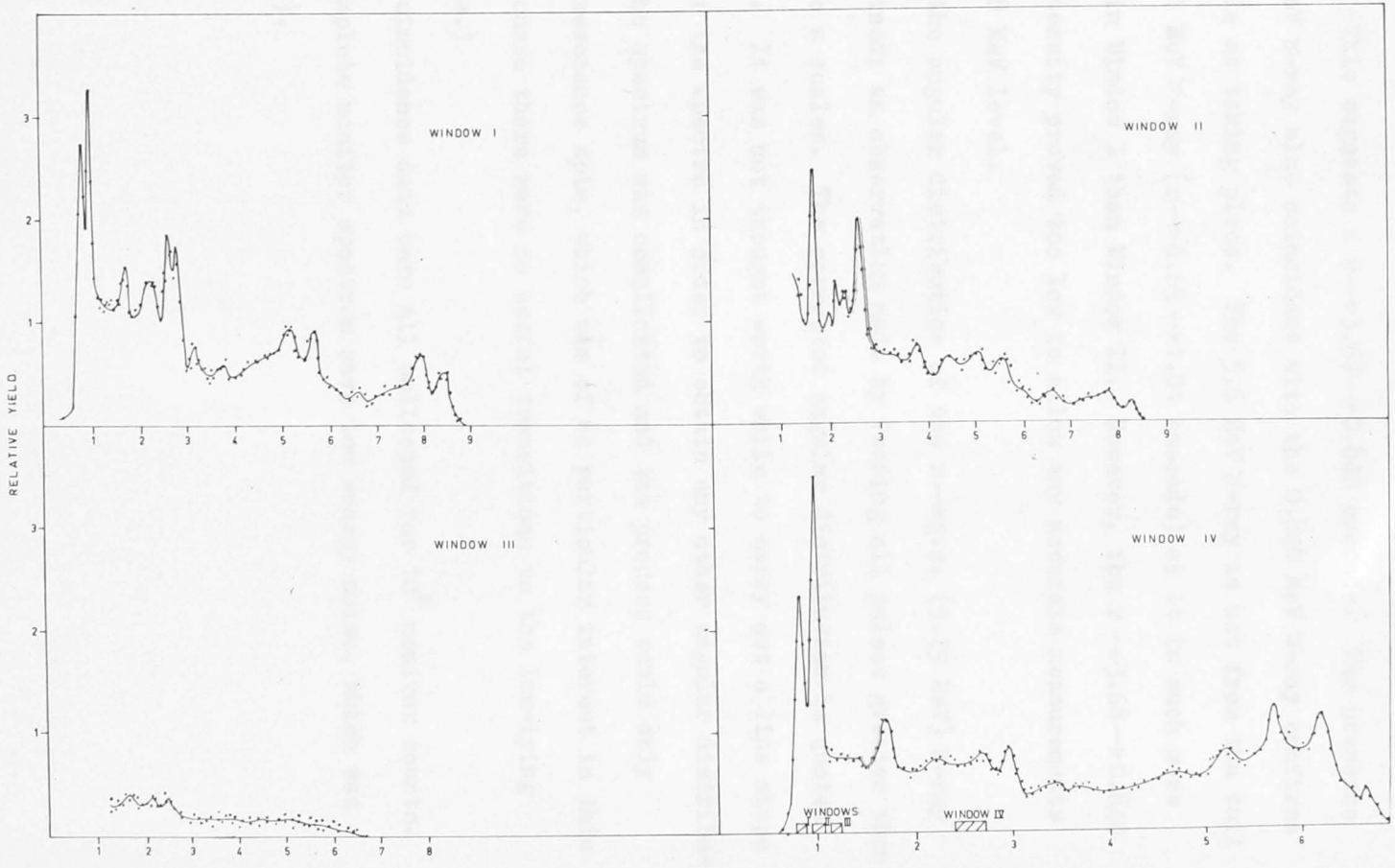
WINDOW I
WINDOW II
WINDOW III
WINDOW IV
WINDOWS
WINDOW IV
RELATIVE YIELD
GAMMA-RAY ENERGY IN MeV

(0.840 MeV) shows that a 2.8 MeV γ-ray is coincident with the 0.840 MeV γ-ray. This suggests a $r \rightarrow 3.68 \rightarrow 0.840$ cascade. The presence of a 5.6 MeV γ-ray also coincident with the 0.840 MeV γ-ray confirms this cascade as taking place. The 5.6 MeV γ-ray is not from the tail of the 1.01 MeV γ-ray ($r \rightarrow 6.65 \rightarrow 1.01$ cascade) as it is much more prominent in Window I than Window II. However, the $r \rightarrow 3.68 \rightarrow 0.840$ cascade intensity proved too low to allow any accurate measurements on the 3.68 MeV level.

Only the angular distribution of the $r \rightarrow$ g.s. (9.29 MeV) γ-ray was determined; an observation made by feeding all pulses greater than 8.75 MeV to a scaler. The corrected angular distribution is quoted in table 8. It was not thought worth while to carry out a line shape analysis of the spectra in order to obtain any other angular distributions as the spectrum was complicated and the process would only yield the resonance spin, which was of no particular interest in this case. (Because there were no useful transitions to the low-lying Al^{27} levels.)

The coincidence data were all collected for 10^6 monitor counts. (In the complete monitor spectrum save low energy noise, which was biased out).

FIG. 44b The 1056 KeV resonance decay scheme.

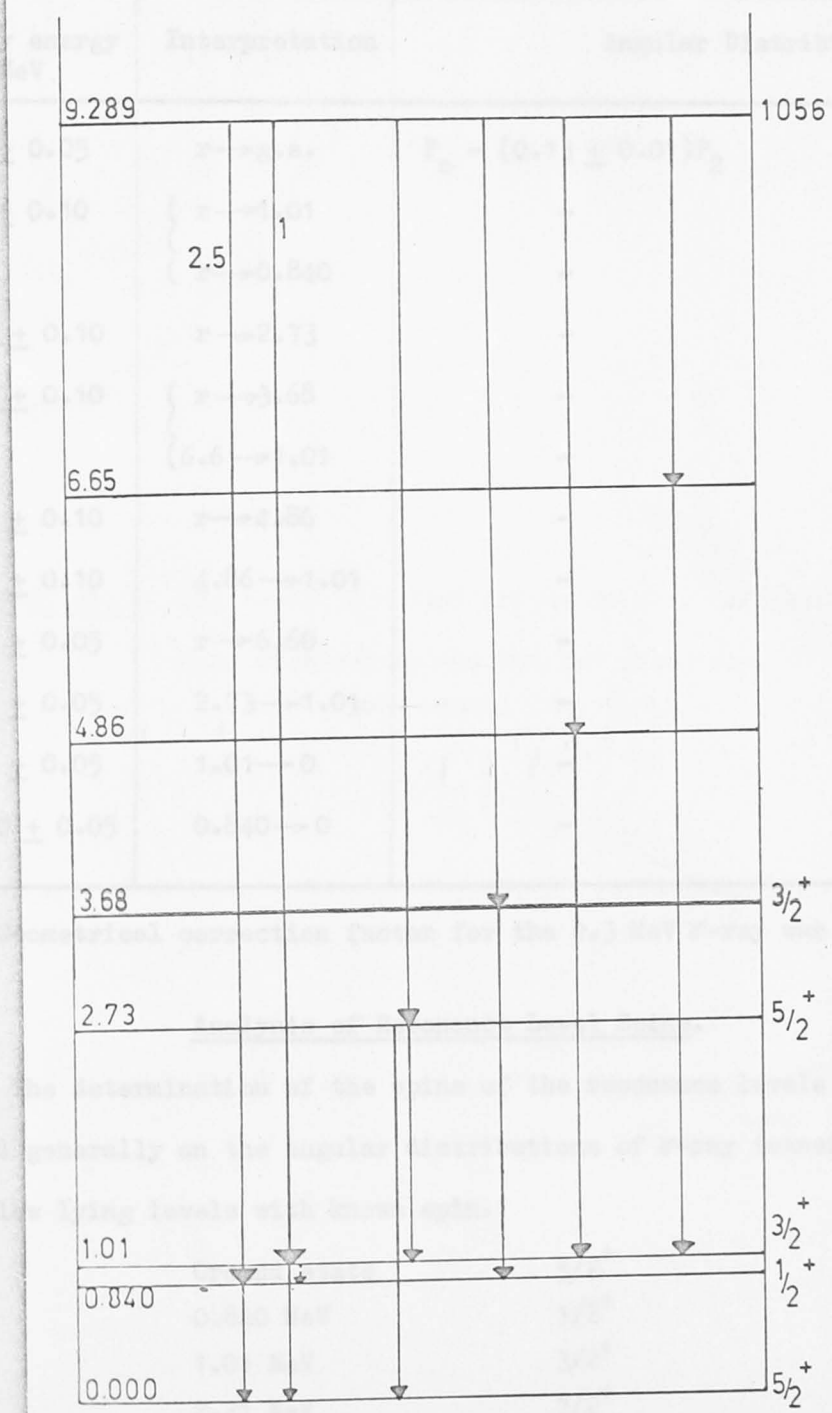
9.289
1056 keV RESONANCE LEVEL.
2.5
1
6.65
4.86
3.68
3/2+
2.73
5/2+
3/2+
1.01
1/2+
0.840
0.000
5/2+

Table 8 Gamma-rays observed at 1056 KeV.

γ-ray energy MeV	Interpretation	Angular Distribution
9.3 ± 0.05	r → g.s.	$P_o - (0.13 \pm 0.01)P_2$
8.4 ± 0.10	r → 1.01	-
	r → 0.840	-
6.60 ± 0.10	r → 2.73	-
5.65 ± 0.10	r → 3.68	-
	6.6 → 1.01	-
4.43 ± 0.10	r → 4.86	-
3.80 ± 0.10	4.86 → 1.01	-
2.65 ± 0.05	r → 6.60	-
1.7 ± 0.05	2.73 → 1.01	-
1.01 ± 0.05	1.01 → 0	-
0.840 ± 0.05	0.840 → 0	-

The Geometrical correction factor for the 9.3 MeV γ-ray was 0.89.

4.4 Analysis of Resonance Level Spins.

The determination of the spins of the resonance levels ($=I_r$) is based generally on the angular distributions of γ-ray transitions to the low lying levels with known spin.

Ground state	$5/2^+$
0.840 MeV	$1/2^+$
1.01 MeV	$3/2^+$
2.21 MeV	$7/2^+$
2.73 MeV	$5/2^+$.

FIG. 46a The r $\rightarrow$ 2.73 $\rightarrow$ 1.01 triple angular correlation data observed at the 991 KeV resonance.

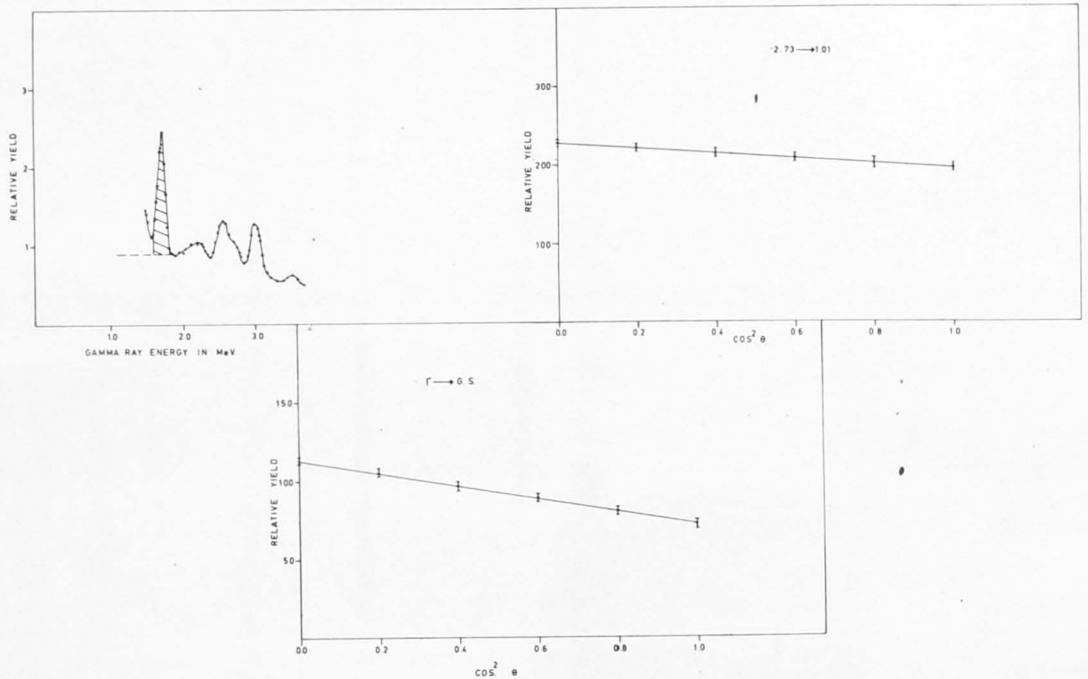
RELATIVE YIELD
GAMMA RAY ENERGY IN MeV
2.73 → 1.01
RELATIVE YIELD
cos² θ
Γ → 0.5
RELATIVE YIELD
cos² θ

FIG. 46 The angular distribution data taken at the 991 KeV resonance concerning the spin of the resonance level. (The r $\rightarrow$ 2.73 gamma-ray distribution is omitted as only a $0^{\circ}/90^{\circ}$ ratio was obtained in this case.)

As pointed out in Chapter I, throughout the discussion the parameter X is the E2/M1 mixing ratio of the transition from the resonance level to a low lying level and X_1 is the mixing ratio of a subsequent γ-ray.

The 721 KeV Resonance.

The spin is likely to be 5/2 or 3/2 since there are strong transitions to the 3.68 MeV level (shown to be I = 3/2 later). The required E2/M1 mixing ratios are within plausible limits for either of the resonance level spins (Fig. 45a).

$I_r = 3/2$ $\quad X = +0.47 \longrightarrow 0.53$ $\quad$ or $+5.4 \longrightarrow +5.8$

$I_r = 5/2$ $\quad X = 0 \longrightarrow -0.09$ $\quad$ or $+5.6 \longrightarrow 5.8$.

A spin of I = $\frac{1}{2}$ for the resonance level is excluded by the anisotropy of the 5.38 MeV γ-ray ($r \longrightarrow 3.68$). Fig. 45 shows the angular distribution data taken at 721 KeV.

The 991 KeV Resonance.

Analysis of the angular distribution data is summarised in Table 9 and Table 9a. Possible compound state spins of 3/2, 5/2 and 7/2 were considered, since the presence of relatively strong transitions to the ground state ($5/2^+$) and the 2.73 MeV ($5/2^+$) level indicates that spins greater than 7/2 are unlikely.

A unique assignment is not possible from the angular distributions alone because all the three above values for the resonance spin give acceptable E2/M1 mixing ratios.

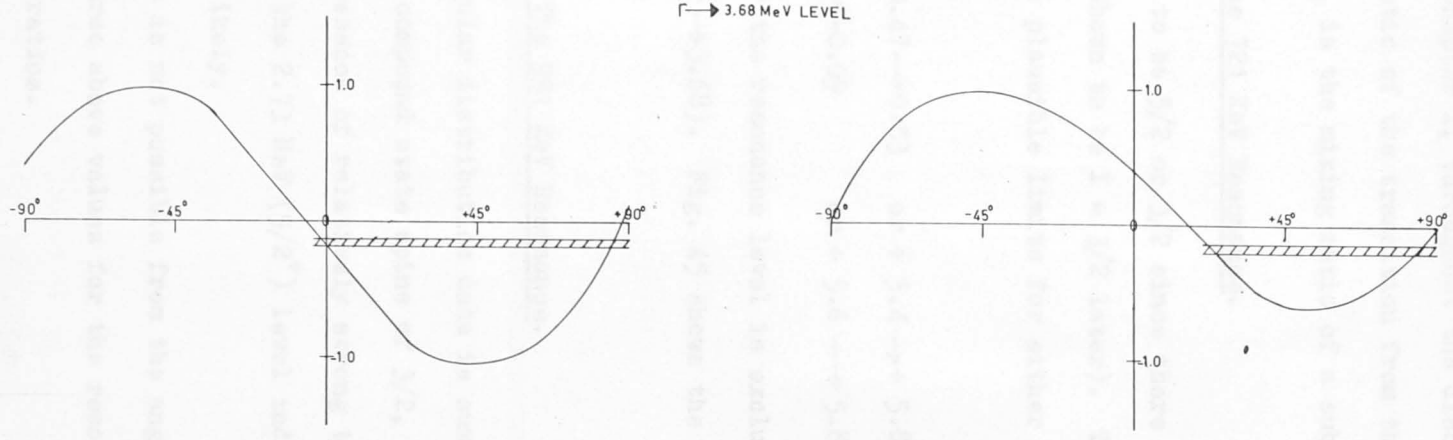
3.68 MeV LEVEL
1.0
-90°
-45°
0
+45°
+90°
-1.0
1.0
-90°
-45°
0
+45°
+90°
-1.0

FIG. 45a Analysis of the r $\rightarrow$3.68 angular distribution data. Sequence 5/2 $\rightarrow$3/2 is on the left and 3/2 $\rightarrow$3/2 on the right.

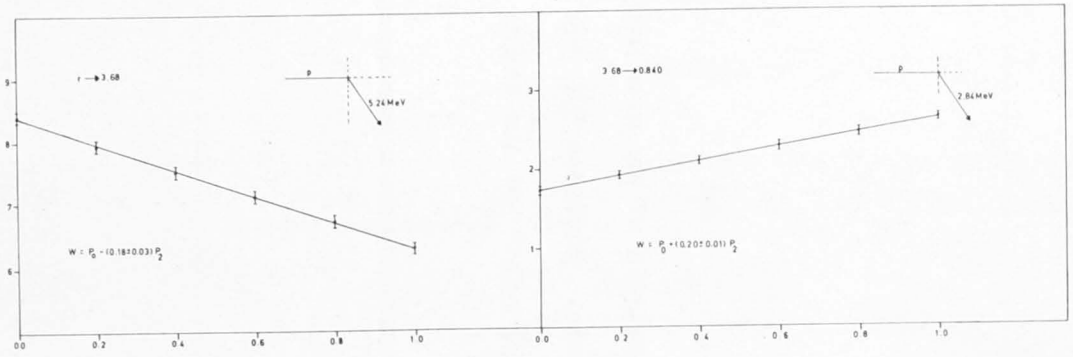
r → 3.68
p
5.24MeV
W = P0 + (0.18±0.03) P2
3.68 → 0.840
P
2.84MeV
W = P0 + (0.20±0.01) P2
9
8
7
6
3
2
1
0.0
0.2
0.4
0.6
0.8
1.0
cos² θ

FIG. 45 The angular distribution data taken at the 721 KeV resonance for the gamma-rays concerned with the resonance level spin. The distributions are uncorrected for geometrical effects.

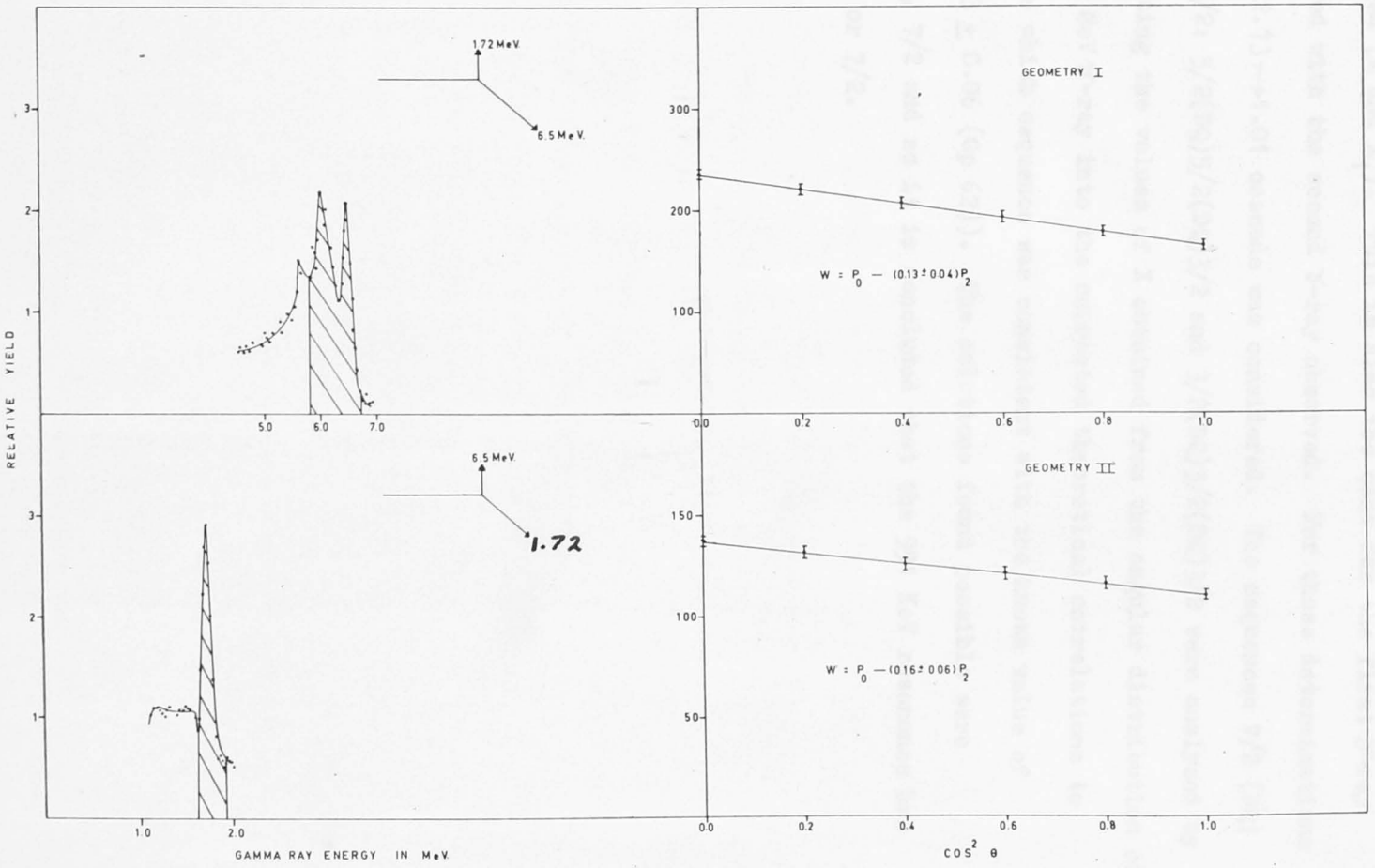
1.72 MeV.
6.5 MeV.
GEOMETRY I
W = P0 — (0.13 ± 0.04) P2
6.5 MeV.
1.72
GEOMETRY II
W = P0 — (0.16 ± 0.06) P2
RELATIVE YIELD
GAMMA RAY ENERGY IN MeV.
COS2 θ

Fig 46a.

For the analysis of triple angular correlation measurements, two mixing parameters, one for each of the cascade transitions, must be considered (X and X_1). This is also the case for the first γ-ray unobserved with the second γ-ray observed. For these determinations the r$\longrightarrow$2.73$\longrightarrow$1.01 cascade was considered. The sequences 7/2 (DQ) 5/2(DQ)3/2; 5/2(DQ)5/2(DQ)3/2 and 3/2(DQ)5/2(DQ)3/2 were analysed by substituting the values of X obtained from the angular distribution of the 6.50 MeV γ-ray into the corrected theoretical correlations to determine which sequence was consistent with the known value of X(-0.23 ± 0.06 (Op 62)). The solutions found possible were I_r = 5/2, 7/2 and so it is concluded that the 991 KeV resonance has spin 5/2 or 7/2.

FIG. 46b The 991 KeV resonance spin.

The transition r $\rightarrow$ 2.73 $\rightarrow$ 1.01 is analysed with the spin sequences $5/2 \rightarrow 5/2 \rightarrow 3/2$ and $7/2 \rightarrow 5/2 \rightarrow 3/2$. The top correlation shows the transition to the 2.73 MeV level. The bottom two show the triple correlations for Geometries I and II. The theoretical predictions are shown as a solid line, the measurements as hatched areas.

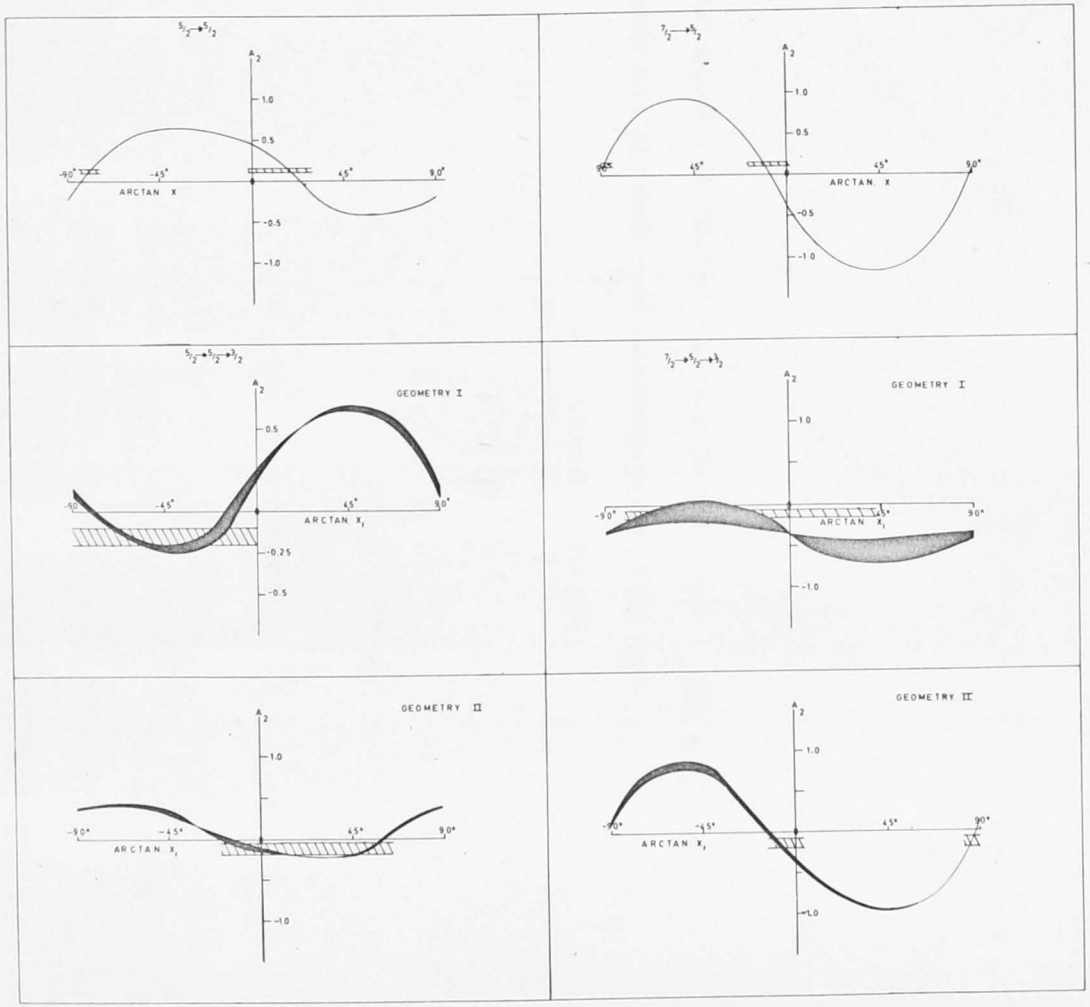
5/2→5/2
A2
1.0
0.5
-90°
-45°
45°
90°
ARCTAN X
-0.5
-1.0
7/2→5/2
5/2→5/2→3/2
GEOMETRY I
ARCTAN X1
-0.25
7/2→5/2→3/2
GEOMETRY II

FIG. 46c Analysis of the 2.73→1.01 transition at the 991 KeV resonance. Measurements are shown as hatched areas.

FIRST GAMMA RAY UNOBSERVED

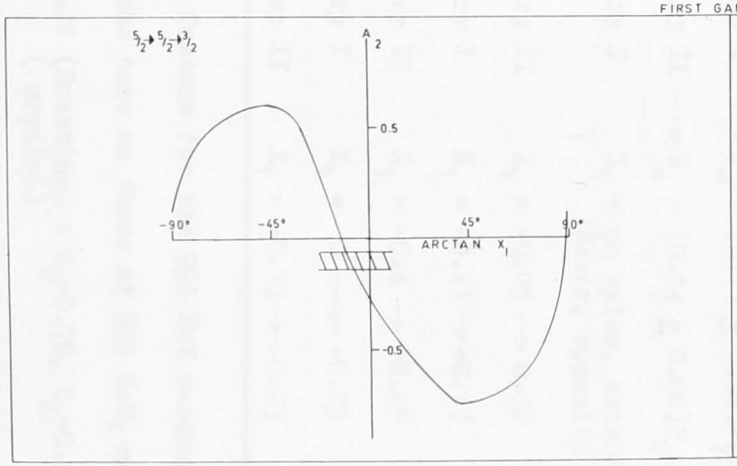

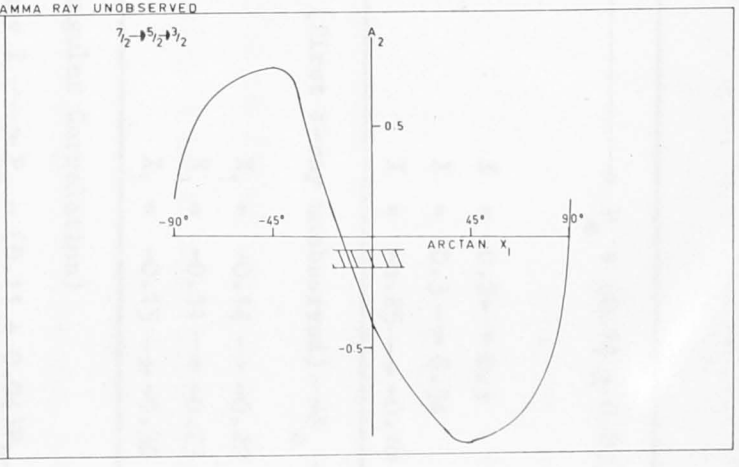

Table 9. Analysis of the r $\rightarrow$ 2.73 $\rightarrow$ 1.01 cascade at the 991 KeV resonance.

r $\rightarrow$ 2.73 MeV level $\longrightarrow$	$P_o + (0.14 \pm 0.05)P_2$.	
Spin sequence		
3/2 $\rightarrow$ 5/2	$X = 0.2 \rightarrow 0.3$	
5/2 $\rightarrow$ 5/2	$X = 0.3 \rightarrow 0.34$	
7/2 $\rightarrow$ 5/2	$X = -0.25 \rightarrow -0.18$	
r $\rightarrow$ 2.73 $\rightarrow$ 1.01 MeV level (first γ-ray unobserved) $\rightarrow$	$P_o - (0.1 \pm 0.04)P_2$.	
3/2 $\rightarrow$ 5/2 $\rightarrow$ 3/2	$X_1 = -0.14 \rightarrow -0.22$	
5/2 $\rightarrow$ 5/2 $\rightarrow$ 3/2	$X_1 = -0.11 \rightarrow -0.23$	
7/2 $\rightarrow$ 5/2 $\rightarrow$ 3/2	$X_1 = -0.15 \rightarrow -0.30$	
r $\rightarrow$ 2.73 $\rightarrow$ 1.01 (Triple angular Correlation)		
	Geometry I $\longrightarrow$	$P_o - (0.11 \pm 0.04)P_2$.
	Geometry II $\longrightarrow$	$P_o - (0.14 \pm 0.06)P_2$.
3/2 $\rightarrow$ 5/2 $\rightarrow$ 3/2	Geometry I	X_1 = no value, outside experimental error, opposite sign a_2 needed.
	Geometry II	$X_1 = -0.05 \rightarrow 0.09$
5/2 $\rightarrow$ 5/2 $\rightarrow$ 3/2	Geometry I	$X_1 = -0.21 \rightarrow +0.17$
	Geometry II	$X_1 = -0.4 \rightarrow +0.25$
7/2 $\rightarrow$ 5/2 $\rightarrow$ 3/2	Geometry I	$X_1 = 0 \longrightarrow -0.29$
	Geometry II	$X_1 = -0.13 \rightarrow -0.23$

The Geometrical correction factors for the 991 KeV resonance triple angular correlations were the same as those at 809 KeV, namely:

Geometry I Q_2=0.845, Q_4=0.41 (Rotating crystal) : Q_2=0.78, Q_4=0.40 (Monitor)

Geometry II Q_2=0.84 Q_4=0.54 (Rotating crystal) : Q_2=0.785, Q_4=0.41 (Monitor).

Table 9a. Analysis of the r⟶g.s transition at the 991 KeV resonance.

Spin sequence	$a_2 = -0.28 \pm 0.02$
3/2 ⟶ 5/2	X = − 0.09 ⟶ − 0.12
5/2 ⟶ 5/2	X = + 0.52 ⟶ + 0.63
7/2 ⟶ 5/2	X = − 0.04 ⟶ − 0.07

The 1015 KeV Resonance.

The angular distributions of the r⟶1.01 and r⟶0.840 transitions combined are isotropic. The r⟶0.840 transition is also isotropic individually. Hence the r⟶1.01 and r⟶0.840 transitions are not isotropic by virtue of opposite angular distributions cancelling out and it can be concluded that the r⟶1.01 transition is also isotropic. On this evidence the 1015 KeV resonance is assigned a spin of $\frac{1}{2}$.

The 1056 KeV Resonance.

Judging from the observed γ-ray intensities, the spin of the resonance level may be either 3/2, 5/2 or 7/2. Table 10 summarises the required mixings for the ground state transitions. A spin of $\frac{1}{2}$ is excluded for the resonance level as the ground state γ-ray is anisotropic. The resonance was of no particular interest and the value of the resonance spin was pursued no further. However, as there are transitions to the 0.84 MeV level ($I = \frac{1}{2}$) the resonance spin is probably either 3/2 or 5/2 with 7/2 being very unlikely.

Table 10 Analysis of the ground state transition at the 1056 KeV resonance.

Spin Sequence	A_2 (exp) -0.13 ± 0.01
$3/2 \longrightarrow 5/2$	$-0.05 \leq X \leq -0.04$
	$+9 \leq X \leq +10$
$5/2 \longrightarrow 5/2$	$+0.53 \leq X \leq +0.54$
	$-40 \leq X \leq -30$
$7/2 \longrightarrow 5/2$	$-0.14 \leq X \leq -0.10$
	$+20 \leq X \leq +30$

4.5 Spins of some low lying levels in Al^{27}.

The 3.68 MeV level

In the $Mg^{26}(p,\gamma)Al^{27}$ reaction the resonances below E_p = 1 MeV which decay, at least in part, via the 3.68 MeV level occur at E_p = 339 KeV, 661 KeV, 721 KeV, 839 KeV and 954 KeV. (Aj 62, Op 62). Of these resonances the 661 KeV and 839 KeV have spin $\frac{1}{2}$ (Op 62). This indicates a value of 3/2 or $\frac{1}{2}$ for the spin of the 3.68 MeV level since otherwise a strong quadrupole transition would be required from the two resonances. Van der Leun (Va 56) et al were the first to investigate the 3.68 MeV level by investigating the 339 KeV resonance. Using small detectors ($1\frac{5}{8}$" x 2" NaI(Tl)) they assigned a spin of 3/2 to the resonance level and a spin of $\frac{1}{2}$ to the 3.68 MeV level on the assumption of pure dipole radiation from the transition. However, the

results are suspect for two reasons, viz.

(i) The workers obtain spectra that are difficult to interpret accurately and the measured angular distribution for the r $\rightarrow$ 3.68 MeV transition could have been effected by the line shape of the intense γ-ray leading to the 3.0 MeV doublet levels.

(ii) Recently Van der Leun has retracted the 3/2 assignment to the 339 KeV resonance level, which presumably means that the other assignments are retracted at the same time (La 64).

In an investigation of the $Mg^{26}(d,n)Al^{27}$ reaction Lawergren and Furguson (La 64) reported that the 3.68 MeV level has a spin of $\frac{1}{2}$.

Whilst investigating the 954 KeV resonance of $Mg^{26}(p,\gamma)$ Ophel and Lawergren (Op 62) found that the 2.84 MeV from the 3.68 $\rightarrow$ 0.840 transition was probably anisotropic. This suggests that the 3.68 MeV level spin is <u>not</u> $\frac{1}{2}$.

The present work concerns observations on the 721 KeV resonance of the $Mg^{26}(p,\gamma)$ reaction as this has an intense r $\rightarrow$ 3.68 $\rightarrow$ 0.840 cascade. Unfortunately the resonance spin could not be determined uniquely, values of 5/2 or 3/2 seeming most probable.

The angular distribution of the 3.68 $\rightarrow$ 0.840 MeV transition was measured in two ways, viz.

(i) From the singles data in the rotating crystal by line shape analysis.

(ii) By observing the distribution of the 2.84 MeV γ-ray in coincidence with the 0.840 MeV γ-ray. This served as a check only on (i).

FIG. 47 The angular distribution data at the 721 KeV resonance concerning the 3.68 MeV level of Al^{27}.

NOTE. The anisotropy of the 3.68 0.840 (2.84 MeV) gamma-ray showing that the 3.68 MeV level cannot possibly be spin $\frac{1}{2}$.

All the distributions are geometrically corrected.

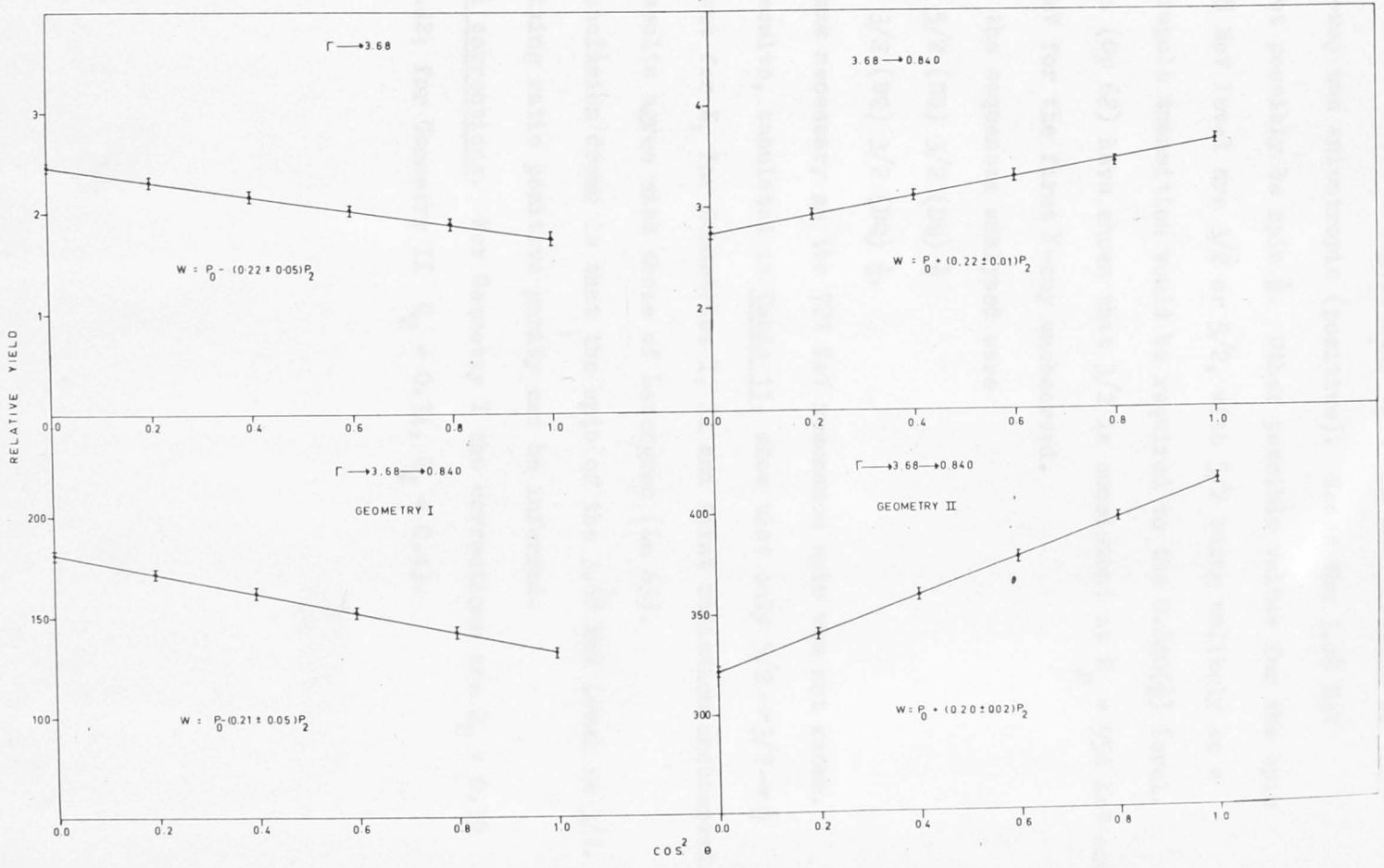
Γ ⟶ 3.68
W = P0 − (0·22 ± 0·05)P2
3.68 ⟶ 0.840
W = P0 + (0.22 ± 0.01)P2
Γ ⟶ 3.68 ⟶ 0.840
GEOMETRY I
W = P0 − (0.21 ± 0.05)P2
Γ ⟶ 3.68 ⟶ 0.840
GEOMETRY II
W = P0 + (0.20 ± 0.02)P2
RELATIVE YIELD
cos² θ

The results showed categorically that the distribution of the 2.84 MeV γ-ray was anisotropic (positive). Hence the 3.68 MeV level cannot possibly be spin $\frac{1}{2}$. Other possible values for the spin of the 3.68 MeV level are 3/2 or 5/2, with 5/2 being unlikely as a large quadrupole transition would be required to the 0.840($\frac{1}{2}$) level. In addition (Op 62) have shown that 3/2 is consistent at E_p = 954 KeV and E_p = 721 KeV for the first γ-ray unobserved.

Hence the sequences analysed were

5/2 (DQ) 3/2 (DQ) $\frac{1}{2}$

and 3/2 (DQ) 3/2 (DQ) $\frac{1}{2}$.

This was necessary as the 721 KeV resonance spin was not known.

The results, tabulated in Table 11, show that only $5/2 \rightarrow 3/2 \rightarrow \frac{1}{2}$ is consistent for X_1 for Geometries I, II and first radiation unobserved. Also the results agree with those of Lawergren (La 63).

The conclusion drawn is that the spin of the 3.68 MeV level is 3/2. From the mixing ratio positive parity can be inferred.

Geometrical corrections. For Geometry I the corrections are Q_2 = 0.79 and Q_4 = 0.42; for Geometry II Q_2 = 0.74, Q_4 = 0.43.

FIG. 47a. The 721 KeV resonance.

The transition r $\rightarrow$3.68$\rightarrow$0.840 with the spin sequence 5/2$\rightarrow$3/2$\rightarrow\frac{1}{2}$. The left hand diagram shows the direct transition to the 3.68 MeV level. The right hand shows the 3.68$\rightarrow$0.840 transition. Theoretical predictions are drawn as a solid line, measurements as hatched areas.

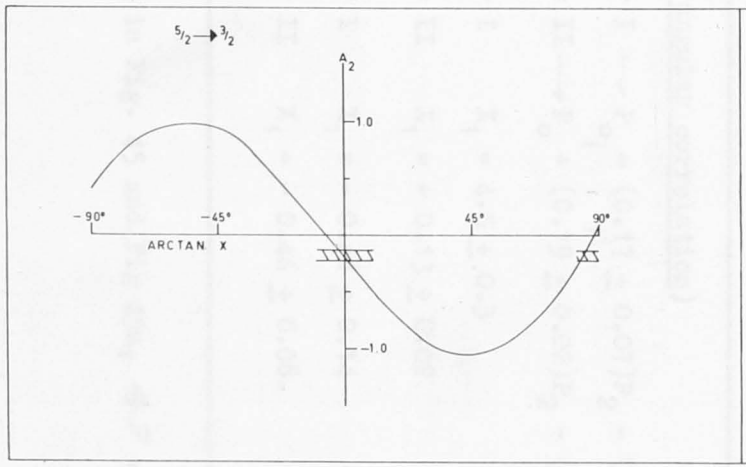
$^{5}/_{2} \rightarrow {}^{3}/_{2}$
A2
1.0
-1.0
-90°
-45°
45°
90°
ARCTAN X

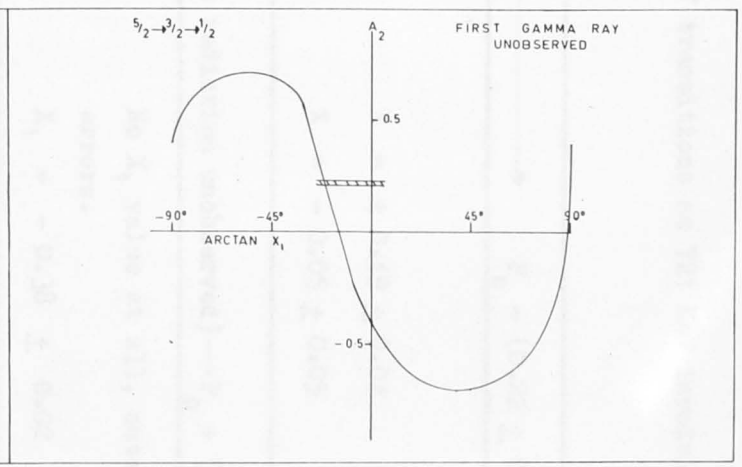
$^{5}/_{2} \rightarrow {}^{3}/_{2} \rightarrow {}^{1}/_{2}$
A2
FIRST GAMMA RAY
UNOBSERVED
0.5
-0.5
-90°
-45°
45°
90°
ARCTAN X_1

Table 11 Analysis of transitions at 721 KeV involving the 3.68 MeV level.

r $\longrightarrow$ 3.68 MeV level $\longrightarrow$		$P_o - (0.22 \pm 0.05)P_2$
Spin Sequence		
$3/2 \longrightarrow 3/2$		$X = + 0.49 \pm 0.04$
$5/2 \longrightarrow 3/2$		$X = - 0.05 \pm 0.05$
r $\longrightarrow$ 3.68 $\longrightarrow$ 0.840 (first radiation unobserved) $\longrightarrow$		$P_o + (0.22 \pm 0.01)P_2$
$3/2 \longrightarrow 3/2 \longrightarrow \frac{1}{2}$		No X_1 value at all, outside experimental errors.
$5/2 \longrightarrow 3/2 \longrightarrow \frac{1}{2}$		$X_1 = - 0.38 \pm 0.02$
r $\longrightarrow$ 3.68 $\longrightarrow$ 0.840 (Triple angular correlation)		
	Geometry I $\longrightarrow$	$P_o - (0.17 \pm 0.07)P_2 - (0.05 \pm 0.06)P_4$
	Geometry II $\longrightarrow$	$P_o + (0.19 \pm 0.02)P_2 - (0.04 \pm 0.02)P_4$
$3/2 \longrightarrow 3/2 \longrightarrow \frac{1}{2}$	Geometry I	$X_1 = 4.5 \pm 0.3$
	Geometry II	$X_1 = + 0.13 \pm 0.02$
$5/2 \longrightarrow 3/2 \longrightarrow \frac{1}{2}$	Geometry I	$X_1 = - 0.48 \pm 0.14$
	Geometry II	$X_1 = - 0.46 \pm 0.08$.

The results are displayed in Fig. 45 and Fig 45a, 47 a, b, c.

FIG. 47b Analysis of the triple angular correlations (Geometries I, II) for the r$\longrightarrow$3.68$\rightarrow$0.840 cascade at the 721 KeV resonance assuming a 5/2$\longrightarrow$3/2$\longrightarrow\frac{1}{2}$ spin sequence. The solid curves of the right hand Figure are the theoretical predictions and the hatched areas the experimental measurements. The left hand Figure shows the energy intervals considered (hatched) for the triple correlation measurements.

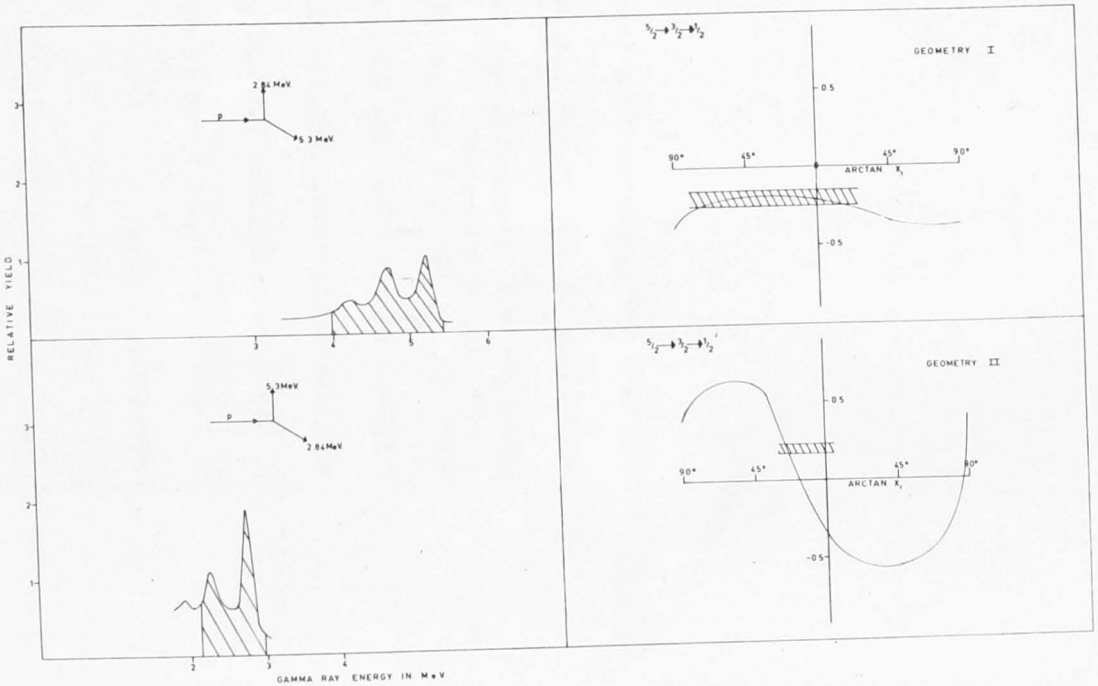
2.84 MeV
p
5.3 MeV
5.3MeV
p
2.84MeV
RELATIVE YIELD
GAMMA RAY ENERGY IN MeV
5/2 → 3/2 → 1/2
GEOMETRY I
0.5
-0.5
90°
45°
45°
90°
ARCTAN X1
5/2 → 3/2 → 1/2
GEOMETRY II
0.5
-0.5
90°
45°
45°
90°
ARCTAN X1

FIG. 48 The 2.84 MeV gamma-ray from the 3.68 $\rightarrow$ 0.840 transition at the 721 KeV resonance. The gamma-ray was fitted with the 2.61 MeV γ-ray from ThC''. The open circles represent the residual counts after the 2.84 line shape has been subtracted out. This residual is equal to the room background 2.6 MeV gamma ray to at least 97%. Hence there is no 3.68 $\rightarrow$ 1.01 transition (3%).

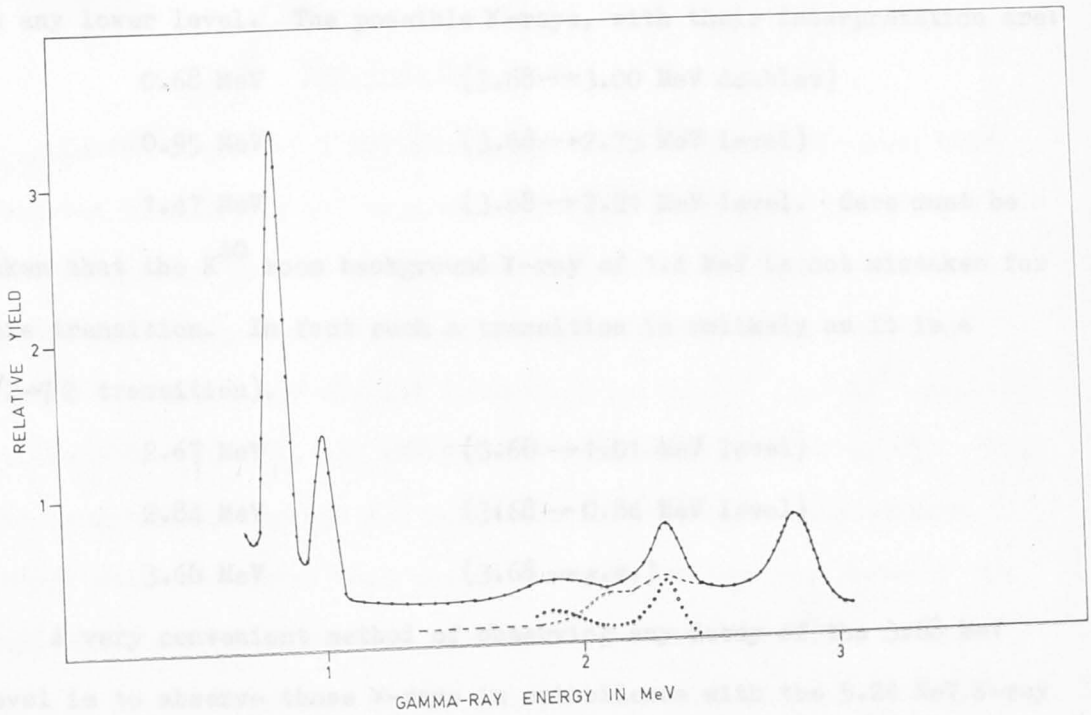
RELATIVE YIELD
1
2
3
1
2
3
GAMMA-RAY ENERGY IN MeV

The Decay of the 3.68 MeV level.

The low energy (below 4.0 MeV) spectrum of the 721 KeV resonance from the $Mg^{26}(p,\gamma)$ reaction is relatively free of γ-rays. Only the 2.84 MeV (3.68 MeV $\rightarrow$ 0.840 MeV) and 2.34 (r $\rightarrow$ 6.6) MeV γ-rays being obvious apart from the 1.01 MeV and 0.840 MeV γ-rays. The region is therefore ideal for observing any decay of the 3.68 MeV level of Al^{27} to any lower level. The possible γ-rays, with their interpretation are:

0.68 MeV (3.68 $\rightarrow$ 3.00 MeV doublet)

0.95 MeV (3.68 $\rightarrow$ 2.73 MeV level)

1.47 MeV (3.68 $\rightarrow$ 2.21 MeV level. Care must be taken that the K^{40} room background γ-ray of 1.4 MeV is not mistaken for this transition. In fact such a transition is unlikely as it is a 3/2$\rightarrow$7/2 transition).

2.67 MeV (3.68 $\rightarrow$ 1.01 MeV level)

2.84 MeV (3.68 $\rightarrow$ 0.84 MeV level)

3.68 MeV (3.68 $\rightarrow$ g.s.)

A very convenient method of observing any decay of the 3.68 MeV level is to observe those γ-rays in coincidence with the 5.24 MeV γ-ray (r $\rightarrow$ 3.68 MeV level). This is because any decay γ-rays from the 3.68 MeV level decay will be in coincidence with the r $\rightarrow$ 3.68 decay. An added advantage is that any non-coincident γ-rays are lost from the spectrum together with room backgrounds being reduced. The coincident spectrum is shown in Fig. 48. Only the 2.84 MeV γ-ray is observed. This was line shape fitted with the 2.61 MeV ThC^{11} γ-ray line shape from a ThC^{11}

source. This reveals that there is also a 2.34 MeV γ-ray present. The source of the 2.34 MeV γ-ray is from the energy window over the 5.24 MeV γ-ray also incorporating the 6.6 MeV γ-ray (6.6 $\rightarrow$ 0), 5.6 (6.6 $\rightarrow$ 1.01) MeV γ-ray and the 5.8 MeV γ-ray (6.6 $\rightarrow$ 0.840) that arise after the r $\rightarrow$ 6.6 MeV transition (2.34 MeV). Hence it was concluded that the 3.68 MeV level decays at least 97% via the 0.840 MeV level.

The 2.98 MeV level.

In the region of 3 MeV excitation in Al^{27} two levels have been observed with 24 $\pm$ 3 KeV separation (Br 54, Va 57, Ba 59). In several experiments one or both of the doublet levels have been excited, but low-energy energy resolution has severely limited the information available. The 3 MeV doublet is excited in the $Mg^{26}(p,\gamma)Al^{27}$ reaction at the 339, 454, 661, 839 and 991 KeV resonances (Le 56, Op 62). With the exception of the 991 KeV resonance, all these resonances have $J \leqslant 3/2$ which indicates that one of the 3.00 MeV states, probably the 2.98 MeV state as it is this level excited, has a low spin $J \leqslant 3/2$. The angular distribution of the r $\rightarrow$ 3.0 transition at the E_p = 339 KeV resonance suggested a spin of 3/2 to one of the levels at 3.00 MeV.

Inelastic particle scattering has shown that the level at 3.0 MeV decays partially via the 2.21 MeV level (0.790 MeV γ-ray) and a spin of 9/2 was consistent with the measurements made. (La 62, Fo 62, Be 61, La 62a). No 2.98 $\rightarrow$ 2.21 transition has been observed and the level decays directly to the ground state (98.8%) and 0.840 MeV level (1.0%) (La 63a).

FIG. 49 The angular distribution data collected at the 991 KeV resonance concerning the 2.98 MeV level of Al^{27}. The r$\longrightarrow$2.98 MeV transition is omitted as only a $0^{\circ}/90^{\circ}$ ratio was obtained. The left hand diagrams show the energy intervals (hatched) considered for the distribution measurements.

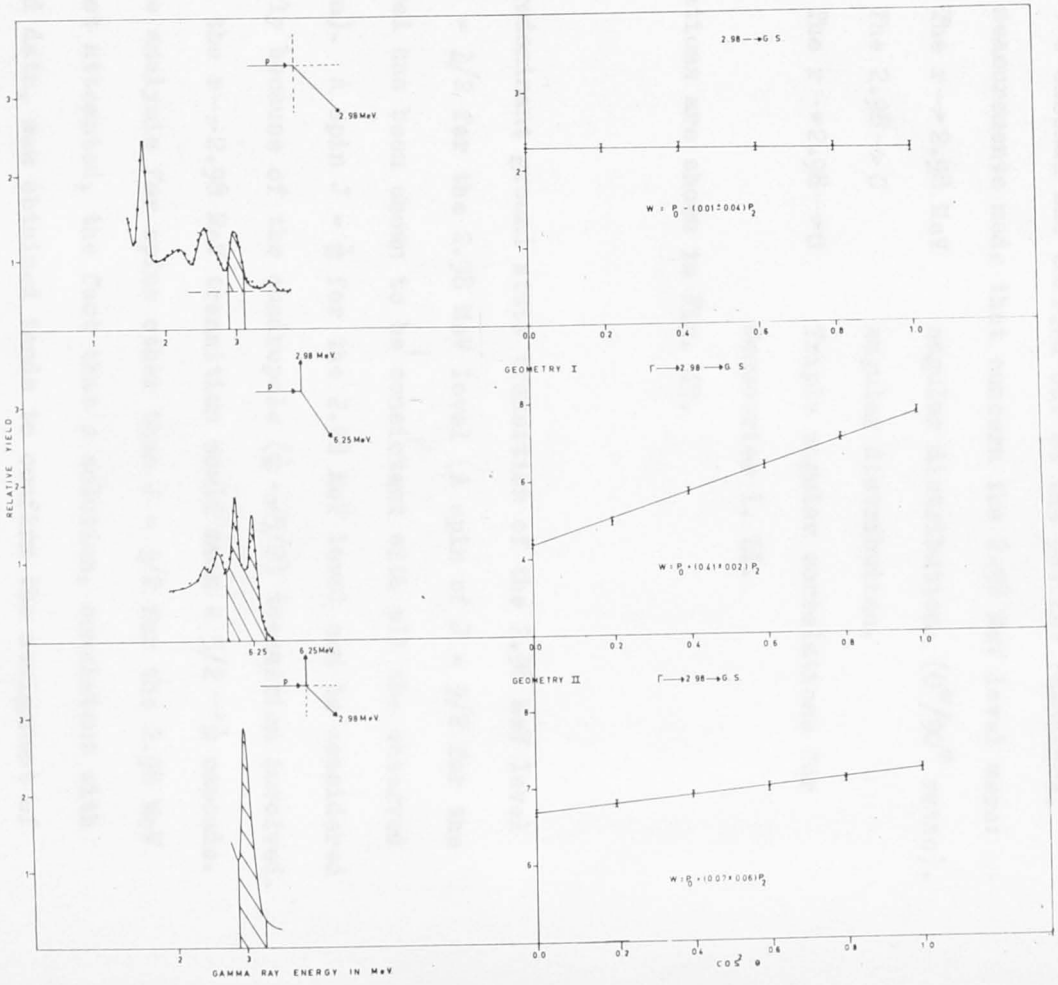
2.98 → G.S.
p
2.98 MeV.
W = P0 - (0.01 ± 0.04) P2
GEOMETRY I
Γ → 2.98 → G.S.
2.98 MeV.
p
6.25 MeV.
W = P0 + (0.41 ± 0.02) P2
6.25
6.25 MeV.
GEOMETRY II
Γ → 2.98 → G.S.
p
2.98 MeV.
W = P0 + (0.07 ± 0.06) P2
RELATIVE YIELD
GAMMA RAY ENERGY IN MeV
cos² θ

The 2.98 MeV level was fed by the 991 KeV resonance of the $Mg^{26}(p,\gamma)$ reaction, as previously described. The 2.98 MeV level was identified by the presence of a 3.00 MeV γ-ray (2.98→0) and the absence of a 0.790 MeV γ-ray (3.0→2.21). Hence analysis of the r→2.98→0 cascade was carried out at the 991 KeV resonance. The actual measurements made that concern the 2.98 MeV level were:

(i) The r→2.98 MeV angular distribution. ($0^\circ/90^\circ$ ratio).

(ii) The 2.98→0 angular distribution.

(iii) The r→2.98→0 Triple angular correlations for Geometries I, II.

The correlations are shown in Fig. 49.

Discussion.

The predominant ground state transition of the 2.98 MeV level indicates J = 3/2 for the 2.98 MeV level (A spin of J = 9/2 for the 3.0 MeV level has been shown to be consistent with all the observed data (La 63a). A spin J = $\frac{1}{2}$ for the 2.98 MeV level can be considered very unlikely because of the quadrupole ($\frac{1}{2}$→5/2) transition involved. In addition the r→2.98 MeV transition would mean a 5/2→$\frac{1}{2}$ cascade. Although the analysis for spins other than J = 3/2 for the 2.98 MeV level was not attempted, the fact that a solution, consistent with the observed data, was obtained tends to confirm the assignment of 3/2. The results of the analysis of the data are given in Table 12 for the sequences 5/2→3/2→5/2 and 7/2→3/2→5/2. Both of these sequences gave consistent values for the mixing ratio of the 2.98→0 transition. Hence it was concluded that J = 3/2 for the 2.98 MeV level

FIG. 49a The 2.98 level of Al^{27}.

The analysis of the $r \rightarrow 2.98 \rightarrow 0$ transition for spin sequences $5/2 \rightarrow 3/2 \rightarrow 5/2$ and $7/2 \rightarrow 3/2 \rightarrow 5/2$. The top figure shows the direct transition to the 2.98 level. The second figure shows the 2.98 to ground state transition. The bottom two show the triple correlations for Geometries I and II. In all cases the experimental measurements are the hatched areas and the solid curves are the theoretical predictions.

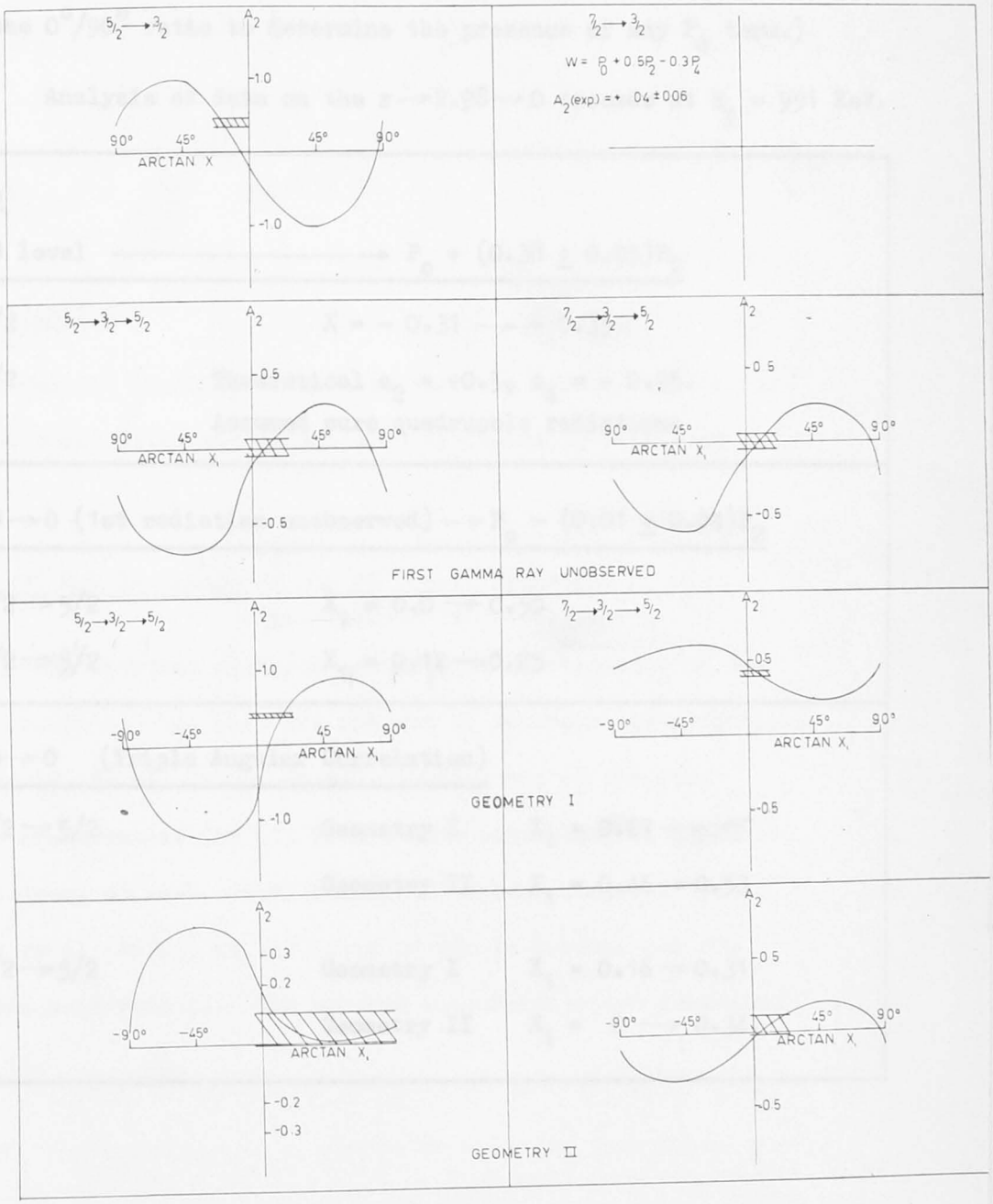
5/2 → 3/2
A2
1.0
90° 45° 45° 90°
ARCTAN X
-1.0
7/2 → 3/2
W = P0 + 0.5P2 - 0.3P4
A2(exp) = + 04 ± 006
5/2 → 3/2 → 5/2
A2
0.5
90° 45° 45° 90°
ARCTAN X1
-0.5
7/2 → 3/2 → 5/2
A2
0.5
90° 45° 45° 90°
ARCTAN X1
-0.5
FIRST GAMMA RAY UNOBSERVED
5/2 → 3/2 → 5/2
A2
1.0
-90° -45° 45 90°
ARCTAN X1
-1.0
7/2 → 3/2 → 5/2
A2
0.5
-90° -45° 45° 90°
ARCTAN X1
-0.5
GEOMETRY I
A2
0.3
0.2
-90° -45°
ARCTAN X1
-0.2
-0.3
A2
0.5
-90° -45° 45° 90°
ARCTAN X1
-0.5
GEOMETRY II

and J = 5/2, 7/2 for the 991 KeV resonance level. On the basis of the analysis a useful measurement would be a complete angular distribution of the r⇝2.98 MeV level transition (all six angles instead of just the $0^{\circ}/90^{\circ}$ ratio to determine the presence of any P_4 term.)

Table 12 Analysis of data on the r⇝2.98→0 cascade at E_p = 991 KeV.

Sequence	
r⇝2.98 level ——————→	$P_o + (0.38 \pm 0.05)P_2$
5/2 →3/2	X = − 0.31 → − 0.35
7/2 →3/2	Theoretical a_2 = +0.5, a_4 = − 0.25. Assumed pure quadrupole radiation.
r⇝2.98→0 (1st radiation unobserved) →	$P_o - (0.01 \pm 0.04)P_2$
5/2 →3/2→5/2	X_1 = 0.0 → 0.50
7/2 →3/2→5/2	X_1 = 0.12→0.25
r →2.98→0 (Triple Angular Correlation)	
5/2 →3/2→5/2	Geometry I X_1 = 0.27 → ∝
	Geometry II X_1 = 0.46→0.53
7/2 →3/2→5/2	Geometry I X_1 = 0.16→0.31
	Geometry II X_1 = 0 → 0.34.

* * * * * * * * * * *

CHAPTER V

5.1 Introduction.

This chapter describes some work that was carried out during the period spent doing the M. Sc. and are basically unrelated topics.

5.2 The 991 KeV Resonance of the $Al^{27}(p,\gamma)$ Reaction.

The γ-ray spectrum produced at the 991 KeV resonance of the $Al^{27}(p,\gamma)$ reaction has been the subject of numerous investigations (Ha 55, Br 59, Ba 61, Si 63, An 63). Though two of the more extensive measurements (Ba 61, Si 63) were consistent with almost identical decay schemes, these results have been disputed by Antoufiev et al (An 63) on the basis of single crystal and sum coincidence measurements. The various measurements are summarised in Table 13.

Table 13

Bashkin and Ophel (Ba 61)		Simons et al (Si 63)		Antoufiev et al (An 63)	
Eγ (MeV)	Relative Intensity	Eγ (MeV)	Relative Intensity	Eγ (MeV)	Relative Intensity
1.78	124	1.77	123	1.78	100
				2.25	5
2.84	10	2.84	7.5	2.75	4
3.12	<5	3.08	3	3.2	4
4.52	10	4.58	10)	4.62	14
4.78	13	4.75	11)		
5.12	<2	5.15	~2	-	
		5.60	~1	-	
6.04	10	6.05	8)	6.15	5
6.30	<3	6.25	3)		
7.40	<2	7.40	~1	-	
7.95	8	7.95	13	7.93	7
8.98	<3	9.49	3	9.38	4
10.76	100	10.76	100	10.76	100

In particular, Antoufiev et al found no evidence for a r $\longrightarrow$ 7.8 MeV transition, corresponding to an energy of 4.75 MeV, and listed a 6.15 MeV γ-ray whereas Bashkin and Ophel (Ba 61) and Simons et al (Si 63) observed 6.02 and 6.3 MeV γ-rays. The former discrepancy is apparent

only in the single crystal data of Antoufiev et al even though they claim that the good resolution of the sum coincidence spectrum would resolve two γ-rays in the vicinity of 4.6 MeV. It should be noted that the sum coincidence method, with the energy sum set at the resonance energy, effectively selects only double cascades; whereas one of the proposed transitions in (Ba 61, Si 63) is part of a triple cascade.

Both discrepancies concern the possible excitation of the 7.80 MeV level of Si^{28} and, since it would appear that this level is not excited at any of the many other resonances of the $Al^{27}(p,\gamma)$ reaction, further studies of the resonance seemed worthwhile in an attempt to resolve the existing differences.

A good resolution spectrum was obtained at the resonance using a three crystal spectrometer (section 2.3.) (T.C.S.) located at an angle of 55° with respect to the incoming proton beam. Details of the accelerator and target facilities have been described in (Ba 61). In addition, coincidence spectra were obtained for various gating windows with two 5" x 4" NaI(Tl) spectrometers mounted at 90° and 55° to the proton beam direction. The γ-rays in an energy window of the 90° spectrometer gated the 55° spectrometer spectrum.

A T.C.S. spectrum accumulated in a run of eight hours duration is shown in Fig. 51 and the energies and relative intensities of the γ-rays identified are listed in Table 14. In general, the agreement with (Ba 61, Si 63) is good except that an additional γ-ray with an energy of 10.30 MeV has been observed. The width of the group at about 4.6 MeV confirms that at least two γ-rays are present. Portion

FIG. 51 A T.C.S. spectrum accumulated in a run of eight hours duration at the 991 KeV resonance of the $Al^{27}(p,\gamma)Si^{28}$ reaction.

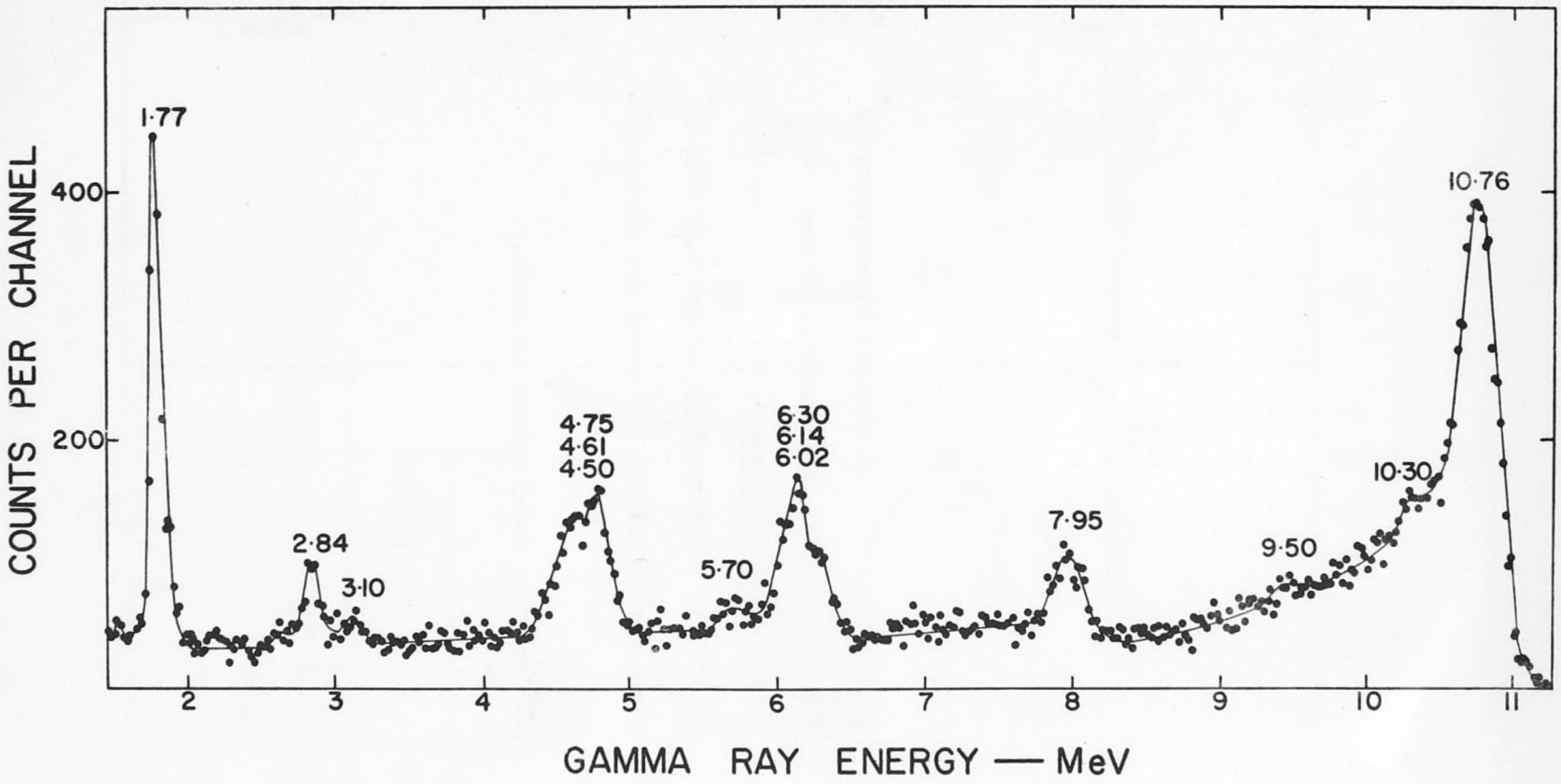
COUNTS PER CHANNEL
400
200
1·77
2·84
3·10
4·75
4·61
4·50
5·70
6·30
6·14
6·02
7·95
9·50
10·30
10·76
2
3
4
5
6
7
8
9
10
11
GAMMA RAY ENERGY — MeV

FIGURE 51

FIG. 52 Spectra from several coincident measurements taken at the 991 KeV resonance of the $Al^{27}(p,\gamma)Si^{28}$ reaction.

NOTE The relative yield of the 1.52 MeV gamma-ray is greatly increased for windows IV and V.

The proposed decay scheme is shown.

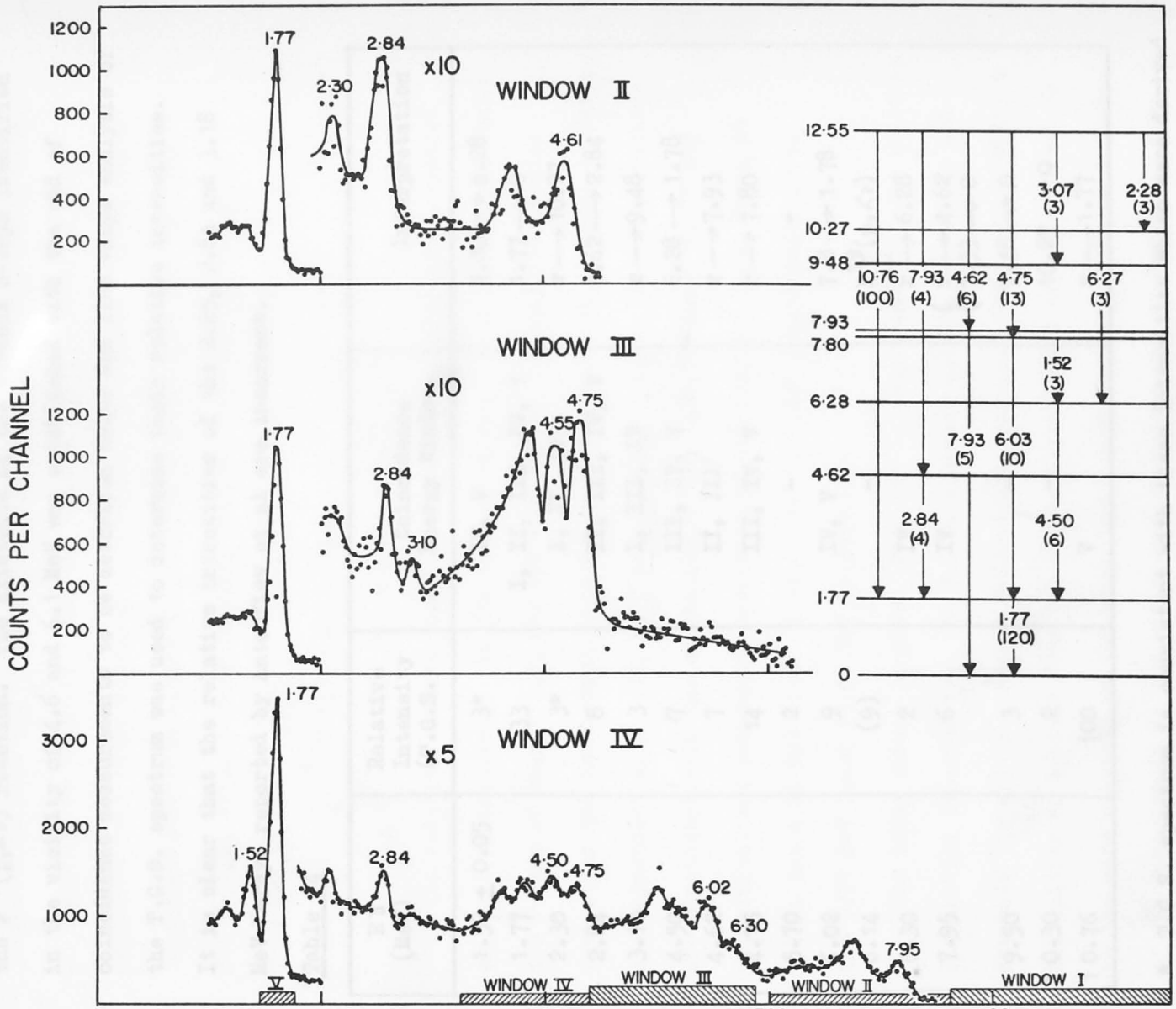
COUNTS PER CHANNEL
CHANNEL NUMBER
WINDOW II
WINDOW III
WINDOW IV
x10
x10
x5
1·77
2·84
2·30
4·61
4·75
4·55
3·10
1·52
4·50
6·02
6·30
7·95
WINDOW V
WINDOW IV
WINDOW III
WINDOW II
WINDOW I
12·55
10·27
9·48
7·93
7·80
6·28
4·62
1·77
0
10·76 (100)
7·93 (4)
4·62 (6)
4·75 (13)
6·27 (3)
3·07 (3)
2·28 (3)
1·52 (3)
7·93 (5)
6·03 (10)
2·84 (4)
4·50 (6)
1·77 (120)

FIGURE 4.52

of the peak at 6.10 MeV (~50%) is due to a 6.14 MeV contribution from the $F^{19}(p,\alpha\gamma)$ reaction. The existence of the various γ-rays identified in the vicinity of 4.6 and 6.1 MeV was established with the aid of coincidence measurements to be described below and line shape analysis of the T.C.S. spectrum was used to determine their relative intensities. It is clear that the relative intensities of the 2.25, 2.84 and 3.18 MeV γ-rays reported by Antoufiev et al are incorrect.

Table 14

E_γ (MeV)	Relative Intensity (T.C.S.)	Coincidence Energy Window	Interpretation
1.52 ± 0.05	3*	IV, V	7.80 → 6.28
1.77	133	I, II, III, IV, V	1.77 → 0
2.30	3*	I, II, IV	r → 10.27
2.84	8	II, III, IV, V	4.62 → 2.84
3.10	3	I, III, IV	r → 9.48
4.50	7	III, IV, V	6.28 → 1.78
4.62	7	II, III	r → 7.93
4.75	14	III, IV, V	r → 7.80
5.70	2	-	-
6.02	9	IV, V	7.8 → 1.78
6.14	(9)	-	$F^{19}(p,\alpha\gamma)$
6.30	2	IV	r → 6.28
7.95	6	IV	(r → 4.62 (7.93 → 0
9.50	3	-	9.48 → 0
10.30	2	-	10.27 → 0
10.76	100	V	r → 1.77

* T.C.S. spectrum is consistent with these intensities which were derived from coincidence spectra.

The results of several of the coincidence measurements are presented in Fig. 52. A summary of all the coincidence measurements is contained in Table 14. The two results considered to be most important were those obtained with windows II and IV. The spectrum in coincidence with window II contains both the 4.61 and the 2.84 MeV γ-rays, clearly demonstrating that the 7.95 MeV γ-ray arises from two sources

$$\text{(i)} \quad r \longrightarrow 7.93 \longrightarrow 0$$

$$\text{(ii)} \quad r \longrightarrow 4.62 \longrightarrow 1.77 \longrightarrow 0.$$

The relative contributions of these two cascades were estimated as 3 : 2 respectively. In the case of Window IV, it is apparent that the γ-rays of energy 4.75 MeV and 4.50 MeV are in coincidence with each other and furthermore that γ-rays of one or both of these energies are coincident with 1.52, 6.02 and 6.30 MeV -rays. Both observations are consistent with the excitation of the 7.80 MeV level (4.75 MeV transition) and subsequent branching of the 7.80 MeV level decay to either the 6.28 MeV level (1.52, 4.50, 1.77 MeV transitions) or to the 1.77 MeV level (6.02 MeV transition).

The decay scheme proposed (Fig. 52) is consistent with the relative intensities observed from the T.C.S. spectrum and (Ba 61, Si 63) and accounts for all the present coincidence spectra. The overall relative intensities as derived from the single crystal data were considered to be the more reliable as the basis for a decay scheme. This is because of the uncertainty in the efficiency as a function of energy for the T.C.S. However, the combined T.C.S. and coincidence data were used for the relative intensities of the closely spaced transitions at 4.5,

FIG. 53 The essential features of a solid state gamma-ray detector.

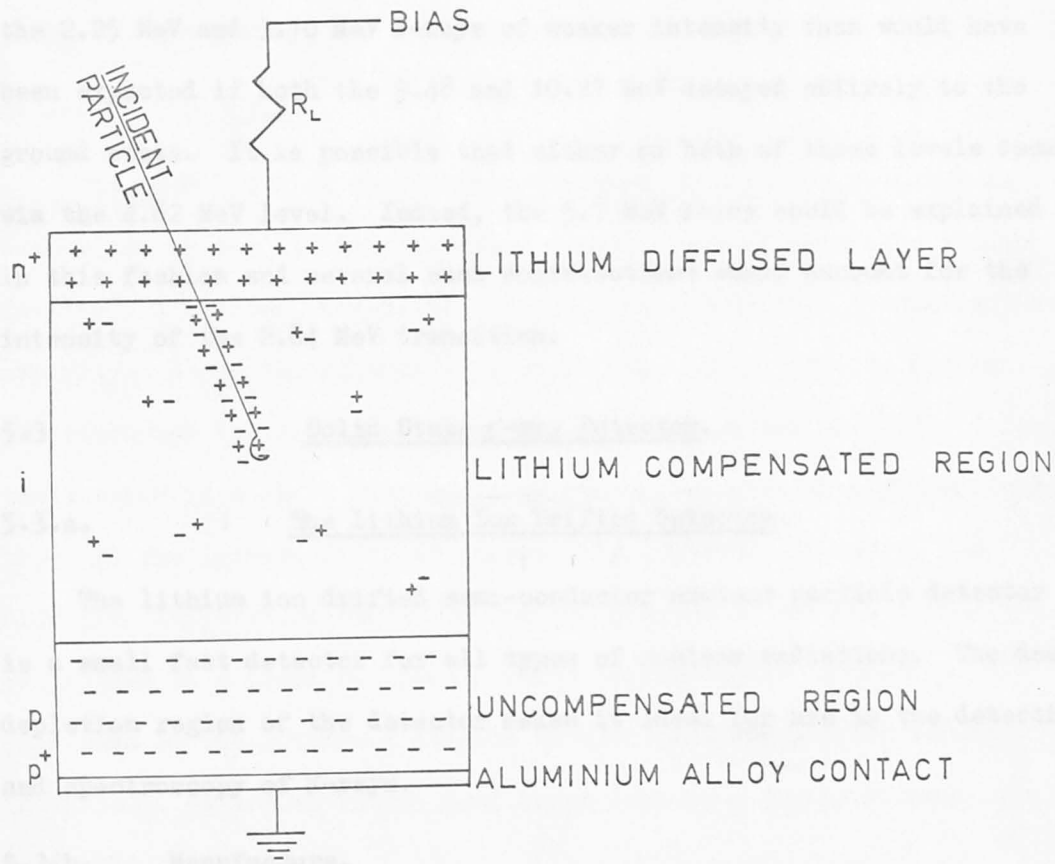
BIAS
R_L
INCIDENT PARTICLE
n^+
LITHIUM DIFFUSED LAYER
i
LITHIUM COMPENSATED REGION
p
UNCOMPENSATED REGION
p^+
ALUMINIUM ALLOY CONTACT

4.62, and 4.75 MeV and at 6.02 and 6.30 MeV.

The observed intensity of the 2.84 MeV γ-ray is not well accounted for by the proposed scheme. Transitions with intensities less than 3% of the 10.76 MeV γ-ray intensity were not investigated since it was felt that no useful branching ratio information could be obtained. However, the gated spectrum coincident with window I contained both the 2.25 MeV and 3.10 MeV γ-rays of weaker intensity than would have been expected if both the 9.48 and 10.27 MeV decayed entirely to the ground state. It is possible that either or both of these levels decays via the 4.62 MeV level. Indeed, the 5.7 MeV γ-ray could be explained in this fashion and several such contributions would account for the intensity of the 2.84 MeV transition.

5.3 Solid State γ-ray Detector.

5.3.a. The Lithium Ion Drifted Detector.

The lithium ion drifted semi-conductor nuclear particle detector is a small fast detector for all types of nuclear radiations. The deep depletion region of the detector makes it ideal for use in the detection and spectroscopy of γ-rays.

5.3.b. Manufacture.

The lithium ion drift process is a good means of obtaining deep depletion regions in solid state detectors. Briefly the manufacture is a two step process. Firstly the lithium is diffused at about 400^{o}C into one face of a piece of low resistivity p-type (boron doped) silicon (or Germanium), producing a n p junction. The diode is heated

to 125°C to increase the lithium mobility and placed under a reverse bias. Positively charged lithium ions drift in the depletion region under the influence of the applied electric field and compensate the negatively charged boron acceptor ions, thereby producing an intrinsic layer which is the sensitive region of the detector. After the silicon (Germanium) has been compensated to the required depth, it is cut to the proper size and shape and mounted.

5.3.c. Properties.

The dead layer on the lithium diffused face of the detector is determined by the lithium diffusion cycle. Lithium acts like a donor (n-type) in silicon, but is an interstitial rather than a substitutional impurity. Hence it diffuses rapidly through tunnels in the crystal structure and the diffusion cycle must be carried out at rather a low temperature in a short time cycle to prevent an excessively deep dead layer on the lithium diffused face of the detector. However, the diffusion temperature cannot be too low because of the low solubility of lithium in silicon at low diffusion temperatures. Because of the magnitude of the lithium diffusion constant and the lithium solubility in silicon, detectors with a dead layer less than 50μ of silicon are difficult to fabricate.

The more common detector has four regions:

(i) The lithium diffused layer through which the nuclear particles enter.

(ii) A lithium compensated region which is the sensitive region of the detector.

(iii) An uncompensated layer.

(iv) An aluminium alloyed layer which provides a low resistance

non-injecting contact to the back surface of the detector. A thin evaporated metal film covers the lithium diffused face of the detector to obtain a low resistance contact to the front face of the detector.

Several other detector structures are possible; one is the structure wherein the 'dead' silicon p layer is absent. This is the dE/dX counter.

5.3.d. Mode of Operation.

The essential features of the detector are shown in Fig. 53. The lithium diffused layer (10-100μ) produces an n-type region containing a high concentration of free electrons and immobile ionized lithium ions. The uncompensated p-type silicon contains an excess of free holes and negative boron acceptor ions. When a reverse bias is applied, as shown, a depletion layer which is swept free of electrons and holes is formed throughout the lithium compensated region and extending a short distance into the heavily doped lithium and boron regions. Assuming that the compensated region is intrinsic the applied voltage V produces a uniform electric field $\mathcal{E} = v/d$ throughout the compensated region of depth d. If a nuclear particle passes through the depletion region, electron hole pairs are produced by inelastic collisions with the silicon atoms. These mobile carriers are swept apart by the electric field giving rise to an electrical pulse proportional to the energy of the particle.

The average energy to produce an electron-hole pair in silicon is 3.5 eV. (This appears to be independent of particle type.) Hence a particle of energy E deposits a charge $Q = e\,E/3.5C$ on the detector

capacitance. The high carrier mobilities and drift velocities combined with the large electric field results in pulses with nano-second rise times.

If the electron-hole pairs do not reach the collecting electrodes the collected charge is less than the expected value. This leads to poor energy resolution and an apparent energy loss.

5.3.e. Solid State Radiations, Inc. now has available lithium ion drifted germanium solid state detectors. The detector represents a valuable supplement to the existing techniques of scintillation spectroscopy. While the photo-electric efficiency of the device is poor the resolution is very good indeed ($\sim 2\%$). Because of its low (n,p) cross section, compared with silicon, it permits charged particle and γ-ray spectroscopy in the presence of fast neutrons.

* * * * * * * * * *

APPENDIX 1

This Appendix contains some of the calculations carried out for the various experiments investigated in the thesis.

A. The thickness of the 200 μgm/cm^2 B^{10} target to

(1) 6 MeV He^{3++}

(2) 8 MeV He^{3++}

(3) 10 MeV He^{3++}

1 $\left(\frac{dE}{dx}\right)_{He^3}\Big|_E = 4\left(\frac{dE}{dx}\right)_p\Big|_{E/3}$, E is the He^3 energy.

Hence proton energy to be considered is 2 MeV

$\left(\frac{dE}{dx}\right)_{2\text{ MeV p}}$ = 130 KeV cm^2/mg.

$\therefore \left(\frac{dE}{dx}\right)_{He^3 .6\text{ MeV}}$ = 520 KeV cm^2/mg.

$\therefore$ dE = 520 x 0.2 KeV

= 104.0 KeV

$\simeq$ <u>110 KeV</u>.

2 Similarly dE = 85.6 KeV

3 " dE = 76 KeV.

B. In the $C^{12}(He^3,n)O^{14}$ experiment C^{12} foils were used. This meant that a material had to be placed behind the foil to stop the O^{14} recoiling away from the counting area. A gold foil was used. The calculation on the thickness of gold foil required follows:

(i) Maximum O^{14} energy.

From the Nuclear Data tables part 3 we can deduce that the maximum possible O^{14} energy is ~4 MeV.

The question of the energy loss of heavy ions is still largely unexplored. The experimental information is fragmentary. Knipp and Teller (Kn 41) have proposed a simple scheme for estimating the order of magnitude of the stopping cross section of heavy ions. They suppose that the charge on a moving ion fluctuates as the ion captures and loses electrons; the ion will have an average charge i which depends on the velocity and not on the stopping material. Then

$$\mathcal{E}_{ion}(v) = i^2 \mathcal{E}_p(v)$$

as long as ion energy is greater than 250 KeV per mass unit.(A condition fulfilled here). The average value i of the ion charge has been computed by Brunings et al (Br 41). From this we get for O^{14} in gold that

$$\frac{i^2}{Z} \simeq .2$$

$$\therefore\ i^2 \simeq 13$$

$$\therefore\ \left(\frac{dE}{dx}\right)_{O^{14}}\Big|_{4\ MeV} \simeq 13 \left(\frac{dE}{dx}\right)_{p}\Big|_{.3\ MeV}$$

$$\simeq 13 \times 115 \text{ KeV cm}^2/\text{mg. for gold}$$

$$\therefore\ dx \simeq \frac{4000}{13 \times 115} \text{ mg/cm}^2$$

$$\simeq 2.6 \text{ mg/cm}^2$$

Hence the 3 mg/cm^2 foil should stop the O^{14} nuclei.

(B) In section 3.2. . . . it was mentioned that $\frac{1}{8}$" lead was placed over the crystals to improve the 2.31/0.511 yield ratio. Here I plan to determine the actual improvement.

Now $$I_{2.31} = I_o e^{-\mu_{2.31} x}$$

where the symbols have their usual meaning,

and $$I_{.511} = I_o' e^{-\mu_{.511} x}$$

$$\therefore \quad \frac{I_{2.31}}{I_{.511}} = \frac{I_o}{I_o'} \frac{e^{-\mu_{2.71} x}}{e^{-\mu_{.511} x}}$$

Hence $$\frac{I_{2.31}}{I_{.511}} \Big/ \frac{I_o}{I_o'} = \frac{e^{-\mu_{2.31} x}}{e^{-\mu_{.511} x}} = \frac{e^{\mu_{.511} x}}{e^{\mu_{2.31} x}} = R' \text{ (say)}$$

$x = \frac{1}{8}" = .32$ cms.

$\mu_{2.31} = .52 \text{ cm}^{-1}$

$\mu_{.511} = 1.76 \text{ cm}^{-1}$

$$\therefore \quad R' = \frac{e^{1.76 \times .32}}{e^{0.52 \times 0.32}}$$

$$= \frac{e^{0.51}}{e^{0.17}}$$

$$= \frac{1.665}{1.185}$$

$$= 1.4$$

Hence the improvement is ~25%.

Experimentally the improvement was 30%. The difference could be due to the fact that the theoretical value was computed on the assumption of a narrow beam of γ-rays. In practice the beam was anything but narrow. Hence it had to pass through more lead (i.e. non normal transmission).

* * * * * * * * * * *

APPENDIX II

The Scintillation Process.

The precise mechanism producing the scintillations in NaI(Tl) is unknown at present. (It is generally called phosphorescence). Given here is a brief summary of the viewpoint as it stands today.

The Mechanism of Phosphorescence.

The electrons are assumed to remain for a great deal of their time in so-called 'traps'. Whilst in a 'trap' they are unable to fall from an excited state to a lower energy state and thus cause emission. It is this fact that is the basic cause of phosphorescence. The time spent in the traps is very large compared with the time which the electrons spend in moving through the phosphor, and the latter can even be neglected. An electron is supposed removed from a trap by the absorption of energy from the surrounding medium. Once free they can re-emit as normal. Thus the decay curve depends on the probability of the electron being released from these traps.

Let depth of trap = $\mathcal{E}$. This is directly proportional to its holding power. Also let us suppose that once electrons have been released from a trap they never become trapped again.

Then Intensity at time t $\quad I = \frac{-dn}{dt} = \alpha n$

where n = total number of electrons trapped at time t

$$\therefore \quad I_t = {}_{t=0}I e^{-\alpha t}$$

$$\therefore \quad \log \frac{I}{I_o} = -\alpha t.$$

α, the reciprocal of the mean life t of the electrons in a trap, is a function of temperature.

$$\text{i.e.} \quad \alpha = s\, e^{-\mathcal{E}/kT}.$$

where s is also generally a function of temperature. It determines the probability with which an electron leaves a trap when the energy required to do so is provided solely by thermal fluctuations. Unfortunately variation of $\mathcal{E}$ by as little as 1% causes the decay curve to deviate from a straight line in a semi-log diagram and this causes confusion.

Randall (Ra 45) assumed that s was independent of temperature and derived equations for several trap ($\mathcal{E}$) distributions, which may be regarded as the limiting cases of those occurring in real crystals. The equations were:

(a) Assuming a uniform distribution of traps all with the same value of $\mathcal{E}$.

$$I_{(t)} \cdot t = \text{const.}$$

(b) Assuming a quasi-uniform distribution

$$I_{(t)} \cdot t = n_{(t)} \cdot \text{const.}$$

(c) Assuming an exponential distribution. The trap depth $\mathcal{E}$ being $= e^{-b\mathcal{E}}$.

$$I_{(t)} = \text{const.}\ t^{-(bkT + 1)}$$

A fourth equation could be derived by assuming that the distribution was completely random with no two traps of the same depth.

Finally it is fundamental for the phosphorescence process that the excited electron moves far away from the excited atom or molecular centre before emission takes place.

3. Theories of Phosphorescence.

There are two rival theories for the explanation of the phenomenon; one a mono-molecular process the other a bi-molecular process. Although the bi-molecular theory gives the better agreement with experimental results it seems that because of the far simpler mathematics of the mono-molecular theory it is the latter that is used. Also the results obtained from the mono-molecular theory are fairly accurate as was shown by Brenger who investigated the KC_2 (tellurium activated) phosphor. He based his calculations on a simple mono-molecular reaction and found the energy of activation needed for transferring the electrons from the traps to the state from which phosphorescence can take place. He deduced the equation

$$\frac{1}{t} = \frac{1}{t_o} \cdot \text{const.} \; e^{-\frac{\mathcal{E}}{kT}} \text{sec}^{-1}$$

t = time of phosphorescence t_o = time coefficient of excited state.

The results obtained were

$$\mathcal{E} = 0.67 \text{ e.V. or } 15.4 \text{ Kcal/mole}$$

and the experimental curves agreed well with the theoretical predictions.

Lenard's Theory. (Pr 49)

Lenard was the first person to attempt to give a comprehensive

explanation of phosphorescence. His ideas were, broadly speaking, as follows:-

When the electromagnetic radiation is absorbed the electrons are displaced from their natural equilibrium positions. This energy is stored as potential energy of the electrons which are trapped in a potential trough, from which they are released by thermal fluctuations of energy. The final stage is the return of the electrons to their initial positions and the subsequent emission of light. Thus according to Lenard the whole process takes place inside a single 'centre'. (This has led to the term 'centre theory'). A centre consists of an atom of activator element surrounded by a great number of molecules of the base material. Although the theory as a whole is rejected now the loose definition of the centres gives it tremendous elasticity and permits it to explain many aspects of phosphorescence in solids.

Levshin's Theory. (Le 36)

The above process is essentially mono-molecular. A rival theory originated by Becquerel and later elaborated by Levshin is mainly a bi-molecular process.

According to this theory an electron after excitation can (and does) leave the centre of origin and travel (Electro-Motive Force) to another excited centre which has lost its electron in the same way. This leads to a hyperbolic decay curve. This was checked and found to be true for many phosphors.

In addition the results that were quoted in support of Lenard's theory can also be adequately interpreted and predicted on the bi-molecular theory. However the decay need not follow the law of a

second order reaction for if most of the electrons are in traps then the number available to combine with centres is small and the decay curve is exponential (i.e. first-order decay). If these traps have different depths then the resultant curve is one of the superposition of exponentials. This is in fact the same result as from Lenard's theory taking the centres to be of different duration.

4. The Emission and Excitation Processes.

The most generally accepted hypothesis is that proposed by Schoen (Sc 38). The ground state of the activating atom is taken to have a higher energy than the ground state of the 'pure' atoms of the phosphor. The positive hole, formed by the emission of an electron by the absorbed light energy, is filled by an electron falling into it from the activator atom. The emission of light then occurs when an electron in the conduction band recombines with the hole in the activator atom (formed by the preceding process). This process is obviously bi-molecular in agreement with Levshin's theory.

Lehovec (Le 55) found that the dependance of the decay of phosphorescence on time varies with the concentration of impurities which do not participate in the phosphorescence process but merely contribute towards the space charge in the phosphor. This can be explained by the experimentally found fact that positive holes and electrons are more easily captured by certain impurity atoms than others.

5. Absorption and Emission Bands.

The cases where the complete absorption spectra of phosphors have

been investigated are rare indeed, instead it is usually the excitation spectra that are known.

The absorption and excitation spectrum of Mn-activated ZnS, investigated by Kroeger, provides a typical example. ZnS has a strong, apparently continuous absorption band in the ultra-violet with a sharp long-wavelength edge at 3380Å, but extending from there is a flat tail in the direction of increasing wavelength. This tail is due to zinc atoms and lattice defects. On addition of manganese a new band is super-imposed on the tail with an intensity maximum at 3500Å and a long-wavelength limit at 3650Å. As the manganese concentration is increased more absorption bands appear between 3900-5000 Å.

It can be taken for granted that the phosphorescence of Manganese activated phosphors is characteristic of the Mn^{++} ion. According to Kroeger, the weak long-wavelength bands observed in the absorption spectrum of ZnS-(Mn) phosphors reappear in the emission spectrum; the most intense part of the phosphorescence is,. however, in the orange. Fig. II.1 shows a typical complex emission band of a phosphor.

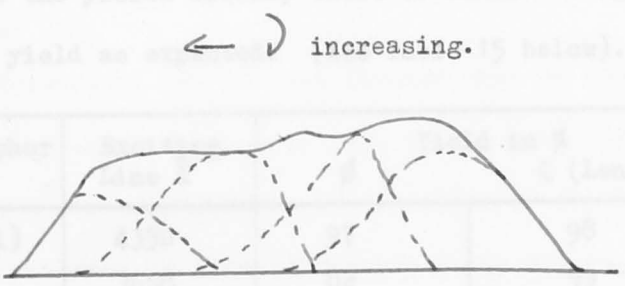

Fig. II.1 Emission band of a phosphor.

The bands corresponding to the excitation of long-lasting phos-

phorescence are connected, in general, with lattice defects, while light absorbed in the unperturbed base lattice gives rise to an after-glow of short duration.

6. Phosphorescence Yield.

This quantity is given the symbol p and is defined as

$$p = \frac{E \text{ emitted}}{E \text{ absorbed}},$$

and for most phosphors the value of p is very close to unity. For example ZnS(Cu) phosphor has a yield of .9.

There is some discussion as to what is meant by E absorbed. Some workers, notably Lenard, use it to mean that it is the exciting energy absorbed by the phosphorescence centre. Others take it to mean the total radiation energy incident on the phosphor that is absorbed by all the phosphor. It can be seen that the second method is the easier for in the first allowance must be made for non-phosphorescence producing absorption and this is very difficult. Using the two interpretations the yields differ, those of Lenard being consistently closer to 100% yield as expected. (See Table 15 below).

Phosphor	Exciting Line Å	Yield in % ϕ	Q (Lenard)
CaS(Bi)	4350	97	98
	3650	82	99
CaS(Cu)	4350	76	92
	3650	64	92
ZnS(Cu)	4350	84	99.5
	3650	73	99.7

Table 15. Phosphorescence Yield of Typical Phosphors.

The differences in Table 15 are explained as follows:-
A part of the light that is absorbed by a phosphor is immediately re-emitted as very short duration fluorescence or even heat. The electrons that have absorbed the energy of the light in the normal manner are trapped in a quasi-stable state. Eventually all these generate phosphorescence. Thus the phosphorescence yield when referred to the exciting absorption energy should always be near to 100%, but it will be much lower if referred to total incident light absorbed by the phosphor because of the above process.

7. Determination of p.

The latest is probably that due to Bocto. The method is to determine the increase in temperature of the phosphor due to irradiation. This temperature increase is related to the same effect in non-phosphorescent carbon black; making thereby possible a calculation of the quantum efficiency. The accuracy claimed for the method is approximately 3%.

8. Conclusion.

Recently Romanovski (Ro 52) put forward what he termed a diffusion theory of phosphorescence. He said that if the mean free path of an electron in the conduction band is of the order of the lattice constant, then the decay kinetics of phosphorescence decay may be described by a linear diffusion equation which takes into account the attraction of

electrons by ionized centres. However, although he cites many cases where the experimental results are as predicted, the general rule seems to be that the free path is not of this magnitude and so it is not surprising that the theory is only used in a very few specific cases.

* * * * * * * * * * *

REFERENCE

Aj 61 Ajzenberg and Dunning. Phys. Rev. 119 1681 (1961)

Aj 62 Ajzenberg - Selove and Lauritsen. Nuclear Data Sheets, Sets 5 and 6 (1962).

Al 58 Altman and MacDonald. Phys. Rev. letters 1, 456 (1958).

Al 62 Altman and MacDonald. University of Maryland Technical report 241 (1962).

An 63 Antoufiev et al. Nuc. Phys. 46, 1, (1963).

Ba 59 Barros et al. Proc. Phys. Soc. 73 793 (1959).

Ba 60 Bardin et al. Phys. Rev. Lett. 5, 323 (1960).

Ba 61 Bashkin and Ophel. Aust. J. of Phys. 14, 335 (1961).

Ba 62 Bardin et al. to be published (1962).

Ba 62a Bardin et al. Phys. Rev. 127 583 (1962)

Ba 63 Bailey. Ph.D. Thesis A.N.U. (1963).

Be 61 Bishop. Nuc. Phys. 14 376 (1961).

Bl 52 Blatt and Weiskopf. Theoretical Nuclear Physics (1952).

Bi 60 Biedenham. Nuclear Spectroscopy, Part II Ed. Ajzenberg-Selove.

Bl 61 Blin - Stoyle and Le Tourneaux. Phys. Rev. 123 627 (1961).

Bl 62 Blin - Stoyle and Le Tourneaux. Ann. Phys. 18 12 (1962).

Bo 36 Bohr. Nature 137 344 (1936).

Bo 53 Bocto. Acta. Phys. Hungar 3 No. 1. (1953).

Br 41 Brunings et al. Phys. Rev. 60, 657 (1941).

Br 54 Browne et al. Phys. Rev. 96, 725, (1954).

Br 56 Bromley and Almqvist. Rep. on Prog. in Phys. 23, 545, (1956)

Br 57 Bromley et al. Phys. Rev. 105 957 (1957).

Br 59 Brenner. Soc. Sci. Fennica. Com. Phys. Math. 23 No. 5 (1959).

Bu 57 Butler et al. Nuclear Stripping reactions, John Wiley and Sons, New York (1957),

Bu 61 Butler and Bondelind. Phys. Rev. 121, 1770, (1961).

Da 52 Davison and Evans. Rev. Mod. Phys. 24, 79 (1952).

De 40 Delsasso, White et al. Phys. Rev. 58 586 (1940).

De 57 Devons and Goldfarb. Handbuch der Physics. 42, 362, (1957).

Di 64 Din. Ph.D. Thesis. Rice University (9164).

Di 64a Din et al. Nuc. Phys. 57, 487, (1964).

Du 60 Durand et al. Phys. Rev. Lett. 4 620 (1960).

Ea 62 Earwaker et al. Nature, 195, 271 (1962).

Ea 63 Earwaker et al. Nuc. Phys. 42, 521, (1963).

Ev 55 Evans. The Atomic Nucleus. (1955).

Fe 62 Ferguson et al. C.R.P. 615. (1962).

Fl 61 Annual Progress Report for 1961. Florida State University (1961).

Fo 62 Foley et al. Nuc. Phys. 37, 23, (1962).

Fu 62 Fulbright et al. NY O 10034 (1962).

Ga 60 Gale et al. Nuc. Phys. 20, 313 (1960).

Ge 59 Gerhart et al. Phys. Rev. 114, 1095 (1959).

Go 58 Gove and Rutlidge CRP - 755 (1958).

Go 59 Goldfarb. Nuclear Reactions I. Edited by Endt and Demeur.

Gu 29 Gurney. Nature, 123, 565 (1929).

Ha 55 Hattons et al. Journal Phys. Soc. Japan 10 242 (1955).

He 57 Heath. Philips Petroleum Co. Report IDO 16408.

He 61 Hendrie and Gerhart. Phys. Rev. 121, 846 (1961).

Hi 59 Hinds and Middleton. Proc. Phys. Soc. 119, 1654 (1960).

Ho 60 Hopkins et al. Bull. Amer. Phys. Soc. 5 239 (1960).

Ho 61 Hopkins et al. Phys. Rev. 121, 1185 (1961).

Ja 59 Jancovici. Ann. Phys. (Paris) 4, 689, (1959).

Je 64 Jenkin. Ph. D. Thesis. A.N.U. (1964).

Ke 58 Kegors et al. IDO 16370 (9158).

Ke 61 Kenny and Caro. Aust. J. of Phys. Vol. 14. No.2. (1961).

Kn 41 Knipp and Teller. Phys. Rev. 59, 659 (1941).

Ku 64 Kuan et al. Nuc. Phys. 51, 3 (1964).

Ku 64a Kuan et al. Nuc. Phys. 57, 487 (1964).

Ku 64b Kuan and Risser. Nuc. Phys. 51, 518 (1964).

La 55 Landon. Phys. Rev. 100 1414 (1955).

La 62 Lawergren and Ophel. Proc. Phys. Soc. 79A 881 (1962).

La 63 Lawergren Ph.D. Thesis A.N.U. (1963).

La 62a Lawergren and Ophel Phys. lett. 2 265 (1962).

La 64 Lawergren (Private Comm.)

La 64a Lawergren. Nuc. Phys. 53 417 (1964).

Le 36 Levshin. Acta. Phys. Polon. 5, 79, (1936).

Le 56 Levin and Hughes. Phys. Rev. 101 1328 (1956).

Le 56a Van de Leun. Physica 22, 1223 (1956).

Le 57 Van de Leun (see Aj 62).

Le 55 Lehovec. J. Opt. Soc. Amer. 45 No. 3. (1958).

Li 63 Lindemann et al. Report on Gatlinberg Conference (1963).

Ma 62 MacDonald and Altman. Bull. Amer. Phys. Soc. 7, 17 (1962).

Ma 63 Manley. Phys. Rev. 130, 241, (1963).

Mo 52 Moskowski. Beta and gamma-ray Spectroscopy. Seigbahn (1952)

Ne 60 Newns. Proc. Phys. Soc. (LONDON) 76, 489, (1960).

Pr 49 Pringsheim. Fluorescence and Phosphorescence. LONDON (1949).

Op 62 Ophel and Lawergren. Nuc. Phys. 30, 215, (1962).

Ro 53 Rose. Phys. Rev. 91, 610 (1953).

Ra 45 Randell. Proc. Roy. Soc. A 184 347 (1945).

Ro 52 Romanovski. Optika i Spectrosk. Vol. 3 No. 6. (1952).

Sc 38 Schoen Z. f. Tech. Phys. 19 361, (1938).

Sh 49 Sherr et al. Phys. Rev. 75 282 (1949).

Si 63 Simons et al. Phys. Lett. 3, 306, (1963).

Sn 50 Snowden. Phys. Rev. 78, 299 (1950).

Ta 63 Tavendale. Rev. Sci. Inst. 4, 214, (1963).

To 33 Tomaschek. Am. d. Phys. 16, 930, (1933).

To 61 Towle and Macefield. Proc. Phys. Soc. 77 399 (1961).

Va 56 Van der Leun et al. Physica 22 1229 (1956).

Va 61 Valerio. Thesis. Iowa State University.

Wa 60 Warburton et al. Phys. Rev. 118, 733. (1960).

We 54 Wegner and Hall. Phys. Rev. 119 1654 (1954).

We 62 Weidenmüller. Bull. Amer. Phys. Soc. 7, 17 (1962).

* * * * * * * * * *